

# **Thermal Tuning of Ethylene/Ethane Selective Cavities of Intrinsically Microporous Polymers**

**Dissertation by**

**Octavio Salinas**

**In Partial Fulfillment of the Requirements for the Degree of  
Doctor of Philosophy**

**King Abdullah University of Science and Technology**

**Thuwal, Kingdom of Saudi Arabia, 2016**

**© June 2016  
Octavio Salinas Montoya  
All Rights Reserved**

The examination committee certifies that this is the approved version of the dissertation of Octavio Salinas:

Supervisor: Ingo Pinnau

Committee Member: William Koros

Committee Member: Zhiping Lai

Committee Member: Yu Han

## ABSTRACT

### **Thermal Tuning of Ethylene/Ethane Selective Cavities of Intrinsically Microporous Polymers**

**Octavio Salinas Montoya**

Ethylene is the most important organic molecule with regard to production volume. Therefore, the energy spent in its separation processes, based on old-fashioned distillation, takes approx. 33% of total operating costs. Membranes do not require significant thermal energy input; therefore, membrane processes may separate hydrocarbons cheaply and just as reliably as distillation columns. Olefin/paraffin separations are the future targets of commercial membrane applications, provided high-performing materials become available at reasonable prices.

This thesis addresses the development of advanced carbon molecular sieve (CMS) membranes derived from intrinsically microporous polymers (PIMs). Chronologically, Chapter 4 of this work reports the evaluation of PIMs as potential ethylene/ethane selective materials, while Chapters 5 to 7 propose PIMs as carbonization precursors. The gravimetric sorption studies conducted in this work regarding both the polymers and their heated-derivatives revealed that this separation is entirely controlled by diffusion differences.

The pristine polymers examined in this study presented BET surface areas from 80 to 720 m<sup>2</sup>g<sup>-1</sup>. Furthermore, the effect of using bromine-substituted PIM-polyimides elucidated a boost in ethylene permeability, but with a significant drop in selectivity. The hydroxyl functionalization of PIM-polyimides was confirmed as a valuable strategy to increase selectivity. Functionalized PMDA-HSBF is the most selective polyimide of

intrinsic microporosity known to date ( $\alpha = 5.1$ ) due to its hydrogen-bonded matrix. In spite of their novelty, pristine PIMs based on the spirobisindane moiety were not tight enough to distinguish between the 0.2 Å difference in diameter of the ethylene/ethane molecules. Therefore, they did not surpass the upper bound limit performance of known polymeric membranes. Nevertheless, the carbons derived from these polymers were excellent ethylene/ethane sieves by virtue of their narrow and tight pore distribution around the 3.6-4.4 Å range.

PIM-based carbons were typically 10 times more permeable than their corresponding low free-volume analogues treated after the weight-loss of the sample reached a plateau. Furthermore, carbons derived from PIM-6FDA-OH and PIM-6FDA at 800 °C were as ethylene separating efficient as their lower free-volume counterparts. The pore sintering mechanism that takes place above 600 °C during the carbonization procedure of these films reduced the entropic freedom of the molecules, as was observed from separation factors of up to 25 under pure-gas conditions and 2 bar of pressure— The best performing CMS membranes reported to date for ethylene/ethane separation.

The mixed-gas separation of 1:1 binary ethylene/ethane mixtures revealed a significant decrease of the pure-gas measurements due to a carbon matrix dilation effect. This localized *ultramicroporous dilation* caused the ethane permeation rate to increase monotonically as the pressure rose to realistic operating values. Nevertheless, the CMS obtained from PIM-6FDA and PIM-6FDA-OH surpassed any diffusion-controlled polymer or carbon that has been reported to date.

## ACKNOWLEDGMENTS

First and foremost, I thank God, the ultimate architect, for giving me the strength to complete this task.

I thank my advisor Prof. Ingo Pinnau. I could not have asked for a better advisor, nor do I wish that any aspect of my research life here at KAUST were any different. I know I will always be fine if I learned anything from him during my period here. I am forever in his debt.

I thank my colleagues, and especially Dr. Xiaohua Ma and Dr. Eric J. Litwiller, for their tremendous help.

Mohsin, Nasser, Fahd: you all enlightened me and offered valuable discussion topics. Thanks to the rest of the AMPM center as well.

Special thanks for the administrators of our center: Nigel, Dalila, and Melinda.

For my friends at KAUST: you are like family to me. You know who you are.

Thank you to my family in Mexico, to whom I dedicate all of my achievements, and to my wife Lecelí, for all of her love and support.

# TABLE OF CONTENTS

<b>LIST OF TABLES.....</b>	<b>13</b>
<b>LIST OF FIGURES.....</b>	<b>15</b>
<b>Chapter 1: Ethylene/Ethane Membrane Separation: Beyond Conventional Distillation Processes</b>	
1.1 Ethylene: the most important building block in the petrochemical industry .....	16
1.2 Steam Cracking .....	18
1.2.1 Conventional ethylene/ethane distillation column .....	19
1.3 Novel membranes: technology for a new age of gaseous hydrocarbon separation .....	21
1.4 Membrane process design .....	23
1.5 Retrofitting of an ethylene/ethane distillation column with an advanced membrane module .....	26
1.6 Membrane materials .....	29
1.6.1 Current polymers that define the performance upper bound of organic membranes .....	31
1.6.2 PIM polymers: the future of gas separation advanced organic materials .....	33
1.7 Strategies to tailor the PSD of advanced PIMs that could enhance the separation performance for the ethylene/ethane gas pair .....	34
1.7.1 Pre-synthesis structural modifications that modify chain rigidity and pore tightness .....	34
1.7.2 Thermal annealing .....	34
1.7.3 Cross-linking .....	35
1.7.4 Formation of polybenzoxazole from ortho-functionalized PIM-PI.....	35
1.7.5 Carbonization.....	36
1.8 Dissertation objectives .....	38
1.9 References .....	40
<b>Chapter 2: Theoretical Background</b>	
2.1 Gas transport through microporous solids .....	49
2.1.1 Transport regime according to pore size .....	49
2.1.2 Solution-diffusion model and the mass balance of an isotropic film .....	51
2.1.3 Transport properties of organic polymers .....	54
2.1.4 The polymer upper bound: empirical and theoretical considerations.....	60
2.1.5 Transport in carbon molecular sieves (CMS).....	62

2.2	Material characterization techniques.....	66
2.2.1	Gel permeation chromatography of polymeric materials .....	66
2.2.2	Thermal stability of polymeric materials.....	67
2.2.3	Functional groups and microstructure determination.....	68
2.2.4	Surface area and pore size distribution (PSD) estimation .....	68
2.3	Non-idealities of membranes that could compromise their long-term performance.....	71
2.3.1	Aging in glassy systems and its influence on transport properties.....	71
2.3.2	Plasticization and competitive sorption during mixed-gas settings.....	73
2.4	References .....	74

### **Chapter 3: Materials and Experimental Procedures**

3.1	Materials and thesis organization.....	83
3.1.1	Synthetic procedures.....	85
3.2	Dense film fabrication.....	86
3.3	Thermal-treatment protocol.....	87
3.4	Pure-gas permeation.....	88
3.4.1	Pure-gas permeation apparatus and testing protocol .....	89
3.5	Mixed-gas permeation.....	91
3.6	Morphology characterization .....	92
3.6.1	TGA .....	92
3.6.2	FTIR.....	93
3.6.3	XRD.....	93
3.6.4	Micromeritics ASAP 2020 .....	93
3.7	Gravimetric sorption .....	93
3.8	References .....	95

### **Chapter 4: Ethylene/Ethane Separation with Spirobisindane-Based Intrinsically Microporous Polymeric Membranes<sup>1</sup>**

4.1	Introduction .....	97
4.2	Chemical structure and physical properties of PIM structures .....	99
4.3	Ethylene/ethane sorption isotherms at 35 °C in PIM membranes.....	102
4.4	Ethylene/ethane pure-gas transport at 35 °C and 2 bar upstream pressure in PIM membranes .....	103
4.5	Ethylene/ethane diffusivity and solubility coefficients at 35 °C and 2 bar upstream pressure in PIM membranes .....	105
4.6	Ethylene/ethane upper bound.....	106

4.7	Conclusions .....	107
4.8	References .....	109

**Chapter 5: Ethylene/Ethane Permeation, Diffusion and Gas Sorption Properties of Carbon Molecular Sieve Membranes Derived from the Prototype Ladder Polymer of Intrinsic Microporosity (PIM-1)<sup>1</sup>**

5.1	Introduction .....	113
5.2	Thermal annealing and CMS formation of pristine PIM-1 films.....	116
5.3	Surface area and PSD estimation of PIM-1 and its heat-derived CMS .....	121
5.4	Pure-gas sorption isotherms of ethylene and ethane in PIM-1 and its heat-derived CMS analogs .....	124
5.5	Pure- gas ethylene/ethane permeation properties.....	126
5.6	Conclusions .....	129
5.7	References .....	131

**Chapter 6: High-Performance Carbon Molecular Sieve and Polybenzoxazole Membranes for Ethylene/Ethane Separation Derived from an Intrinsically Microporous Polyimide<sup>1</sup>**

6.1	Introduction .....	137
6.2	Thermal-annealing of PIM-6FDA-OH.....	140
6.3	Heat treatment of PIM-6FDA-OH .....	140
6.4	CO <sub>2</sub> sorption for PSD estimation of carbonized samples.....	146
6.5	Ethylene/ethane pure-gas permeation properties .....	149
6.6	Gravimetric sorption isotherms at 35 °C for ethylene and ethane .....	150
6.7	Pure-gas diffusivity and solubility of ethylene and ethane .....	153
6.8	Mixed-gas permeability and selectivity of the 800 °C CMS membrane .....	156
6.9	Conclusions .....	158
6.10	References .....	160

**Chapter 7: Fine-Tuning Ultramicroporosity of a Carbon Molecular Sieve Membrane from a Spirobisindane-Containing Microporous Polyimide for Enhanced Ethylene/Ethane Selectivity**

7.1	Introduction .....	166
7.2	Physical properties and carbonization of PIM-6FDA .....	171
7.3	CO <sub>2</sub> sorption for PSD estimation .....	177



7.4	Ethylene/ethane pure-gas permeation properties .....	182
7.5	Mixed-gas permeability and selectivity of the 800 °C CMS membrane .....	185
7.6	Conclusions .....	187
7.7	References .....	189

## **Chapter 8: Conclusions and Recommendations**

8.1	PIMs for ethylene/ethane separation .....	194
8.2	PBO for ethylene/ethane separation .....	195
8.3	PIM-based CMS for ethylene/ethane separation.....	195
8.4	Thermally induced porosity evolution during pyrolysis .....	196
8.5	Dilation of ultramicroporous CMS cavities .....	197
8.6	Recommendations .....	198
8.6.1	Advanced PIMs for ethylene/ethane separation .....	198
8.6.2	Advanced PIM precursors as carbon platforms and thin-film carbons .....	199
8.6.3	Control of the O <sub>2</sub> atmosphere .....	199
8.7	References .....	201

<b>APPENDIX.....</b>	<b>202</b>
----------------------	------------

## LIST OF TABLES

<b>Table 1.1.</b> Largest ethylene production facilities in the world [15].	17
<b>Table 1.2.</b> Physical properties of ethylene and ethane [65].	27
<b>Table 3.1.</b> Chemical structure of the PIMs tested in this work	83
<b>Table 3.2.</b> Membrane preparation conditions of the dense isotropic films.	86
<b>Table 3.3.</b> Protocol of the various thermally treated derivatives of PIM precursors.	88
<b>Table 4.1.</b> Physical and thermal properties of the PIMs tested in this work.	102
<b>Table 4.2.</b> Parameters obtained from fitting experimental data to the dual-mode sorption model for the PIMs tested in this work.	103
<b>Table 4.3.</b> Single-gas permeation of various gases through spiro-based PIMs measured at 35 °C and 2 bar upstream pressure with vacuum downstream.	104
<b>Table 4.4.</b> Solubility and diffusivity of ethylene and ethane in various PIMs, measured at 35°C and 2 bar upstream pressure.	105
<b>Table 5.1.</b> Permeation data of PIM-1 prepared under different protocols.	116
<b>Table 5.2.</b> Bulk density and internal surface area of PIM-1 and its CMS derivatives.	123
<b>Table 5.3.</b> Parameters obtained from fitting experimental ethylene and ethane sorption data to the dual-mode (polymers) and the Langmuir isotherms (carbons).	126
<b>Table 5.4.</b> Pure-gas permeability, diffusivity and solubility coefficients of ethylene and ethane at 35 °C and 2 bar for heat-treated PIM-1 and its CMS derivate samples.	127
<b>Table 6.1.</b> Gas permeation properties of thermally annealed PIM-6FDA-OH measured at 2 bar and 35 °C.	140
<b>Table 6.2.</b> Parameters obtained from fitting experimental data to the dual-mode (pristine PIM-6FDA-OH) and the Langmuir isotherms (carbons).	152
<b>Table 7.1.</b> Bulk density and internal surface area of the spirobisindane-based polyimides and its heat-treated derivatives.	172
<b>Table 7.2.</b> Parameters obtained from fitting experimental data to the dual-mode (pristine PIM-6FDA) and the Langmuir isotherms for CMS membranes. <sup>a</sup>	182
<b>Table 7.3.</b> Pure-gas transport properties at 35 °C and 2 bar driving-force for heat-treated PIM-6FDA and its CMS samples.	184

## LIST OF FIGURES

<b>Fig. 1.1.</b> Ethylene production breakdown by country. ....	17
<b>Fig. 1.2.</b> Process diagram of ethylene production via steam cracking. ....	19
<b>Fig. 1.3.</b> Size and reflux ratio of a distillation column required to separate a 1:1 binary feed of ethylene/ethane into grade 4 pure streams. ....	20
<b>Fig. 1.4.</b> Schematic representation of a single membrane stage. The more permeable ethylene molecules are concentrated in the permeate stream, while ethane remains in the retentate stream. ....	22
<b>Fig. 1.5.</b> Schematic representation of asymmetric (left) and composite (right) membranes [46]. ....	23
<b>Fig. 1.6.</b> Membrane area and pressure ratio influence on the permeate concentration. A single permeation stage of a 1:1 binary mixture was simulated. The membrane had a fixed selectivity of 10 and a thickness of 1 $\mu\text{m}$ . ....	25
<b>Fig. 1.7.</b> Existing membrane module configurations [51]. ....	26
<b>Fig. 1.8.</b> Possible configurations of a hybrid membrane system with a distillation column [59]. ....	28
<b>Fig. 1.9.</b> Examples of membrane materials. ....	30
<b>Fig. 1.10.</b> Qualitative cost versus performance relationship of major membrane materials (courtesy of Prof. William Koros, Georgia Institute of Technology). ....	30
<b>Fig. 1.11.</b> Theoretical upper bound of ethylene/ethane separation performance reported by Koros and Rungta [85]. ....	32
<b>Fig. 1.12.</b> Schematic structure of ortho-XH-functionalized polyimides as they are transformed into PBO. ....	36
<b>Fig. 1.13.</b> Idealized pore of a CMS (left) [116]. The critical dimensions $d_c$ are responsible for the selective diffusion of molecules into the pores. The turbostratic graphene wall (right) was modeled by [124]. ....	37
<b>Fig. 1.14.</b> CMS membranes for ethylene/ethane separation [117-123]. ....	37
<b>Fig. 2.1.</b> Relevant transport mechanisms for gas separation. (i) Knudsen flow, (ii) molecular sieving, and (iii) solution-diffusion mechanism. Adapted from [7]. ....	50
<b>Fig. 2.2.</b> Gas diffusion in one dimension through a film of thickness $l$ [4]. ....	52
<b>Fig. 2.3.</b> The change in the specific volume of a polymer with varying temperature. The fractional free volume may be observed in polymers cooled below their glass transition temperature. ....	55
<b>Fig. 2.4.</b> Schematic representation of non-connected (left) and interconnected (right) <i>FFV</i> as a consequence of inefficient chain packing. ....	57
<b>Fig. 2.5.</b> Evolution of PIM materials: (i) original ladder spiro-contorted PIM-1 [33], (ii) PIM-polyimide with contortion centers [35], (iii) OH-functionalization of PIM-polyimide [36], and (iv) ladder polymer with more rigid spiro/Tröger's base contortion centers [37]. ....	57
<b>Fig. 2.6.</b> Transport of small penetrant molecules in the vicinity of two polymeric chains: (i) chains surround the penetrant molecule and (ii) statistical gap opens to allow the diffusion jump of the molecule. ....	58
<b>Fig. 2.7.</b> Gas uptake in the Henry's and Langmuir sorption modes. ....	60

<b>Fig. 2.8.</b> Chemical structure of representative polyimides that were used to construct the ethylene/ethane upper bound: (i) 6FDA-NDA [48], (ii) 6FDA-Durene [49], (iii) 6FDA-TrMPD [49], (iv) BPDA-TeMPD [49], (v) 6FDA-mPD [50].	62
<b>Fig. 2.9.</b> The schematic structures of disordered carbon and regular graphite structure [63].	63
<b>Fig. 2.10.</b> Critical dimensions of an idealized carbon pore. The critical dimensions, $d_c$ , are the ultra-microporous entrances that lead to the sorption chambers of dimensions $d_T$ . Finally, $d_\lambda$ is related to the fast diffusion jumps in the cavities of the chamber [58].	64
<b>Fig. 2.11.</b> Pyrolysis protocol effect on carbon ultramicroporous cavities [58, 68, 69].	65
<b>Fig. 3.1.</b> Three-zone pipe furnace used to carbonize polymeric membranes.	88
<b>Fig. 3.2.</b> Schematic representation of a pure-gas permeation setup.	90
<b>Fig. 3.3.</b> Schematic representation of a mixed-gas permeation setup.	92
<b>Fig. 4.1.</b> Chemical structures of PIMs evaluated for ethylene/ethane separation presented in this chapter.	101
<b>Fig. 4.2.</b> Existing ethylene/ethane separation data with polymeric membranes. The red circles represent data from non-PIM glassy polyimides [5] whereas the blue triangles represent PIMs containing spiro-contortion centers.	107
<b>Fig. 5.1.</b> Chemical structure of PIM-1.	114
<b>Fig. 5.2.</b> Thermal gravimetric analysis of PIM-1 under an inert N <sub>2</sub> atmosphere at a ramping rate of 3 °C/min. Mass-spectrometry qualitatively depicts H <sub>2</sub> , H <sub>2</sub> O and CO <sub>2</sub> evolution. Shaded areas represent the dominating degradation mechanisms: (i) partial dioxane splitting, ii) complete dioxane and methyl groups degradation, iii) matrix dehydrogenation.	118
<b>Fig. 5.3.</b> FTIR spectra of (a) polymeric heated-annealed PIM-1 and (b) its CMS derivatives.	119
<b>Fig. 5.4.</b> Raman spectra of CMS generated from PIM-1 at 600 and 800 °C.	120
<b>Fig. 5.5.</b> XRD spectra of PIM-1 (250 °C) and cross-linked (400 °C) PIM-1 and its heat-derived CMS analogs (600 and 800 °C).	121
<b>Fig. 5.6.</b> (a) CO <sub>2</sub> sorption isotherms at 0 °C in heated-annealed PIM-1 (250 and 400 °C) and its CMS derivatives (600 and 800 °C). The lower right corner depicts low-pressure sorption. (b) Pore size distribution computed from this sorption data by NLDFT using Micromeritics software version 2.0.	123
<b>Fig. 5.7.</b> (a) Pure-gas sorption isotherms of ethylene at 35 °C in pristine PIM-1-250 °C (■), its cross-linked PIM-1-400 °C derivative (◆), CMS-600 °C (▼) and CMS-800 °C (●) derivatives. Fitted dashed curves follow the dual-mode sorption model for the polymeric PIM-1 and its cross-linked analog samples, whereas the Langmuir model was used to describe sorption in the CMS. (b) Ethylene/ethane solubility selectivity as a function of pressure for all samples.	125
<b>Fig. 5.8.</b> Pure-gas ethylene/ethane permeation properties of heat-derived PIM-1 membranes (stars) from right to left: Pristine thermally annealed at 250 °C, cross-linked at 400 °C followed by CMS produced at 600 °C and 800 °C, respectively. For comparison, previously reported Matrimid® polyimide derived CMS heated to 550 and 800 °C [45]. Shaded areas represent the two main mechanism of carbon tailoring. The polymer upper bound is represented with the bold black line [5].	129
<b>Fig. 6.1.</b> Thermal gravimetric analysis of PIM-6FDA-OH under an inert N <sub>2</sub> atmosphere at a ramping rate of 3 °C min <sup>-1</sup> . Mass-spectrometry qualitative depicts H <sub>2</sub> O and CO <sub>2</sub>	

evolution. Four different stages of degradation can be detected (a) limit of thermal stability, (b) polybenzoxazole formation, (c) degradation into amorphous carbon, (d) sintering of CMS.....	141
<b>Fig. 6.2.</b> FTIR spectra of PIM-6FDA-OH and derived PBO: (a) represents hydroxyl groups, (b) methyl stretch that remain unchanged after the PBO formation, (c) and (e) decrease representing the imide stretch; lastly, PBO characteristics peaks: (d) and (f) are shown after the film was treated at 400 °C.....	142
<b>Fig. 6.3.</b> FTIR spectra of PIM-6FDA-OH and derived heat-treated samples.....	143
<b>Fig. 6.4.</b> (a) Weight loss of PIM-6FDA-OH for each isothermal stage of degradation. Shaded areas show the dominating porosity evolution mechanisms during heat treatment while the dashed line was the actual soak time used in the pyrolysis protocol; (b) XRD spectra of all samples. ....	144
<b>Fig. 6.5.</b> Raman spectrum becomes active at 500 °C due to the growth of carbonaceous domains in the CMS samples as elucidated with the D and G peaks (dashed lines).....	145
<b>Fig. 6.6.</b> Heat treatment of PIM-6FDA-OH. At 600 °C the thermally rearranged PBO structure degrades into turbostratic graphene layers that sinter as the pyrolysis temperature increases. Non-carbon impurities (as significant as 10% molar [48]) are contained within the honeycomb array of the turbostratic graphene sheets (generated in Material Studio, version 8.0). ....	146
<b>Fig. 6.7.</b> Physisorption of CO <sub>2</sub> at 0 °C in PIM-6FDA-OH and its heat-derived CMS membranes. Low-pressure sorption is shown in the upper left corner of the graph. ....	147
<b>Fig. 6.8.</b> PSD from the NLDFT method derived from CO <sub>2</sub> sorption data at 0 °C for the pristine PIM-6FDA-OH conditioned at 250 °C and its derived CMS samples. ....	148
<b>Fig. 6.9.</b> Schematic pore evolution of PIM-6FDA-OH and its heat-derived CMS samples. The red arrow represents the critical dimension $d_c$ of ultramicropores, which determines the molecular sieving behavior of the membranes. ....	149
<b>Fig. 6.10.</b> Pure-gas ethylene/ethane permeation properties of CMS membranes derived from PIM-6FDA-OH. The polymer upper bound is represented with the bold black line [10].....	150
<b>Fig. 6.11.</b> Pure-gas sorption isotherms of (a) ethylene and (b) ethane at 35 °C in PIM-6FDA-OH and its CMS derivatives. Fitted dashed curves follow the dual-mode sorption model for the polymeric PIM-PI annealed at 250 °C, whereas the Langmuir model was used to describe sorption in the CMS samples. ....	152
<b>Fig. 6.12.</b> Solubility of ethylene and ethane in PIM-6FDA-OH (●) and its CMS (▲) derivatives at 35 °C and 2 bar. ....	154
<b>Fig. 6.13.</b> Diffusivity of ethylene and ethane in PIM-6FDA-OH (●) and its CMS (▲) samples at 35 °C and 2 bar.....	155
<b>Fig. 6.14.</b> Ethylene/ethane diffusivity and solubility selectivities in PIM-6FDA-OH (●) and its CMS derivatives (▲). The fitted lines are drawn to guide the eye. ....	156
<b>Fig. 6.15.</b> (a) Pressure dependence of the mixed-gas transport properties of a 1:1 ethylene/ethane binary mixture and (b) time required to reach pseudo-equilibrium at each pressure for the CMS membrane heat-treated at 800 °C derived from PIM-6FDA-OH. ....	157
<b>Fig. 6.16.</b> Single ethylene permeability and ethylene/ethane selectivity of CMS derived from PIM-6FDA-OH (red closed squares). Mixed-gas selectivity dropped from 14 to 8.3 as the feed pressure was increased from 4 to 20 bar (open squares). Matrimid® polyimide-based CMS (blue) pure-gas permeation at 35 °C and 3.4 bar [41].....	158

<b>Fig. 7.1.</b> Chemical structure of: a) PIM-1; b) PIM-6FDA-OH; c) PIM-PBO d) PIM-6FDA.....	170
<b>Fig. 7.2.</b> Weight loss and mass spectra of evolved gases during the degradation of a) PIM-6FDA and b) PIM-6FDA-OH. Ramping rate 3 °C/min under N <sub>2</sub> atmosphere.....	174
<b>Fig. 7.3.</b> Raman spectra of CMS generated from PIM-6FDA at 500, 600 and 800 °C. D and G peaks indicate amorphous graphene configurations are marked with dashed lines. ....	174
<b>Fig. 7.4.</b> Weight loss of PIM-6FDA for each isothermal stage of carbonization. Shaded areas show the dominating porosity evolution mechanisms during heat treatment while the dashed line was the actual soak time used in the pyrolysis protocol. ....	175
<b>Fig. 7.5.</b> FTIR spectra of PIM-6FDA and derived CMS membranes at 500, 600 and 800 °C. ....	175
<b>Fig. 7.6.</b> XRD spectra of PIM-6FDA (pristine PI) and CMS membranes for each isothermal stage of carbonization. ....	176
<b>Fig. 7.7.</b> Physisorption of CO <sub>2</sub> at 0 °C in PIM-6FDA and its heat-derived CMS membranes. Low-pressure sorption is shown in the upper left corner of the graph.....	178
<b>Fig. 7.8.</b> PSD of 250 °C annealed PIM-6FDA and CMS samples heat-treated at 500, 600 and 800 °C.....	179
<b>Fig. 7.9.</b> Pure-gas sorption isotherms of (a) ethylene and (b) ethane at 35 °C in PIM-6FDA and its CMS derivatives. Fitted dashed curves follow the dual-mode sorption model for the polymeric PIM-PI annealed at 250 °C, whereas the Langmuir model was used to describe sorption in the CMS samples.....	181
<b>Fig. 7.10.</b> Pure-gas ethylene/ethane permeation properties of CMS membranes derived from PIM-6FDA (2 bar; 35 °C). The polymer upper bound is represented with the bold black line [10]. ....	185
<b>Fig. 7.11.</b> Pressure dependence of the mixed-gas permeation properties of 800 °C-treated CMS membranes derived from PIM-6FDA using a 1:1 v/v ethylene/ethane binary mixture at 35 °C.....	186
<b>Fig. 7.12.</b> Time dependence of the mixed-gas permeation properties of 800 °C-treated CMS membranes derived from PIM-6FDA using a 1:1 v/v ethylene/ethane binary mixture at 35 °C.....	187
<b>Fig. 8.1.</b> Intermediate carbon region. Data underneath the polymer upper bound represents pristine Matrimid® 6FDA-DAM, PIM-6FDA-OH and PIM-1. Data above the tradeoff represent carbons generated between 600-675 °C [3-5]. ....	196
<b>Fig. 8.2.</b> Schematic representation of the ultramicroporous selective CMS pores (d <sub>ci</sub> ) as they remain: (a) unaltered by condensable molecules and (b) dilate slightly allow permeation of bulkier molecules.....	198

## Chapter 1

### **Ethylene/Ethane Membrane Separation: Beyond Conventional Distillation Processes**

Traditional equilibrium-based distillation methods have been reliably implemented since the early 1900s to purify ethylene from ethane. Although improvements have been made in their overall design, distillation cost has remained high due to its unavoidable relation to the latent heat of vaporization. In contrast, membrane separations do not require phase changes so avoid this energy cost. However, membranes have not reached commercial status for olefin/paraffin applications yet, mainly due to material performance limitations. In this chapter, advanced intrinsically microporous polymers and their heat-derived products are proposed as valuable candidates to generate dependable, affordable membranes that could lead to a paradigm shift that reduces ethylene/ethane distillation costs.

### *1.1 Ethylene: the most important building block in the petrochemical industry*

The fossil-fuel-powered industrialization and mass production of goods and food also brought new challenges, including scarcity of non-renewable resources [1], unacceptable pollution levels in major cities [2], and climate change [3, 4]. Consequently, industry is searching for technologies that reduce energy expenditures and environmental impact [5]. As expected, there has been an enormous effort to develop alternative fuels [6], as well as novel strategies to harness the power of sustainable natural sources, such as sun [7] and wind [8]. However, the combined demand for oil, carbon and natural gas has been predicted to remain dominant in the foreseeable future, as no other substitute has been found capable of reliably offering the same net energy returns [9].

The petrochemical sector has diversified its products significantly since its foundation 150 years ago. The first refined oil components were directly used to provide light and heat [10], and later on, through catalytic reactions, they were turned into more useful liquid and gas fuels that made steam machines obsolete [11]. Further advances led to the production of small-chain olefins that were implemented as building blocks and precursors in a broad range of products. Plastics, synthetic fibers, surfactants, and pharmaceuticals were then obtained from ethylene, whose simple unsaturated organic structure of two carbons allowed for a commendable versatility of synthesis [12].

Nowadays, 150 million tons of ethylene are produced per year – more than any other organic compound [13]. Production of ethylene can be related to around 8% of the total energy consumption in the industrial sector [14]. Approximately 60% of ethylene produced is used to make polyethylene. Ethylene oxide (precursor of ethylene glycol), ethyl benzene, and ethylene dichloride are important intermediates that demand this olefin



as well. Ethylene production facilities are mainly clustered in Saudi Arabia, China, Japan, and the USA, as shown in **Fig. 1.1**. The largest industrial complexes have capacities ranging from 1–4 million tons ethylene produced per year as shown in **Table 1.1**. These macro-complexes could be the pivotal points for immense opportunities of technology application.

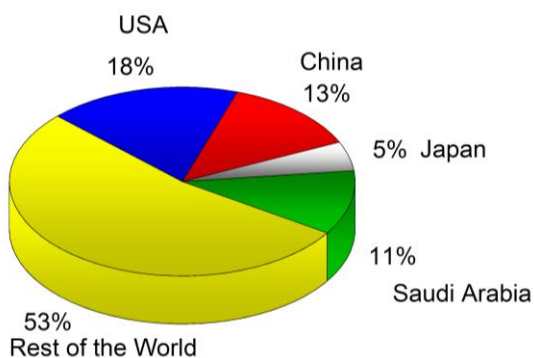


**Fig. 1.1.** Ethylene production breakdown by country.

**Table 1.1.** Largest ethylene production facilities in the world [15].

Company	Location	Capacity (tpy)
ExxonMobil Chemical	Jurong Island, Singapore	3 500 000
Formosa Petrochemical	Taiwan, China	2 935 000
Nova Chemicals	Joffre, Canada	2 811 792
Arabian Petrochemical	Jubail, Saudi Arabia	2 250 000
ExxonMobil Chemical	Baytown, United States	2 197 000
Chevron Phillips Chemical	Sweeny, United States	1 865 000
Dow Chemical	Terneuzen, Netherlands	1 800 000
Ineos Olefins & Polymers	Chocolate Bayou, United States	1 752 000
Equistar Chemicals LP	Channelview, United States	1 750 000

## 1.2 *Steam Cracking*

Ethylene is produced by a process called *steam cracking* [16]. Liquid or gaseous naphtha and ethane are typically used as feedstocks [17, 18], with naphtha more common due to its lower cost. The overall process diagram is shown in **Fig. 1.2**. The feed stream is heated by steam in the absence of oxygen until it reaches its pyrolysis point. The pyrolysis furnace turns the larger molecules from the feed into smaller unsaturated molecules. Small molecules such as hydrogen, carbon dioxide, methane, ethylene and acetylene are produced instantly. This product stream is segregated into two phases: (i) the condensable fraction, which is later used as fuel; and (ii) the gaseous remainder, which goes through a series of compressing stages for further separation.

The gaseous stream that leaves the furnace needs to be cooled down before the removal of acid gases and moisture. The last stage involves the systematic separation of hydrocarbons by thermal means, where small differences in volatility are exploited. Distillation columns are proven technologies that, in spite of their high cost and bulk, produce streams with very high purity [19].

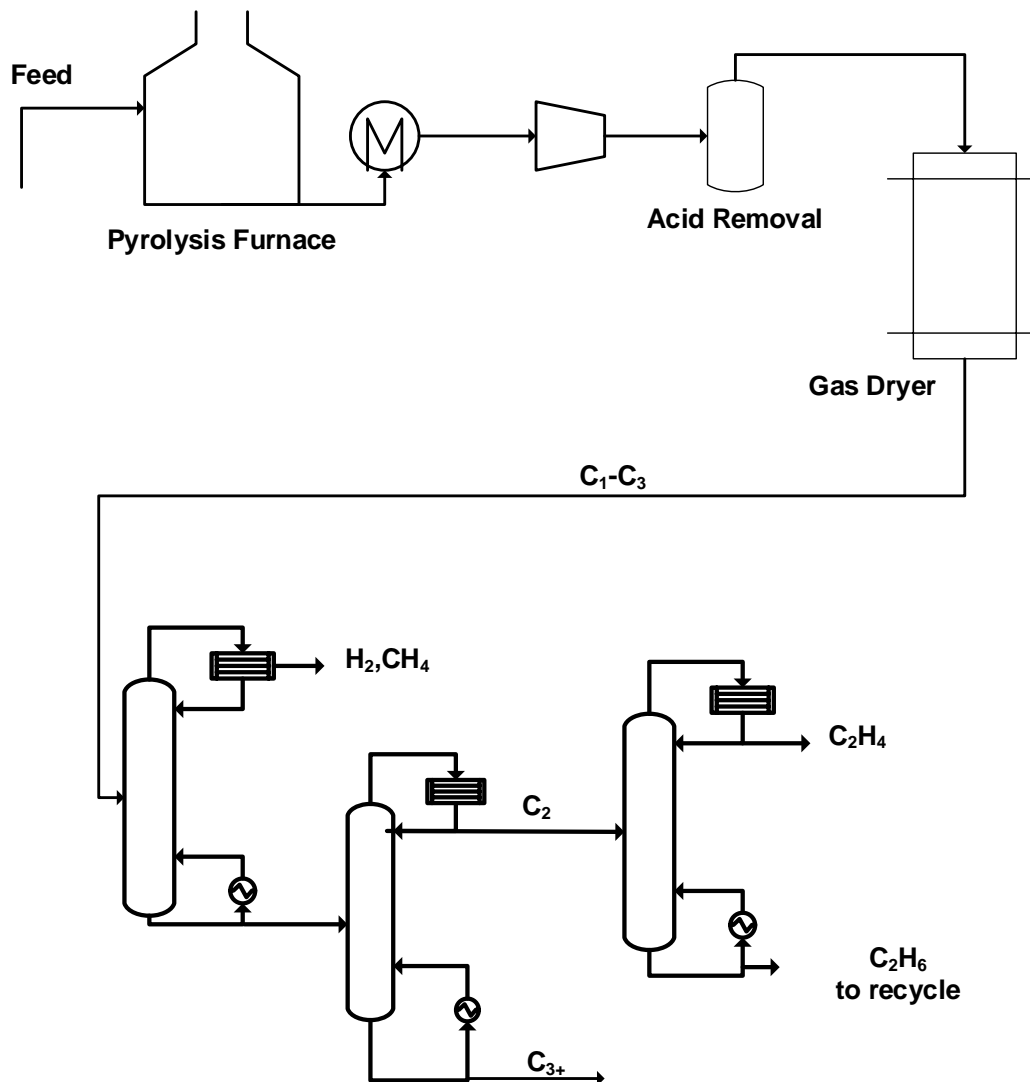


**Fig. 1.2.** Process diagram of ethylene production via steam cracking.

### 1.2.1 Conventional ethylene/ethane distillation column

The distillation column is the heart of the hydrocarbon separation train of a steam cracking facility. This separation is particularly difficult because it is based on the very small difference in volatility of the compounds involved. The normal boiling point of ethylene is  $-103.9\text{ }^{\circ}\text{C}$  while ethane is slightly more condensable at  $-88.3\text{ }^{\circ}\text{C}$  [20]. All the

points of the surface shown in **Fig. 1.3** represent feasible distillation columns that produce grade 4 pure gases (i.e. tops and bottoms with molar concentrations of over 99.99%). The required size of the column will vary with its pressure profile and reflux ratio. In actual practice, the ethylene/ethane distillation takes place at low temperatures in the range of -10 °C to -30 °C at pressures of ~20 bar [21]. Over the last 100 years, these distillation systems have been the subject of numerous revisions to enhance their operating efficiency [22-25]. In spite of their gradual optimizations, the energy spent in an ethylene/ethane distillation column has remained high, as it has been estimated that around 0.16 EJ of energy are annually consumed in this single application. Moreover, distillation towers are often 100 m tall since more than 100 equilibrium stages are needed to obtain the necessary purity in the product streams [26]. Overall, ethylene separation from ethane is very expensive in terms of both operational and capital costs.

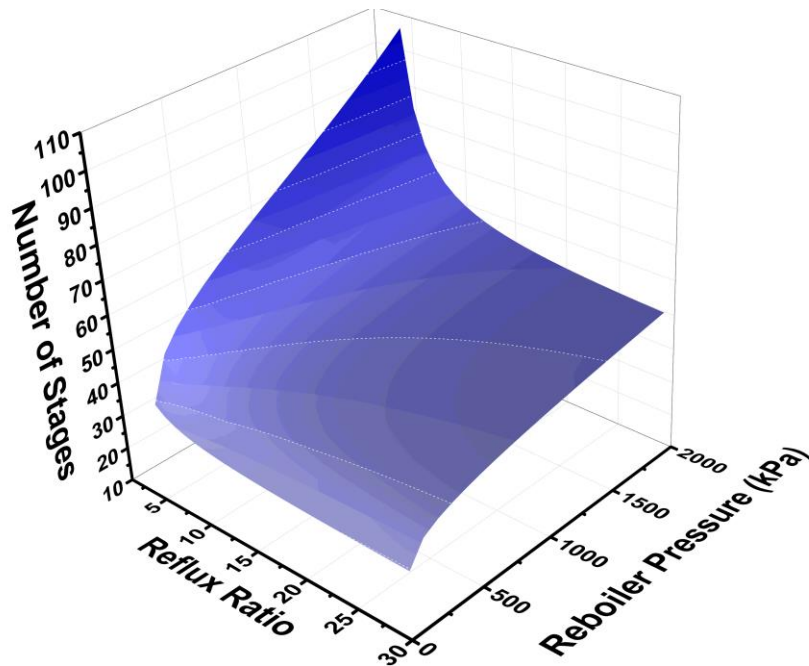


**Fig. 1.3.** Size and reflux ratio of a distillation column required to separate a 1:1 binary feed of ethylene/ethane into grade 4 pure streams.

### 1.3 *Novel membranes: technology for a new age of gaseous hydrocarbon separation*

Synthetic membranes are inspired by their biological counterparts: thin layers with separating properties. Ideally, a membrane can be tailored so that it discriminates even the smallest of the molecules, such as gases and ions [27]. Membrane processes for gas applications are driven by partial pressure differences between the upstream and downstream side of the membrane. Potentially, a membrane can reduce the energy costs needed to separate molecules by a factor of 10 if compared to conventional thermally-based processes [28]. Membranes have found roles in various advanced applications such as water desalination, natural gas treatment, artificial kidneys, and nitrogen purification from the air [29]. The total membrane market value is expected to reach 40 billion U.S. dollars worldwide by 2019 [30].

In principle, a gas separation membrane system could outperform a thermal process because two tunable parameters can be influenced to segregate a mixture of gases (i.e. instead of volatility alone in the distillation base case). The first parameter is the affinity between the gas and the membrane material itself. This affinity is typically defined in terms of the gas solubility in the membrane medium ( $S$ ) and it scales with the inherent gas condensability [31]. The other variable is the gas diffusion coefficient ( $D$ ) through the membrane matrix that is strongly affected by the size of the permeant molecules. According to the solution-diffusion model [32], the gas selectivity of a membrane material is estimated as follows:

$$\alpha_{i/j} \equiv \frac{P_i}{P_j} = \frac{D_i S_i}{D_j S_j}$$

Essentially, membranes discriminate between molecules with different permeation rates. The membrane selectivity ( $\alpha$ ) is the ratio of permeability of the various components traversing its structure. In other words, the membrane selectivity is a measure of the ability of the material itself to separate one component from another. The productivity of the membrane is closely related to its permeability ( $P$ ), and needs to be high to minimize membrane area requirements, since the flux for a given membrane thickness is proportional to the permeability of the material.

Membrane technology for industrial applications requires an affordable material that satisfies the separation task, minimizes energy consumption compared to distillation techniques, has a long life before replacement is needed, is environmentally benign, and does not require heavy maintenance [33]. A schematic representation of a single membrane stage for ethylene purification from ethane is shown in **Fig. 1.4**. The gas permeation across the membrane is perpendicular to the feed flow.

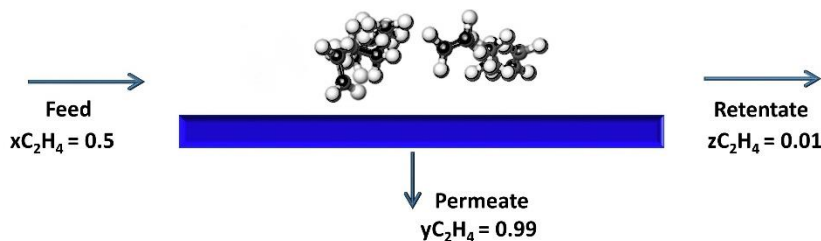


**Fig. 1.4.** Schematic representation of a single membrane stage. The more permeable ethylene molecules are concentrated in the permeate stream, while ethane remains in the retentate stream.

#### 1.4 Membrane process design

The design of a new membrane process intended for commercial purposes should follow this procedure [34]: (i) material development, (ii) thin layer formation, (iii) module construction. The first step mainly relies on the screening of the newest and most advanced materials that have both high selectivity and permeability [35]. The second step demands materials of solution processability that allows the formation of thin selective layers. The separation layer needs to be thin (e.g. 10-1000 nm) to not compromise the membrane flux. Several techniques have emerged to fabricate thin films composite and asymmetric membranes [36-41], since the times of the pioneering work of Loeb and Sourirajan [42]. In **Fig. 1.5**, generic composite and asymmetric membrane structures are shown. Composite membranes require the selective layer to be supported on a porous substrate that provides mechanical resistance whereas asymmetric membranes are made of only one material. The former are preferred since thin-film composite membranes allow the optimization of the various layers individually [43-45]. Furthermore, the selective layer tends to be more expensive than the support; thus, there is a double incentive to minimize its thickness.

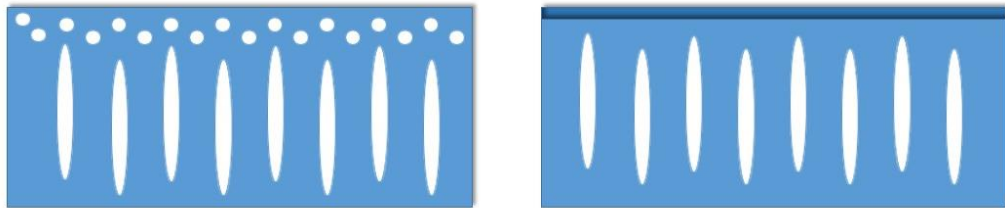


**Fig. 1.5.** Schematic representation of asymmetric (left) and composite (right) membranes [46].

It is important to note that the selectivity of the membrane material provides only a rudimentary initial assessment of the performance of the final membrane module. The design of industrially meaningful membranes entails the knowledge of the limit on separation performance imposed by economically reasonable driving forces [47]. The effect of the pressure ratio on permeate purity is simply represented as follows:

$$y_p = \frac{\phi}{2} \left[ y + \frac{1}{\phi} + \frac{1}{\alpha - 1} - \sqrt{\left( y + \frac{1}{\phi} + \frac{1}{\alpha - 1} \right)^2 - 4 \frac{\alpha y_f}{(\alpha - 1)\phi}} \right]$$

where  $y_p$  is the concentration of the faster component in the permeate,  $y_f$  is the concentration in the feed, and  $\phi$  is defined as the pressure ratio of the feed relative to the permeate. **Fig. 1.6** depicts the effect of pressure ratio and membrane area on ethylene permeate concentration after a single-stage membrane unit. For pressure ratios higher than 1, selective permeation of ethylene takes place. Therefore, a membrane with an infinitesimal area would produce the most concentrated permeate possible, limited only by the material selectivity ( $\alpha$ ). A hypothetical membrane material of  $\alpha = 10$  could only produce a 91% ethylene-pure permeate in one permeation stage which is below polymer-grade quality requirements. Furthermore, a larger-sized stage always produces a permeate stream with a higher concentration of the slower and bulkier ethane molecules. The ultimate membrane configuration may require multiple membrane stages with a recycling stream to achieve the desired separation task.



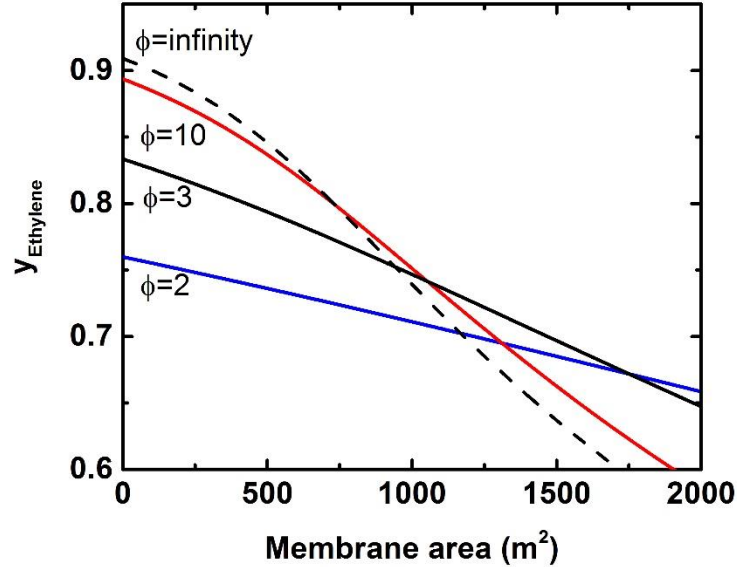


**Fig. 1.6.** Membrane area and pressure ratio influence on the permeate concentration. A single permeation stage of a 1:1 binary mixture was simulated. The membrane had a fixed selectivity of 10 and a thickness of 1  $\mu\text{m}$ .

Cost-effective membrane processes require modules that maximize surface area to volume ratio. The preferred modules in industry are the spiral wound and hollow fiber, which can offer higher surface area per unit volume than the standard plate-and-frame membrane, as shown in **Fig. 1.7**. Indeed, hollow fiber commercial modules provide area densities up to 30 000  $\text{m}^2 \text{m}^{-3}$  [48], which is why they are used in nearly 90% of the gas separation applications in the membrane industry [49]. Once a reliable module has been exposed to realistic testing conditions, a small size pilot plant can be proposed to test a system in the field [50].

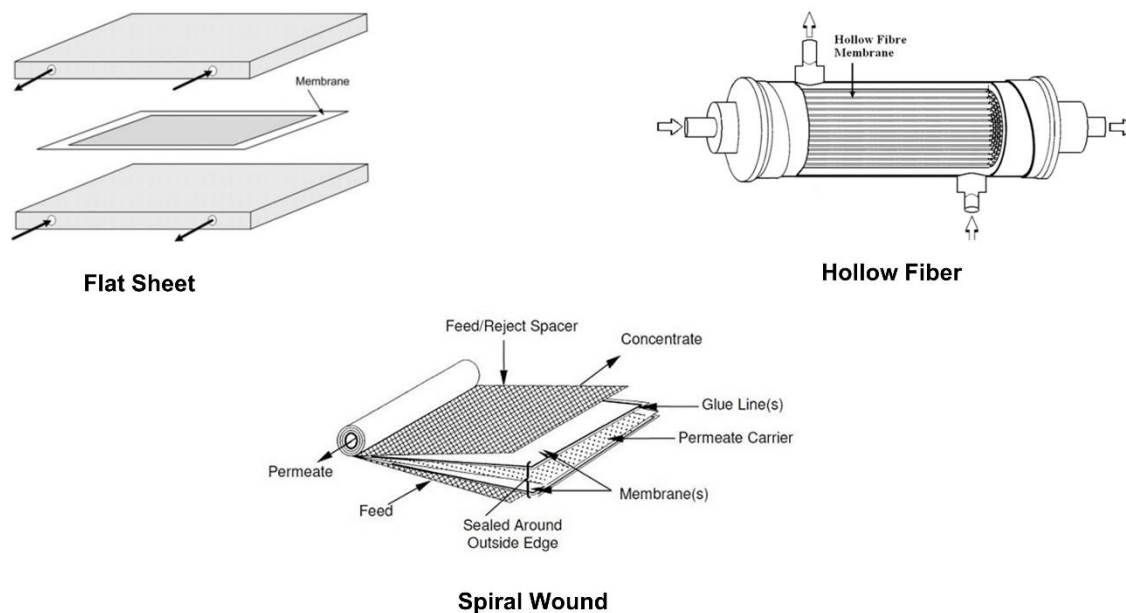


**Fig. 1.7.** Existing membrane module configurations [51].

### 1.5 *Retrofitting of an ethylene/ethane distillation column with an advanced membrane module*

To date, membrane technology has not been commercialized for ethylene/ethane separation. Ethylene and ethane have very similar physical properties that make this separation extremely challenging even for membranes. As shown in **Table 1.2**, ethylene is slightly smaller due to its double bond, which causes its structure to be slimmer and flat. Ethane has a higher critical temperature of 31.9 °C compared to ethylene of 9.1 °C. Thus, traditional polymeric membranes have only provided modest pure-gas selectivities (i.e.  $\alpha < 7$ ) [52-57]. Notwithstanding, process simulations have predicted a significant economic incentive if a hybrid membrane distillation system is used instead of distillation alone [58-

60]. The distillation column and a membrane stage could form a superstructure with various configurations: (i) the membrane before the column, (ii) parallel to the column, (iii) after the reboiler, or (iv) before the condenser, as schematically depicted in **Fig. 1.8**. Estimates of the quantitative savings resulting from the synergistic membrane/column approach have varied significantly with the transport properties of the membrane material, its associated cost, as well as the actual models and assumptions built into the transport equations [59, 61-64]. However, the following qualitative advantages compared to the base case of the distillation column by itself were observed:

- Reduction on the heat duty of the column
- System versatility to adapt to changes in feed concentration
- Possibility for a throughput increase (or decrease) without sacrificing the purity of the product

**Table 1.2.** Physical properties of ethylene and ethane [65].

Gas	Molecular mass (g mol <sup>-1</sup> )	LJ diameter (Å)	Critical temperature (°C)
C <sub>2</sub> H <sub>4</sub>	28	4.16	9.1
C <sub>2</sub> H <sub>6</sub>	30	4.44	31.9

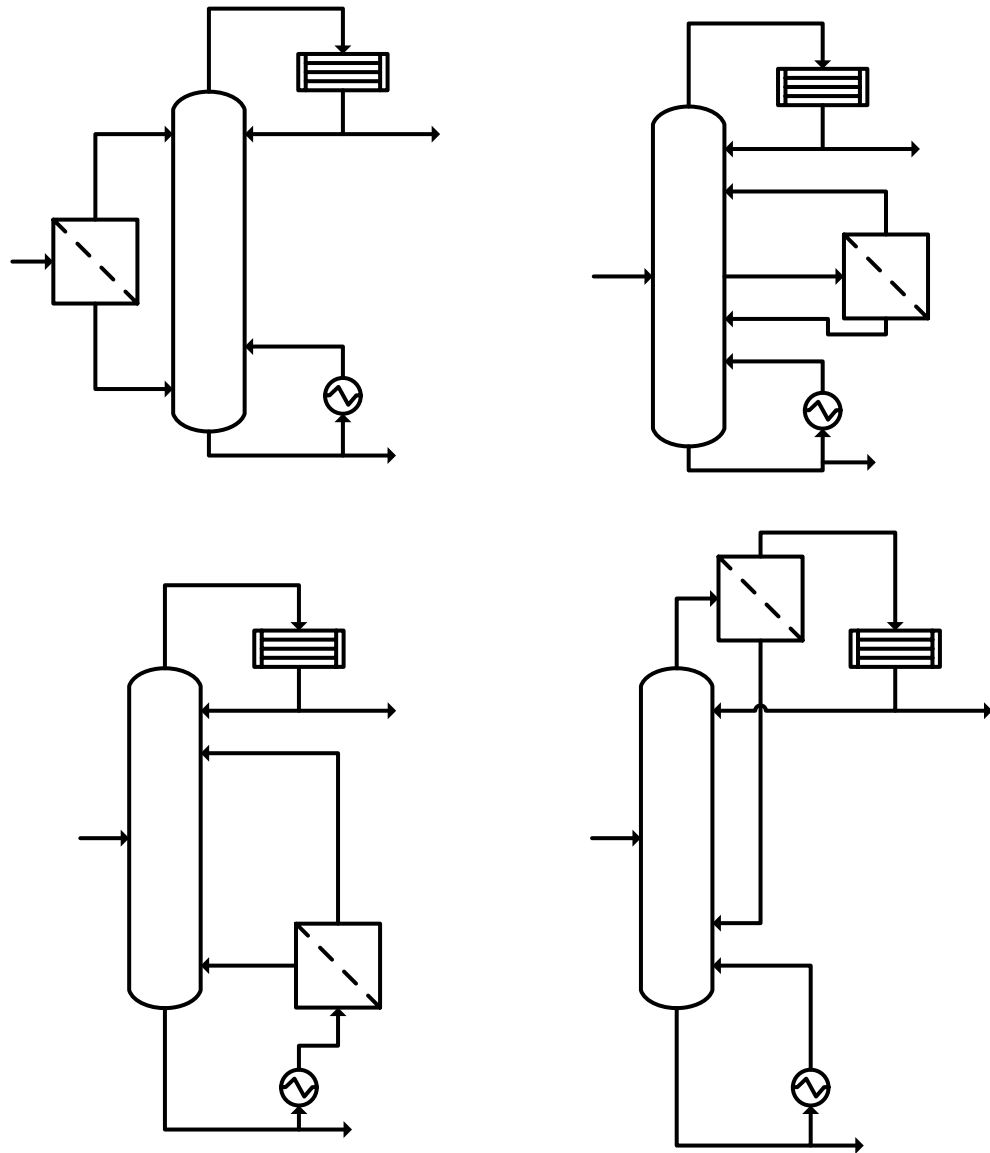


**Fig. 1.8.** Possible configurations of a hybrid membrane system with a distillation column [59].

According to Baker, an ethylene/ethane selectivity of 15 or above should be a potential candidate for commercial hybrid distillation olefin/paraffin applications [66]. New materials are needed to debottleneck this challenging hybrid application [67].

## 1.6 Membrane materials

Membranes may be fabricated with organic or inorganic materials. Some examples of generic membrane materials are shown in **Fig. 1.9**. Inorganic materials are ceramics, carbons, and metals while organic materials mainly comprise polymers. The classic structural difference between polymers and inorganics is their respective pore size distribution (PSD), a key parameter for molecular size discrimination [68-71]. In addition, polymers are known to be less resistant to condensable-gas-induced swelling effects compared to their inorganic counterparts [72]. Essentially, inorganics usually have higher performance and higher cost compared to polymer alternatives. In spite of their extraordinary inherent properties, pure inorganic membranes have been all but precluded from commercial applications, whereas polymeric selective layers fabricated with cellulose acetate, polysulfone, and some cross-linked polyimides have so far achieved mainstream status in membrane technology. Between the two extremes of pure inorganic and pure polymeric membranes lie the mixed-matrix systems [73] and the carbon molecular sieves derived from organic precursors [74]. The mixed-matrix membranes are traditionally fabricated by dispersing inorganic (or at least *partially* inorganic [75]) particulates into a polymeric medium [76]. A mixed-matrix system is intended to have superior selectivities compared to those of the polymeric base, which is commonly achieved by adding porous fillers with molecular sieving properties [77]. Finally, carbons can be simply generated from a polymeric precursor through an atmospheric-controlled pyrolysis protocol [78]. Like zeolites, carbons have been acclaimed for their excellent size-discrimination

capabilities [79]. They may offer a sweet spot between performance and practical cost, as shown in **Fig. 1.10**.

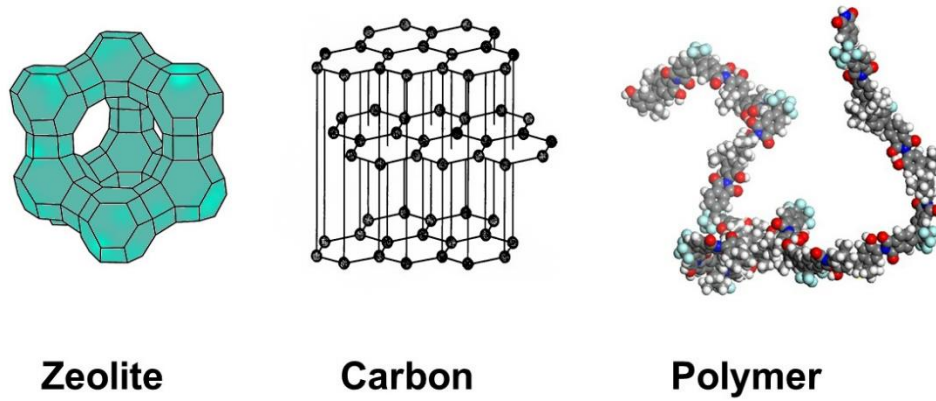


**Fig. 1.9.** Examples of membrane materials.

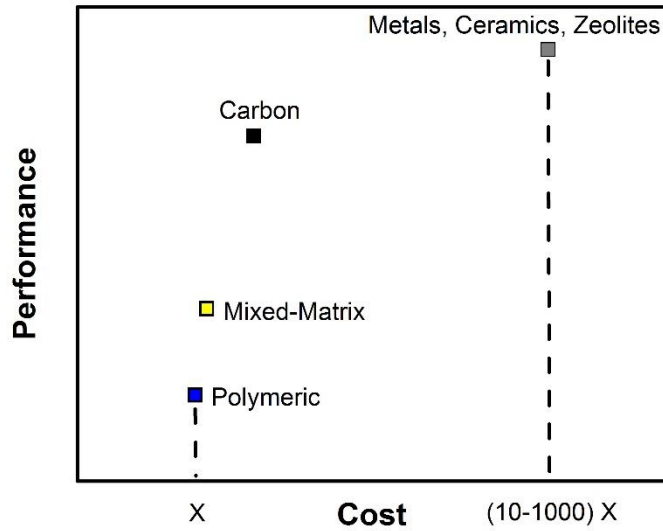


**Fig. 1.10.** Qualitative cost versus performance relationship of major membrane materials (courtesy of Prof. William Koros, Georgia Institute of Technology).

### *1.6.1 Current polymers that define the performance upper bound of organic membranes*

Polymeric materials constitute the bulk of commercially produced membranes. Accordingly, the synthesis of advanced gas-selective materials demands profound knowledge of their physical properties and their interaction with the permeation mechanisms of gas molecules [80]. Earlier studies concluded that polymers below their glass transition temperature (i.e. glassy polymers) would have limited chain mobility compared to their rubbery analogues that lie above their glass transition temperature [81]. The relatively stable glassy matrices would provide better molecular size-discrimination compared their rubbery polymers counterparts [82].

In agreement with the phenomenological behavior observed for other gas pairs [83], the ethylene/ethane selectivity that a polymeric material can achieve decreases with increasing permeation rate [52], a relationship that holds a linear trend in a  $\log(P)$ - $\log(\alpha)$  scale. Accordingly, all polymeric performance data have been categorized under a limit upper bound, as shown in **Fig. 1.11**. Prominently, the best of the polymeric membranes for ethylene/ethane separation are glassy polyimides based on the 6FDA dianhydride [55, 84], which achieved ideal gas selectivities of  $\sim 7$  at 35 °C and 2 bar upstream pressure.

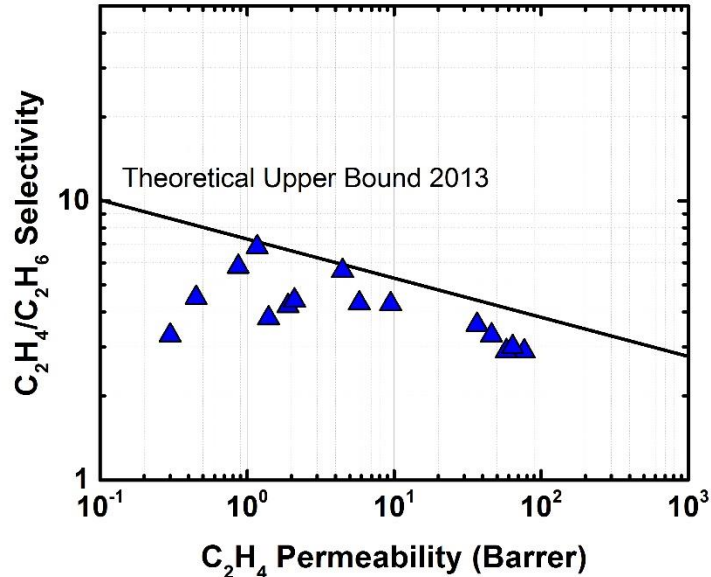


**Fig. 1.11.** Theoretical upper bound of ethylene/ethane separation performance reported by Koros and Rungta [85].

In conjunction with the requirement for a highly-selective membrane for an ethylene/ethane application, exposure to realistic mixed-gas conditions needs to be tested if a viable candidate is to be found. Ethylene and ethane could potentially plasticize a membrane matrix of glassy polymers and decrease separation performance [56]. In addition, part-per-million levels of other condensable molecules, such as water and toluene [86], could preferentially sorb into the membrane, effectively blocking pores relevant for permeation. Regardless, all ethylene/ethane compilation studies so far have excluded the state-of-the-art polymers in gas separation, the so-called polymers of intrinsic microporosity (PIM).



### 1.6.2 PIM polymers: the future of gas separation advanced organic materials

PIMs are organic macromolecules bearing extremely rigid contortion centers (e.g. tetrahedral carbon) that prevent efficient chain-packing in their solid state, thus developing a polymeric matrix of interconnected microporosity ( $< 20 \text{ \AA}$ ) in the form of super-micropores ( $7 \text{ \AA} - 20 \text{ \AA}$ ) and ultra-micropores ( $< 7 \text{ \AA}$ ) [87, 88]. The inner structure of a PIM material can be visualized as a series of constrictions in a void space and their connected chambers that allow a significant surface area for adsorption (typically 200–1000  $\text{m}^2/\text{g}$ ).

A wealth of research has been dedicated to the synthesis of PIM-based materials since the creation of the prototype spirobisindane polybenzodioxane ladder [87, 89, 90] of PIM-1 in 2004 and the incorporation of the spirobisindane moiety into a dianhydride that was the precursor of several polyimides of intrinsic microporosity (PIM-PI) [91, 92], which presented moderate selectivities and commendable versatility of synthesis. The most recent PIMs have been tailored with even less flexible bridge-head bicyclics: Tröger's base, ethanoanthracene, and triptycene moieties, that often surpassed the 2008 polymer upper bound for several important gas pairs [93-96]. In spite of their novelty, PIM polymers have not been reported for ethylene/ethane separation except for PIM-1 itself, which failed to provide sufficient ethylene/ethane separation [97]. Regardless, advanced PIM examples may have the ultra-microporosity needed to size-discriminate ethylene from ethane and reach commercially relevant separation factors.

## *1.7 Strategies to tailor the PSD of advanced PIMs that could enhance the separation performance for the ethylene/ethane gas pair*

### *1.7.1 Pre-synthesis structural modifications that modify chain rigidity and pore tightness*

PIM-PIs have been tailored for the separation of the  $C_3H_6/C_3H_8$  pair by changing the rigidity of their contortion centers, and it was found that the more rigid triptycene-bearing KAUST-PI-1 offered selectivities nearly as high as that of low-free-volume polymers but with unmatched permeabilities [98]. Furthermore, side-groups and functionalities modify the conformation and rigidity of PIM materials in their solid-state. For example, bromine-substituted PMDA-BSBF showed limited torsional mobility of its spirobifluorene moiety which in turn enhanced its chain rigidity and restricted chain packing, thus effectively increasing the polymer permeability with a slight decrease in selectivity compared to its unsubstituted analogue [99]. Furthermore, pendant groups may induce physical crosslinks via intra-chain polar interactions (e.g. hydrogen bonding), which tighten the constricting throats up and enhance the selectivity of various PIM-based membranes [100-103]. Accordingly, novel PIMs could show significant molecular sieving, which is key to separating ethylene from ethane.

### *1.7.2 Thermal annealing*

Heat may be used to densify a polymeric matrix, causing tightening of the cavities responsible for gas discrimination. Because PIM polymers do not have defined glass transition temperatures prior to their main chain decomposition, heating the polymer below

its decomposition temperature is called sub- $T_g$  annealing [104]. As reported previously [105], annealing PIMs increase selectivity with a slight decrease in permeability via charge transfer complex (CTC) formation.

### 1.7.3 Cross-linking

Heating under certain atmospheric conditions can cross-link a PIM-matrix. The structural change in the polymer matrix during a thermal step will depend on the structure of the precursor. For example, PIM-1 has been self-cross-linked under vacuum at 300 °C and showed a 400% increase in CO<sub>2</sub>/CH<sub>4</sub> pure-gas selectivity via triazine formation [106]. A tighter structure, with interconnected cavities, would maximize the diffusion difference between the ethylene/ethane gas pair. Therefore, cross-linked PIMs aimed at ethylene/ethane separation could have a significant impact in the development of industrial membranes.

### 1.7.4 Formation of polybenzoxazole from *ortho*-functionalized PIM-PI

In recent years, *ortho*-functionalized polyimides have been thermally treated to generate more stable polybenzoxazole structures [107-111]. The carbonyl of the polyimide ring reacts with the *ortho*-functionality of the diamine moiety to form polybenzoxazole, releasing CO<sub>2</sub> (**Fig. 1.12**). This molecular rearrangement is known to enhance permeability while reducing selectivity [112, 113]. Small changes in polymer structure can result in substantial changes in the thermally-treated product [114]. This overall procedure would

be beneficial for ethylene/ethane purification if the starting material had very high selectivity, and the degradation did not open up the structure significantly.

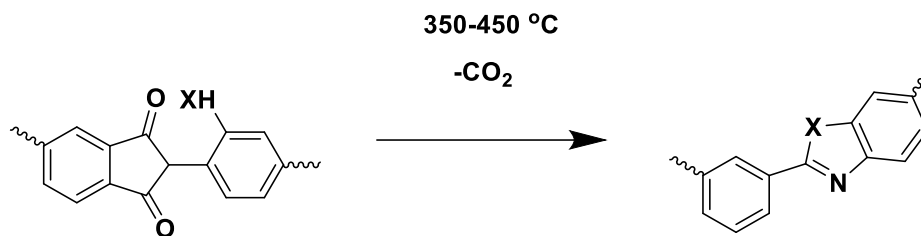


**Fig. 1.12.** Schematic structure of ortho-XH-functionalized polyimides as they are transformed into PBO.

### 1.7.5 Carbonization

Degradation of PIM materials well above their decomposition temperature should produce a carbonized amorphous structure [115]. PIM polymers make ideal substrates for carbonization because of their very high carbon yield and excellent thermal properties. The amorphous graphene sheets of a carbon molecular sieve (CMS) have significant size-discriminating structures [85]. CMS structures are likely to achieve extraordinary selectivity by virtue of their bottlenecked cavities [116], as shown in **Fig. 1.13**. The hypothetical, ultra-microporous, immovable cavities should size-reject any molecule larger than their inner diameter. The ethylene/ethane transport properties of CMS materials surpass the polymeric upper bound due to their high permselectivities [117-123], as shown in **Fig. 1.14**. Polymeric precursors used to generate these carbons have been either

traditional low-free-volume polymers (e.g. Matrimid®) or high-free-volume polymers without contortion centers.

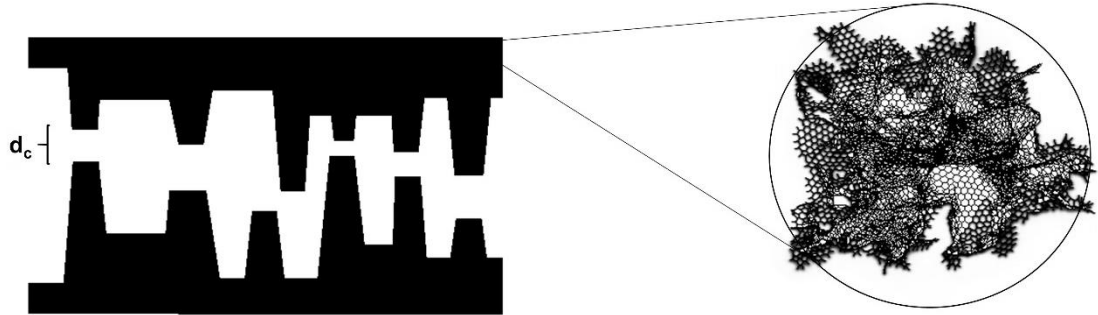


**Fig. 1.13.** Idealized pore of a CMS (left) [116]. The critical dimensions  $d_c$  are responsible for the selective diffusion of molecules into the pores. The turbostratic graphene wall (right) was modeled by [124].

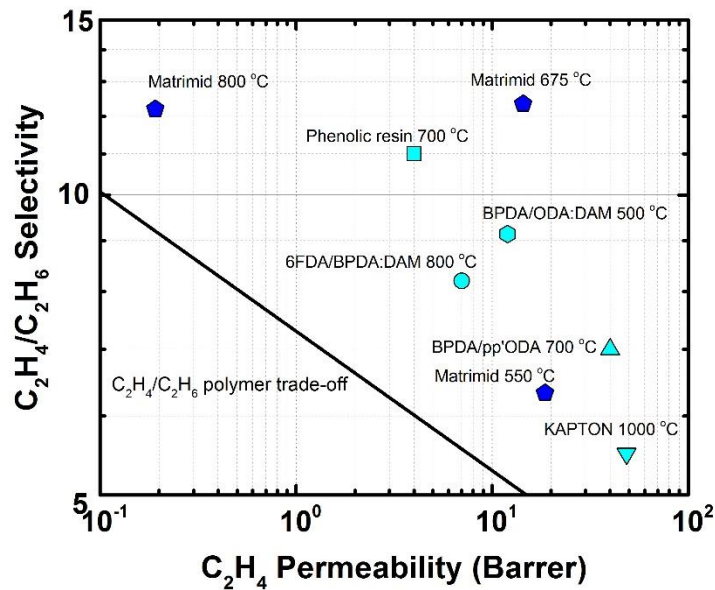


**Fig. 1.14.** CMS membranes for ethylene/ethane separation [117-123].

## 1.8 *Dissertation objectives*

### **Screen advanced intrinsically microporous polymeric materials for ethylene/ethane separation.**

The advantage of PIMs over conventional, low-free-volume polymers is that they may increase the diffusion selectivity of similarly-sized ethylene/ethane while still providing very high permeabilities. Even tests under ideal conditions would elucidate their ethylene/ethane sieving capabilities. In this work, the properties of nine PIM-polymers bearing spiro-contortion centers are reported, to benchmark their performance against conventional low-free-volume polymers. Their rigidity and pore size were modified by using bromine substitutions and hydroxyl functionalities in their backbones.

### **Heat-treatment of advanced PIM substrates to enhance their microporosity**

Polymers taken beyond their onset of decomposition under a fixed set of conditions, such as temperature and pressure, will undergo specific reactions that change their structure in their solid state. In this case, thermolabile PIM polymers were used as substrates for carbonization. A variety of characterization techniques were used to assess the completeness of degradation, the (qualitative) pore-size-distribution and film gas transport properties.

### **Evaluation of advanced CMS membranes for ethylene/ethane separation under realistic mixed-gas testing**

In the presence of gas mixtures, non-ideal effects such as competitive sorption and matrix swelling may reduce membrane selectivity. The best performing carbons derived from

PIM-PIs were tested under binary ethylene/ethane mixtures at pressures representative of real operating conditions.

## 1.9 References

- [1] F. Holz, P.M. Richter, R. Egging, A global perspective on the future of natural gas: resources, trade, and climate constraints, *Rev. Environ. Econ. Pol.*, (2015).
- [2] X. Han, L.P. Naehar, A review of traffic-related air pollution exposure assessment studies in the developing world, *Environ. Int.*, 32 (2006) 106-120.
- [3] C. Parmesan, G. Yohe, A globally coherent fingerprint of climate change impacts across natural systems, *Nature*, 421 (2003) 37-42.
- [4] C.D. Thomas, A. Cameron, R.E. Green, M. Bakkenes, L.J. Beaumont, Y.C. Collingham, B.F.N. Erasmus, M.F. de Siqueira, A. Grainger, L. Hannah, L. Hughes, B. Huntley, A.S. van Jaarsveld, G.F. Midgley, L. Miles, M.A. Ortega-Huerta, A. Townsend Peterson, O.L. Phillips, S.E. Williams, Extinction risk from climate change, *Nature*, 427 (2004) 145-148.
- [5] V. Smil, *Energy in world history*, Westview Press, Boulder, 1994.
- [6] R.C.d. Cerqueira Leite, M.R.L. Verde Leal, L.A. Barbosa Cortez, W.M. Griffin, M.I. Gaya Scandiffio, Can Brazil replace 5% of the 2025 gasoline world demand with ethanol?, *Energy*, 34 (2009) 655-661.
- [7] Z. Şen, Solar energy in progress and future research trends, *Prog. Energy Combust. Sci.*, 30 (2004) 367-416.
- [8] G.M. Joselin Herbert, S. Iniyar, E. Sreevalsan, S. Rajapandian, A review of wind energy technologies, *Renew. Sust. Energ. Rev.*, 11 (2007) 1117-1145.
- [9] C. Marcilly, Present status and future trends in catalysis for refining and petrochemicals, *J. Catal.*, 216 (2003) 47-62.
- [10] J.L. Enos, *The rate and direction of inventive activity: economic and social factors*, Princeton University Press, Boston, 1962.
- [11] J.G. Speight, *The chemistry and technology of petroleum*, CRC press, Boca Raton, 2014.
- [12] D.S. Remer, C. Jorgens, Ethylene economics and production forecasting in a changing environment, *Eng. Process. Econ.*, 3 (1978) 267-278.
- [13] M. Bender, An overview of industrial processes for the production of olefins – C4 hydrocarbons, *ChemBioEng Rev.*, 1 (2014) 136-147.
- [14] T. Ren, M. Patel, K. Blok, Olefins from conventional and heavy feedstocks: energy use in steam cracking and alternative processes, *Energy*, 31 (2006) 425-451.
- [15] <http://www.ogj.com/articles/print/volume-111/issue-7/special-report-ethylene-report/global-ethylene-capacity-poised-for-major.html>.



- [16] M.E. Masoumi, S.M. Sadrameli, J. Towfighi, A. Niaei, Simulation, optimization and control of a thermal cracking furnace, *Energy*, 31 (2006) 516-527.
- [17] S. Seifzadeh Haghighi, M.R. Rahimpour, S. Raeissi, O. Dehghani, Investigation of ethylene production in naphtha thermal cracking plant in presence of steam and carbon dioxide, *Chem. Eng. J.*, 228 (2013) 1158-1167.
- [18] M.S. Touvelle, D.P. Klein, T.J. Chen, L.R. Martens, E.S. Ellis, Production of naphtha and light olefins, Patent US 6652737 B2, 2003.
- [19] L.L. Buck, R.D. Key, Ethane, ethylene, methane, cooling, condensation, distillation, heat exchanging, evaporation, Patent US 4895584 A, 1990.
- [20] O. Maass, C.H. Wright, Some physical properties of hydrocarbons containing two and three carbon atoms, *J. Am. Chem. Soc.*, 43 (1921) 1098-1111.
- [21] K. Bauer, D. Garbe, H. Surburg, *Ullmann's Encyclopedia of Industrial Chemistry*, Weinheim, 1988.
- [22] D.W. Tedder, Fractional distillation of C<sub>2</sub> /C<sub>3</sub> hydrocarbons at optimum pressures, Patent US 4430102 A, 1984.
- [23] W.S. Stewart, Control of a fractional distillation column, Patent US 4230534 A, 1980.
- [24] R. Fitzmorris, R. Mah, Improving distillation column design using thermodynamic availability analysis, *AIChE Journal*, 26 (1980) 265-273.
- [25] G.S. Soave, S. Gamba, L.A. Pellegrini, S. Bonomi, Feed-splitting technique in cryogenic distillation, *Ind. Eng. Chem. Res.*, 45 (2006) 5761-5765.
- [26] D. Salerno, H. Arellano-Garcia, G. Wozny, Ethylene separation by feed-splitting from light gases, *Energy*, 36 (2011) 4518-4523.
- [27] P. Bernardo, E. Drioli, G. Golemme, Membrane gas separation: a review/state of the art, *Ind. Eng. Chem. Res.*, 48 (2009) 4638-4663.
- [28] W.J. Koros, Evolving beyond the thermal age of separation processes: membranes can lead the way, *AIChE Journal*, 50 (2004) 2326-2334.
- [29] R.W. Baker, *Membrane technology and applications*, Wiley, West Sussex, 2004.
- [30] <http://www.transparencymarketresearch.com/membrane-separation-market.html>.
- [31] G.J. Van Amerongen, The permeability of different rubbers to gases and its relation to diffusivity and solubility, *J. Appl. Phys.*, 17 (1946) 972-985.
- [32] J.G. Wijmans, R.W. Baker, The solution-diffusion model: a review, *J. Membr. Sci.*, 107 (1995) 1-21.
- [33] M. Mulder, *Basic Principles of Membrane Technology*. Kluwer, Dordrecht, 1991.

- [34] W.J. Koros, G.K. Fleming, Membrane-based gas separation, *J. Membr. Sci.*, 83 (1993) 1-80.
- [35] B. Freeman, Y. Yampolskii, I. Pinnau, *Materials science of membranes for gas and vapor separation*, Wiley, 2006.
- [36] I. Pinnau, W.J. Koros, Relationship between substructure resistance and gas separation properties of defect-free integrally skinned asymmetric membranes, *Ind. Eng. Chem. Res.*, 30 (1991) 1837-1840.
- [37] I.-C. Kim, H.-G. Yoon, K.-H. Lee, Formation of integrally skinned asymmetric polyetherimide nanofiltration membranes by phase inversion process, *J. Appl. Polym. Sci.*, 84 (2002) 1300-1307.
- [38] H. Kawakami, M. Mikawa, S. Nagaoka, Gas permeability and selectivity through asymmetric polyimide membranes, *J. Appl. Polym. Sci.*, 62 (1996) 965-971.
- [39] R.E. Kesting, C.A. Cruse, A.K. Fritzsche, R.F. Malon, M.K. Murphy, A.C. Handermann, Asymmetric gas separation membranes having graded density skins, Patent EP 0257012 A2, 1988.
- [40] R.E. Kesting, The four tiers of structure in integrally skinned phase inversion membranes and their relevance to the various separation regimes, *J. Appl. Polym. Sci.*, 41 (1990) 2739-2752.
- [41] R.E. Kesting, A.K. Fritzsche, M.K. Murphy, A.C. Handermann, C.A. Cruse, R.F. Malon, Process for forming asymmetric gas separation membranes having graded density skins, Patent US 4871494 A, 1989.
- [42] L. Sidney, S. Sourirajan, Sea water demineralization by means of an osmotic membrane, *Advan. Chem. Ser.*, 38 (1962) 117-132.
- [43] F. Xiangli, W. Wei, Y. Chen, W. Jin, N. Xu, Optimization of preparation conditions for polydimethylsiloxane (PDMS)/ceramic composite pervaporation membranes using response surface methodology, *J. Membr. Sci.*, 311 (2008) 23-33.
- [44] T. Kamada, T. Ohara, T. Shintani, T. Tsuru, Optimizing the preparation of multi-layered polyamide membrane via the addition of a co-solvent, *J. Membr. Sci.*, 453 (2014) 489-497.
- [45] K.K. Sirkar, Skin thickness of dense asymmetric or composite membranes for maximum extent of separation of permanent gas mixtures, *Sep. Sci. Technol.*, 13 (1978) 165-171.
- [46] D.R. Paul, Y.P. Yampol'skii, *Polymeric Gas Separation Membranes*, Taylor & Francis, Boca Raton, 1993.
- [47] Y. Huang, T.C. Merkel, R.W. Baker, Pressure ratio and its impact on membrane gas separation processes, *J. Membr. Sci.*, 463 (2014) 33-40.

- [48] N. Peng, N. Widjojo, P. Sukitpaneenit, M.M. Teoh, G.G. Lipscomb, T.-S. Chung, J.-Y. Lai, Evolution of polymeric hollow fibers as sustainable technologies: past, present, and future, *Prog. Polym. Sci.*, 37 (2012) 1401-1424.
- [49] J.G. Crespo, K.W. Böddeker, Membrane processes in separation and purification, Springer, Amsterdam, 2013.
- [50] M. Sandru, T.-J. Kim, W. Capala, M. Huijbers, M.-B. Hägg, Pilot scale testing of polymeric membranes for CO<sub>2</sub> capture from coal fired power plants, *Energy Procedia*, 37 (2013) 6473-6480.
- [51] L. Camacho, L. Dumée, J. Zhang, J.-d. Li, M. Duke, J. Gomez, S. Gray, Advances in membrane distillation for water desalination and purification applications, *Water*, 5 (2013) 94.
- [52] M. Rungta, C. Zhang, W.J. Koros, L. Xu, Membrane-based ethylene/ethane separation: the upper bound and beyond, *AIChE Journal*, 59 (2013) 3475-3489.
- [53] K. Tanaka, A. Taguchi, J. Hao, H. Kita, K. Okamoto, Permeation and separation properties of polyimide membranes to olefins and paraffins, *J. Membr. Sci.*, 121 (1996) 197-207.
- [54] O.M. Ilinitch, G.L. Semin, M.V. Chertova, K.I. Zamaraev, Novel polymeric membranes for separation of hydrocarbons, *J. Membr. Sci.*, 66 (1992) 1-8.
- [55] S.S. Chan, R. Wang, T.-S. Chung, Y. Liu, C<sub>2</sub> and C<sub>3</sub> hydrocarbon separations in poly(1,5-naphthalene-2,2'-bis(3,4-phthalic) hexafluoropropane) diimide (6FDA-1,5-NDA) dense membranes, *J. Membr. Sci.*, 210 (2002) 55-64.
- [56] C. Staudt-Bickel, W.J. Koros, Olefin/paraffin gas separations with 6FDA-based polyimide membranes, *J. Membr. Sci.*, 170 (2000) 205-214.
- [57] R. Faiz, K. Li, Polymeric membranes for light olefin/paraffin separation, *Desalination*, 287 (2012) 82-97.
- [58] J.A. Caballero, I.E. Grossmann, M. Keyvani, E.S. Lenz, Design of hybrid distillation-vapor membrane separation systems, *Ind. Eng. Chem. Res.*, 48 (2009) 9151-9162.
- [59] A. Motelica, O.S.L. Bruinsma, R. Kreiter, M. den Exter, J.F. Vente, Membrane retrofit option for paraffin/olefin separation—a techno-economic evaluation, *Ind. Eng. Chem. Res.*, 51 (2012) 6977-6986.
- [60] J. Ploegmakers, A.R.T. Jelsma, A.G.J. van der Ham, K. Nijmeijer, Economic evaluation of membrane potential for ethylene/ethane separation in a retrofitted hybrid membrane-distillation plant using unisim design, *Ind. Eng. Chem. Res.*, 52 (2013) 6524-6539.
- [61] W. Stephan, R.D. Noble, C.A. Koval, Design methodology for a membrane/distillation column hybrid process, *J. Membr. Sci.*, 99 (1995) 259-272.

- [62] M. Benali, B. Aydin, Ethane/ethylene and propane/propylene separation in hybrid membrane distillation systems: optimization and economic analysis, *Sep. Purif. Technol.*, 73 (2010) 377-390.
- [63] I.K. Kookos, Optimal design of membrane/distillation column hybrid processes, *Ind. Eng. Chem. Res.*, 42 (2003) 1731-1738.
- [64] E. Ayotte-Sauvé, M. Sorin, F. Rheault, Energy requirement of a distillation/membrane parallel hybrid: a thermodynamic approach, *Ind. Eng. Chem. Res.*, 49 (2010) 2295-2305.
- [65] D.W. van Krevelen, K. te Nijenhuis, *Properties of polymers: their correlation with chemical structure; their numerical estimation and prediction from additive group contributions*, Elsevier Science, Amsterdam, 2009.
- [66] R.W. Baker, B.T. Low, Gas separation membrane materials: a perspective, *Macromolecules*, 47 (2014) 6999-7013.
- [67] A. Alshehri, Z. Lai, Attainability and minimum energy of single-stage membrane and membrane/distillation hybrid processes, *J. Membr. Sci.*, 472 (2014) 272-280.
- [68] A.B. Shelekhin, A.G. Dixon, Y.H. Ma, Adsorption, permeation, and diffusion of gases in microporous membranes. II. Permeation of gases in microporous glass membranes, *J. Membr. Sci.*, 75 (1992) 233-244.
- [69] Y.S. Lin, Microporous and dense inorganic membranes: current status and prospective, *Sep. Purif. Technol.*, 25 (2001) 39-55.
- [70] X. Du, E. Wu, Porosity of microporous zeolites A, X and ZSM-5 studied by small angle X-ray scattering and nitrogen adsorption, *J. Phys. Chem. Solids*, 68 (2007) 1692-1699.
- [71] M. Jia, K.-V. Peinemann, R.-D. Behling, Molecular sieving effect of the zeolite-filled silicone rubber membranes in gas permeation, *J. Membr. Sci.*, 57 (1991) 289-292.
- [72] T. Visser, M. Wessling, Auto and mutual plasticization in single and mixed gas C3 transport through Matrimid-based hollow fiber membranes, *J. Membr. Sci.*, 312 (2008) 84-96.
- [73] J. Ploegmakers, S. Japip, K. Nijmeijer, Mixed matrix membranes containing MOFs for ethylene/ethane separation part A: membrane preparation and characterization, *J. Membr. Sci.*, 428 (2013) 445-453.
- [74] C.W. Jones, W.J. Koros, Carbon molecular sieve gas separation membranes- I. Preparation and characterization based on polyimide precursors, *Carbon*, 32 (1994) 1419-1425.
- [75] Y. Dai, J.R. Johnson, O. Karvan, D.S. Sholl, W.J. Koros, Ultem®/ZIF-8 mixed matrix hollow fiber membranes for CO<sub>2</sub>/N<sub>2</sub> separations, *J. Membr. Sci.*, 401-402 (2012) 76-82.

- [76] R. Mahajan, W.J. Koros, Mixed matrix membrane materials with glassy polymers. Part 2, *Polym. Eng. Sci.*, 42 (2002) 1432-1441.
- [77] R. Mahajan, W.J. Koros, Mixed matrix membrane materials with glassy polymers. Part 1, *Polym. Eng. Sci.*, 42 (2002) 1420-1431.
- [78] S.M. Saufi, A.F. Ismail, Fabrication of carbon membranes for gas separation—a review, *Carbon*, 42 (2004) 241-259.
- [79] A.J. Bird, D.L. Trimm, Carbon molecular sieves used in gas separation membranes, *Carbon*, 21 (1983) 177-180.
- [80] T.H. Kim, W.J. Koros, G.R. Husk, K.C. O'Brien, Relationship between gas separation properties and chemical structure in a series of aromatic polyimides, *J. Membr. Sci.*, 37 (1988) 45-62.
- [81] G.J. van Amerongen, Diffusion in elastomers, *Rubber Chem. Technol.*, 37 (1964) 1065-1152.
- [82] A.R. Berens, H.B. Hopfenberg, Diffusion of organic vapors at low concentrations in glassy PVC, polystyrene, and PMMA, *J. Membr. Sci.*, 10 (1982) 283-303.
- [83] L.M. Robeson, Correlation of separation factor versus permeability for polymeric membranes, *J. Membr. Sci.*, 62 (1991) 165-185.
- [84] S.S. Chan, T.-S. Chung, Y. Liu, R. Wang, Gas and hydrocarbon (C<sub>2</sub> and C<sub>3</sub>) transport properties of co-polyimides synthesized from 6FDA and 1,5-NDA (naphthalene)/Durene diamines, *J. Membr. Sci.*, 218 (2003) 235-245.
- [85] M. Rungta, Carbon molecular sieve dense film membranes for ethylene/ethane separations, Ph.D. dissertation, Georgia Institute of Technology, 2012.
- [86] C. Ma, W.J. Koros, Effects of hydrocarbon and water impurities on CO<sub>2</sub>/CH<sub>4</sub> separation performance of ester-crosslinked hollow fiber membranes, *J. Membr. Sci.*, 451 (2014) 1-9.
- [87] P.M. Budd, B.S. Ghanem, S. Makhseed, N.B. McKeown, K.J. Msayib, C.E. Tattershall, Polymers of intrinsic microporosity (PIMs): robust, solution-processable, organic nanoporous materials, *Chem. Commun.*, (2004) 230-231.
- [88] P.M. Budd, K.J. Msayib, C.E. Tattershall, B.S. Ghanem, K.J. Reynolds, N.B. McKeown, D. Fritsch, Gas separation membranes from polymers of intrinsic microporosity, *J. Membr. Sci.*, 251 (2005) 263-269.
- [89] N.B. McKeown, P.M. Budd, K.J. Msayib, B.S. Ghanem, H.J. Kingston, C.E. Tattershall, S. Makhseed, K.J. Reynolds, D. Fritsch, Polymers of intrinsic microporosity (PIMs): bridging the void between microporous and polymeric materials, *Chem. Eur. J.*, 11 (2005) 2610-2620.

- [90] P.M. Budd, N.B. McKeown, D. Fritsch, Polymers of intrinsic microporosity (PIMs): high free volume polymers for membrane applications, *Macromol. Symp.*, 245-246 (2006) 403-405.
- [91] B.S. Ghanem, N.B. McKeown, P.M. Budd, N.M. Al-Harbi, D. Fritsch, K. Heinrich, L. Starannikova, A. Tokarev, Y. Yampolskii, Synthesis, characterization, and gas permeation properties of a novel group of polymers with intrinsic microporosity: PIM-polyimides, *Macromolecules*, 42 (2009) 7881-7888.
- [92] B.S. Ghanem, N.B. McKeown, P.M. Budd, J.D. Selbie, D. Fritsch, High-Performance Membranes from Polyimides with Intrinsic Microporosity, *Adv. Mater.*, 20 (2008) 2766-2771.
- [93] M. Carta, R. Malpass-Evans, M. Croad, Y. Rogan, J.C. Jansen, P. Bernardo, F. Bazzarelli, N.B. McKeown, An efficient polymer molecular sieve for membrane gas separations, *Science*, 339 (2013) 303-307.
- [94] M. Carta, M. Croad, R. Malpass-Evans, J.C. Jansen, P. Bernardo, G. Clarizia, K. Friess, M. Lanč, N.B. McKeown, Triptycene induced enhancement of membrane gas selectivity for microporous Tröger's base polymers, *Adv. Mater.*, 26 (2014) 3526-3531.
- [95] B.S. Ghanem, R. Swaidan, E. Litwiller, I. Pinnau, Ultra-microporous triptycene-based polyimide membranes for high-performance gas separation, *Adv. Mater.*, 26 (2014) 3688-3692.
- [96] R. Swaidan, B. Ghanem, I. Pinnau, Fine-tuned intrinsically ultramicroporous polymers redefine the permeability/selectivity upper bounds of membrane-based air and hydrogen separations, *ACS Macro Lett.*, 4 (2015) 947-951.
- [97] P. Li, T.S. Chung, D.R. Paul, Gas sorption and permeation in PIM-1, *J. Membr. Sci.*, 432 (2013) 50-57.
- [98] R.J. Swaidan, B. Ghanem, R. Swaidan, E. Litwiller, I. Pinnau, Pure- and mixed-gas propylene/propane permeation properties of spiro- and triptycene-based microporous polyimides, *J. Membr. Sci.*, 492 (2015) 116-122.
- [99] X. Ma, O. Salinas, E. Litwiller, I. Pinnau, Novel spirobifluorene- and dibromospirobifluorene-based polyimides of intrinsic microporosity for gas separation applications, *Macromolecules*, 46 (2013) 9618-9624.
- [100] R. Swaidan, B.S. Ghanem, E. Litwiller, I. Pinnau, Pure- and mixed-gas CO<sub>2</sub>/CH<sub>4</sub> separation properties of PIM-1 and an amidoxime-functionalized PIM-1, *J. Membr. Sci.*, 457 (2014) 95-102.
- [101] N. Du, G.P. Robertson, J. Song, I. Pinnau, M.D. Guiver, High-performance carboxylated polymers of intrinsic microporosity (PIMs) with tunable gas transport properties, *Macromolecules*, 42 (2009) 6038-6043.

- [102] N. Du, H.B. Park, G.P. Robertson, M.M. Dal-Cin, T. Visser, L. Scoles, M.D. Guiver, Polymer nanosieve membranes for CO<sub>2</sub>-capture applications, *Nat. Mater.*, 10 (2011) 372-375.
- [103] J. Weber, N. Du, M.D. Guiver, Influence of intermolecular interactions on the observable porosity in intrinsically microporous polymers, *Macromolecules*, 44 (2011) 1763-1767.
- [104] T. Sandreczki, X. Hong, Y. Jean, Sub-glass-transition-temperature annealing of polycarbonate studied by positron annihilation spectroscopy, *Macromolecules*, 29 (1996) 4015-4018.
- [105] R. Swaidan, B. Ghanem, E. Litwiller, I. Pinnau, Effects of hydroxyl-functionalization and sub-T<sub>g</sub> thermal annealing on high pressure pure- and mixed-gas CO<sub>2</sub>/CH<sub>4</sub> separation by polyimide membranes based on 6FDA and triptycene-containing dianhydrides, *J. Membr. Sci.*, 475 (2015) 571-581.
- [106] F.Y. Li, Y. Xiao, T.-S. Chung, S. Kawi, High-performance thermally self-cross-linked polymer of intrinsic microporosity (PIM-1) membranes for energy development, *Macromolecules*, 45 (2012) 1427-1437.
- [107] S. Li, H.J. Jo, S.H. Han, C.H. Park, S. Kim, P.M. Budd, Y.M. Lee, Mechanically robust thermally rearranged (TR) polymer membranes with spirobisindane for gas separation, *J. Membr. Sci.*, 434 (2013) 137-147.
- [108] H.B. Park, S.H. Han, C.H. Jung, Y.M. Lee, A.J. Hill, Thermally rearranged (TR) polymer membranes for CO<sub>2</sub> separation, *J. Membr. Sci.*, 359 (2010) 11-24.
- [109] H. Shamsipur, B.A. Dawood, P.M. Budd, P. Bernardo, G. Clarizia, J.C. Jansen, Thermally rearrangeable PIM-polyimides for gas separation membranes, *Macromolecules*, 47 (2014) 5595-5606.
- [110] D.F. Sanders, R. Guo, Z.P. Smith, K.A. Stevens, Q. Liu, J.E. McGrath, D.R. Paul, B.D. Freeman, Influence of polyimide precursor synthesis route and ortho-position functional group on thermally rearranged (TR) polymer properties: pure gas permeability and selectivity, *J. Membr. Sci.*, 463 (2014) 73-81.
- [111] H.B. Park, C.H. Jung, Y.M. Lee, A.J. Hill, S.J. Pas, S.T. Mudie, E. Van Wagner, B.D. Freeman, D.J. Cookson, Polymers with cavities tuned for fast selective transport of small molecules and ions, *Science*, 318 (2007) 254-258.
- [112] K.-S. Chang, Z.-C. Wu, S. Kim, K.-L. Tung, Y.M. Lee, Y.-F. Lin, J.-Y. Lai, Molecular modeling of poly(benzoxazole-co-imide) membranes: a structure characterization and performance investigation, *J. Membr. Sci.*, 454 (2014) 1-11.
- [113] B. Comesaña-Gándara, A. Hernández, J.G. de la Campa, J. de Abajo, A.E. Lozano, Y.M. Lee, Thermally rearranged polybenzoxazoles and poly(benzoxazole-co-imide)s from ortho-hydroxyamine monomers for high performance gas separation membranes, *J. Membr. Sci.*, 493 (2015) 329-339.

- [114] M. Calle, Y. Chan, H.J. Jo, Y.M. Lee, The relationship between the chemical structure and thermal conversion temperatures of thermally rearranged (TR) polymers, *Polymer*, 53 (2012) 2783-2791.
- [115] X. Ma, R. Swaidan, B. Teng, H. Tan, O. Salinas, E. Litwiller, Y. Han, I. Pinnau, Carbon molecular sieve gas separation membranes based on an intrinsically microporous polyimide precursor, *Carbon*, 62 (2013) 88-96.
- [116] K.M. Steel, W.J. Koros, Investigation of porosity of carbon materials and related effects on gas separation properties, *Carbon*, 41 (2003) 253-266.
- [117] J.-i. Hayashi, H. Mizuta, M. Yamamoto, K. Kusakabe, S. Morooka, S.-H. Suh, Separation of ethane/ethylene and propane/propylene systems with a carbonized BPDA–pp'ODA polyimide membrane, *Ind. Eng. Chem. Res.*, 35 (1996) 4176-4181.
- [118] K.-i. Okamoto, S. Kawamura, M. Yoshino, H. Kita, Y. Hirayama, N. Tanihara, Y. Kusuki, Olefin/paraffin separation through carbonized membranes derived from an asymmetric polyimide hollow fiber membrane, *Ind. Eng. Chem. Res.*, 38 (1999) 4424-4432.
- [119] H. Suda, K. Haraya, Alkene/alkane permselectivities of a carbon molecular sieve membrane, *Chem. Commun.*, (1997) 93-94.
- [120] M. Yamamoto, K. Kusakabe, J.-i. Hayashi, S. Morooka, Carbon molecular sieve membrane formed by oxidative carbonization of a copolyimide film coated on a porous support tube, *J. Membr. Sci.*, 133 (1997) 195-205.
- [121] M. Rungta, L. Xu, W.J. Koros, Carbon molecular sieve dense film membranes derived from Matrimid® for ethylene/ethane separation, *Carbon*, 50 (2012) 1488-1502.
- [122] L. Xu, M. Rungta, W.J. Koros, Matrimid® derived carbon molecular sieve hollow fiber membranes for ethylene/ethane separation, *J. Membr. Sci.*, 380 (2011) 138-147.
- [123] A.B. Fuertes, I. Menendez, Separation of hydrocarbon gas mixtures using phenolic resin-based carbon membranes, *Sep. Purif. Technol.*, 28 (2002) 29-41.
- [124] [http://www.che.udel.edu/research\\_groups/nanomodeling/research.html](http://www.che.udel.edu/research_groups/nanomodeling/research.html).



## Chapter 2

### Theoretical Background

This chapter describes the gas transport mechanisms and equations through microporous polymers and carbons. In addition, various characterization techniques that are used to elucidate the membrane microstructure are introduced. In the last section, several detrimental effects that could affect the membrane performance when separating gas mixtures under realistic conditions are described.

#### *2.1 Gas transport through microporous solids*

##### *2.1.1 Transport regime according to pore size*

The transport of molecules through a microporous solid is a function of the porosity, size and morphology of its pores [1]. The gas transport mechanisms according to the pore size of the membranes are shown schematically in **Fig. 2.1**. Hagen-Poiseuille flow takes place in cavities that are much larger compared to the natural diffusion paths of gaseous molecules; therefore, this mechanism is not useful for gas separation. As the cavities become smaller, Knudsen diffusion becomes relevant when the mean free path of the molecules and the diameter of the holes are of comparable size. According to the Knudsen theory [2], the molecules of a permeant gas bounce more often with the pore wall rather than with other molecules. The gas selectivity under Knudsen flow is equal to the square root of the inverse ratio of the molecular weights of the permeant species. Historically, Knudsen-controlled porous metal membranes were first industrially

employed to enrich uranium from its isotopes [3]. The solution-diffusion mechanism occurs when the permeant molecules advance at a different rate through interstitial zones developed in a tight membrane matrix [4]. There is a particular case of gas transport in which one of the permeant species interacts heavily with the pore walls while hindering the permeation of other species via blocking. This pore-blocking effect is triggered by the co-permeation of gases with very different condensabilities (e.g.  $C_4H_{10}/CH_4$  separation [5]). Finally, there are ultra-microporosities, smaller than the permeants themselves, that prevent the admission of the larger components into their inner structure [6].

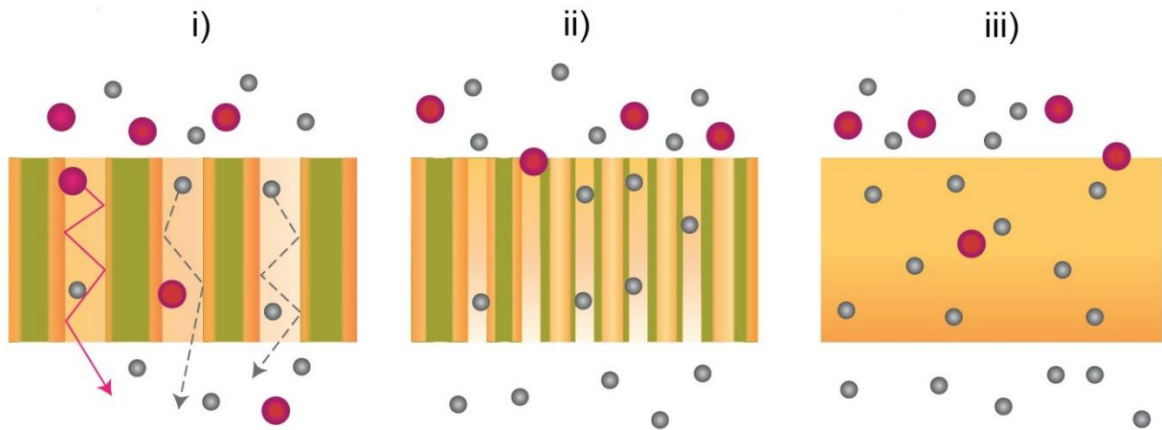


**Fig. 2.1.** Relevant transport mechanisms for gas separation. (i) Knudsen flow, (ii) molecular sieving, and (iii) solution-diffusion mechanism. Adapted from [7].

### 2.1.2 Solution-diffusion model and the mass balance of an isotropic film

According to the solution-diffusion model [4, 8], transport of gaseous molecules through a film follows this sequence:

- Sorption on the upstream membrane surface
- Diffusion of molecules down a concentration gradient
- Desorption on the downstream side of the membrane

The one-dimensional Fick's First Law represents the activated diffusion of molecules that occurs due to a concentration gradient:

$$J_i = -D_i \frac{dC_i}{dx}$$

Where  $J_i$  is the flux,  $D_i$  is the diffusion coefficient of  $i$  in the film, and  $dC_i$  is the local change in concentration over a  $dx$  distance differential.

The mass balance through a rectangular film of thickness  $l$  where diffusion takes place in only one direction is represented as Fick's second law:

$$\frac{\partial C_i}{\partial t} = D_i \frac{\partial^2 C_i}{\partial x^2}$$

Where  $t$  is the time.

Assuming steady state:

$$\frac{d^2 C_i}{dx^2} = 0$$

and after integration in terms of  $x$ :

$$C_i = ax + b$$

Which indicates that during the steady state transport of molecules through a film there is a linear profile of concentration, as shown in **Fig. 2.2**.

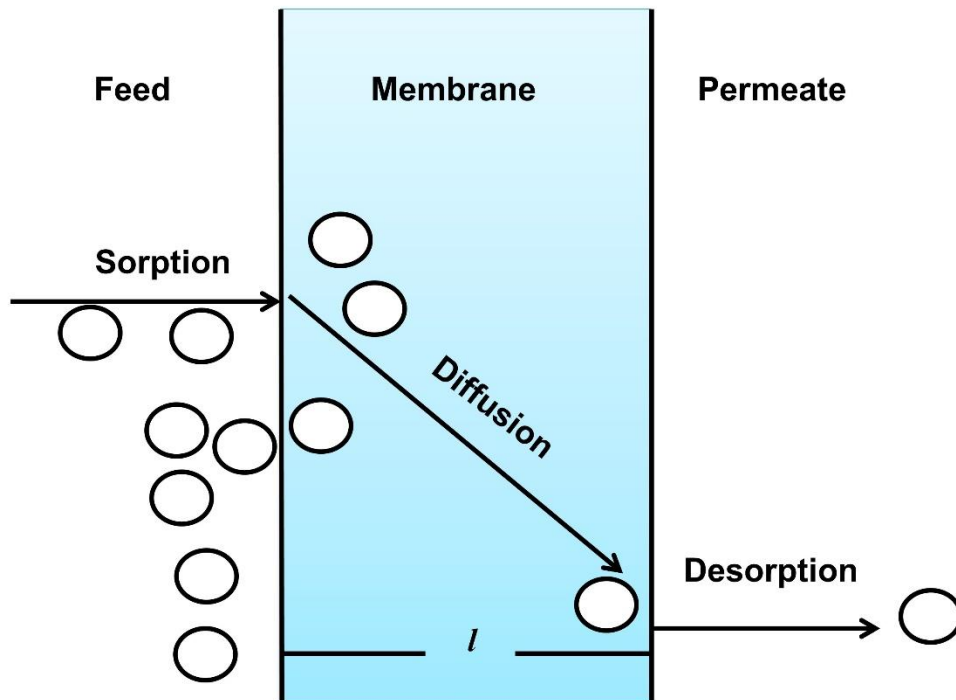


**Fig. 2.2.** Gas diffusion in one dimension through a film of thickness  $l$  [4].

For an isotropic film,  $D_i$  is assumed a constant value, as long as the molecules do not interact with the membrane or with themselves.

If  $D_i$  is a constant, Fick's first law can be integrated with the limits  $x = 0, C_i = C_f$  and  $x = l, C_i = C_p$ , viz.

$$J_i = D_i \frac{(C_f - C_p)}{l}$$

Where  $l$  is the thickness of the membrane,  $C_f$  represents the concentration of permeating component  $i$  at the feed side and  $C_p$  is the concentration of  $i$  at the permeate side. For ideal systems, Henry's law can be used to describe the gas solubility in the membrane as:

$$c_i = S_i p_i$$

Where  $S_i$  is the solubility coefficient of  $i$  in the membrane and  $p_i$  is the partial pressure of  $i$ .

Finally, the flux  $J_i$  can be estimated as a function of the permeability coefficient  $P_i$  and the difference in partial pressure of  $i$  upstream and downstream of the membrane such as

$$J_i = \frac{P_i(\Delta p_i)}{l}$$

where the permeability can further be expressed as the product of the diffusivity and solubility coefficients

$$P_i = D_i S_i$$

In addition, the pure gas membrane selectivity is the product of their respective diffusivity and solubility ratios:

$$\alpha_{i/j} = \frac{D_i S_i}{D_j S_j} = \alpha_D \alpha_S$$

The  $\alpha_D$  represents a kinetic factor describing how fast molecules of different sizes diffuse through the membrane matrix, whereas  $\alpha_S$  is a thermodynamic factor that relates the relative affinity of two gas species with the membrane material.

### 2.1.3 Transport properties of organic polymers

#### 2.1.3.1 The glass transition and its influence on transport properties

Viscoelastic polymeric systems are classified as glasses or rubbers at room temperature according to their glass transition ( $T_g$ ) that can be related to a decrease of the long-range movement of the chains [9]. The  $T_g$  of a polymer is a second-order thermodynamic transition in which there is a discontinuity on derived properties (e.g. heat-capacity, volumetric expansion). A glassy polymer is “frozen”, whereas polymers that are heated above their glass transition are classified as rubbers. Furthermore, rubbers are equilibrium materials. Therefore, their dynamic free volume is constant. When a perturbation is applied to a rubbery system, the chains realign and deform the polymer matrix. For this reason, rubbers may suffer compaction [10]. Glassy polymers, on the other hand, have a significant portion of empty space that is static compared to the time frames of molecular diffusion (**Fig. 2.3**). Accordingly, several group contribution methods have been developed to calculate the fractional free volume (*FFV*) of an organic polymer [11, 12], viz.

$$FFV = \frac{V - V_0}{V_0}$$

Where  $V$  is the observed specific volume and  $V_0$  is calculated from the correlation:

$$V_0 = 1.3V_w$$

Where  $V_w$  represents the Van der Waals volume which is estimated from the Bondi’s group contribution method [13]. The free volume is deemed essential for the gas transport in polymeric systems because it provides sorption sites that enhance solubility and thus permeability [14, 15]. In addition, glasses have rigid structures that sieve permeants in

terms of their molecular dimension more efficiently than their rubbery counterparts [16]. Accordingly, most commercial gas separation processes where the molecular size is the critical parameter use glassy polymers [17].

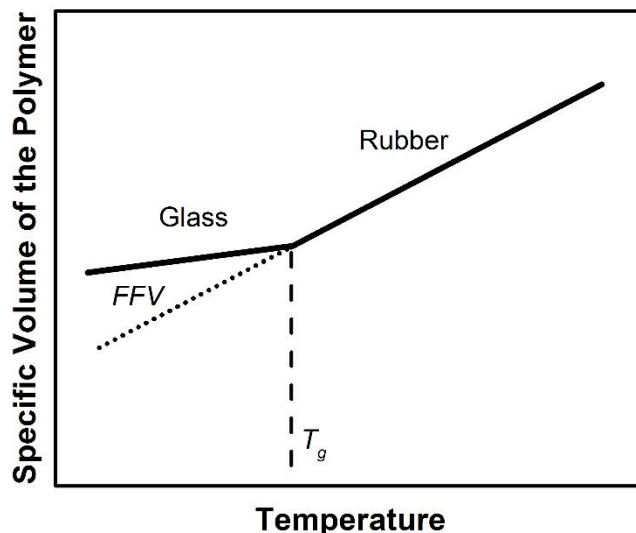


**Fig. 2.3.** The change in the specific volume of a polymer with varying temperature. The fractional free volume may be observed in polymers cooled below their glass transition temperature.

### 2.1.3.2 Chemical structure and free volume of polymers

The first gas separation studies in polycarbonates [18], polysulfones [19], and polyimides [20] elucidated the importance of the polymeric structure on its correspondent free volume [21-23]. For example, rigid polymer backbones, made stiffer via functionalization, may entrap a higher fraction of inter-chain free volume compared to their unfunctionalized analogs [24]. Depending on their shape and conformation, side groups

can either act as chain spacers (if they are short and rigid) or fill the free volume (if they are long, flexible, and can occupy space) [25, 26]. Naturally, the gas transport through a polymer may be designed by modifying the chain rigidity and conformation of the polymer in its solid state when cast into films [27]. The most permeable polymer known today, glassy PTMSP, has a backbone made of double bonds that prevent major segmental motions [28]. In addition, its bulky trimethylsilyl propyl groups keep the structure remarkably open. Accordingly, the permeability of various permanent gases, such as O<sub>2</sub>, has been reported to exceed 4000 Barrer [29]. Conversely, a polymer may reach an extreme case of regular chain-packing evidenced by the formation of crystalline domains that hinder gas transport [30]. For example, poly(4-methyl-1-pentene), with a crystalline fraction of 76%, had a N<sub>2</sub> permeability of 5.93 Barrer whereas its counterpart, with only 51% crystallinity, had a N<sub>2</sub> permeability of 9.3 Barrer [31].

#### 2.1.3.3 Structural analysis of intrinsically microporous polymers

Intrinsically microporous polymers have *interconnected* free volume elements by virtue of their mobility-restricted structures [32], shown in **Fig. 2.4**. The PIM family owes their microporosity to very rigid contortion centers, which prevent efficient chain packing [33]. Ideally, PIMs should have bottlenecked pores that achieve significant diffusion selectivity via molecular sieving coupled with very high permeabilities [34]. The innovation of PIM-polyimides (i.e. polyimides bearing contortion centers) allowed for a great versatility of synthesis [35]. **Fig. 2.5** shows the evolution of the PIM chemical structures as they turned into more rigid contortion centers.



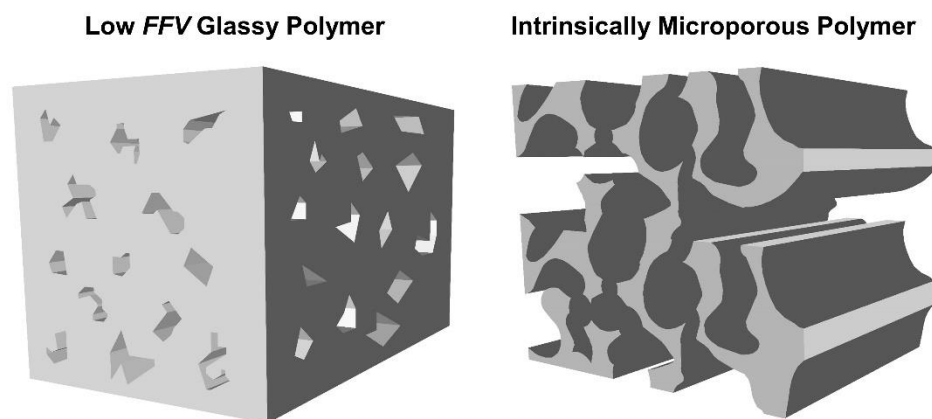


**Fig. 2.4.** Schematic representation of non-connected (left) and interconnected (right) *FFV* as a consequence of inefficient chain packing.

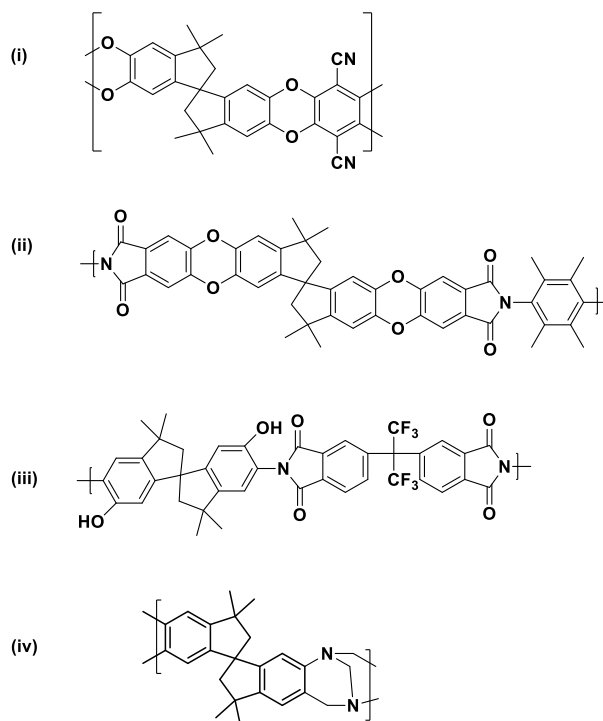


**Fig. 2.5.** Evolution of PIM materials: (i) original ladder spiro-contorted PIM-1 [33], (ii) PIM-polyimide with contortion centers [35], (iii) OH-functionalization of PIM-polyimide [36], and (iv) ladder polymer with more rigid spiro/Tröger's base contortion centers [37].

#### 2.1.3.4 Molecular diffusion in polymeric mediums

Gaseous molecules have energy levels of the order of  $\sim 3k_B T$  due to their movement [38]. In polymer systems, as shown in **Fig. 2.6**, a penetrant molecule diffuses between the inter-chain spaces in a polymeric medium. A statistical gap driven by chain motion opens up and allows passage of the gas permeant [39]. Activated diffusion of gases occurs, and the average position of the molecule in the system changes [40].

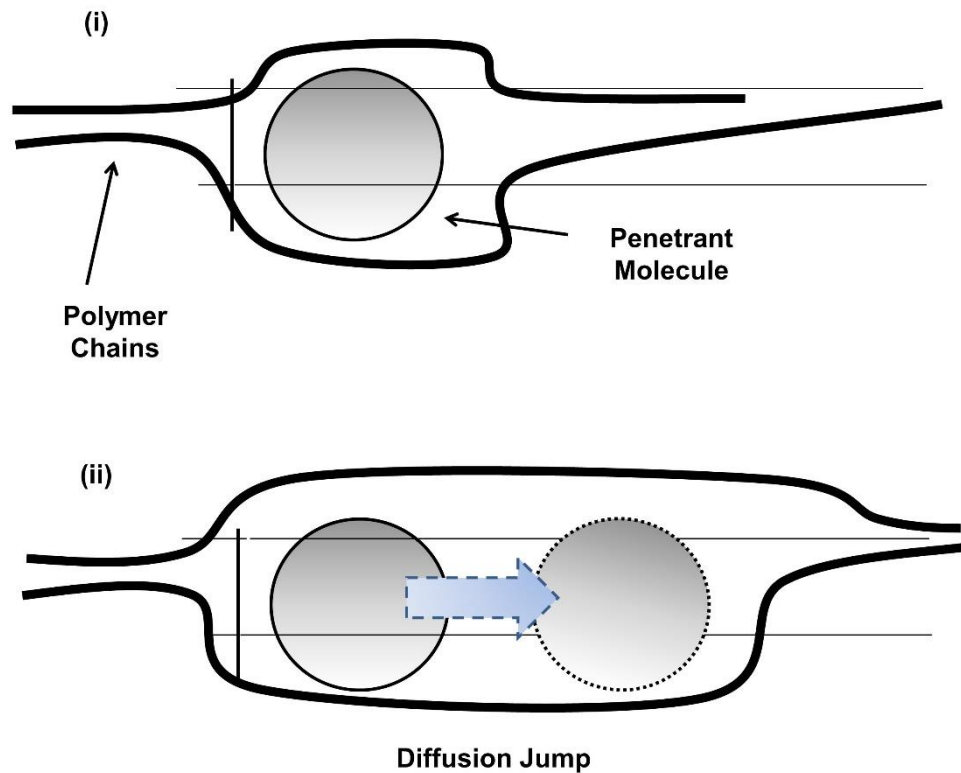


**Fig. 2.6.** Transport of small penetrant molecules in the vicinity of two polymeric chains: (i) chains surround the penetrant molecule and (ii) statistical gap opens to allow the diffusion jump of the molecule.

### 2.1.3.5 Sorption in polymeric mediums

The sorption of gas in a polymer is typically an exothermic process that is driven by two separate contributions: (i) the gas enthalpy change according to its phase change and the (ii) interactions between the penetrant and the chains [41].

Gas dissolves in dense, rubbery polymers according to Henry's law [42]:

$$C_i = K_D p_i$$

Where  $K_D$  is the Henry's constant and  $p_i$  is the pressure and  $C_i$  is the equilibrium concentration at that pressure.

Glassy polymers, on the other hand, follow a dual mode sorption which in addition to the Henry sorption model, also presents Langmuir sorption sites [43]. Thus, the sorption in glassy polymers is simply:

$$C_i = K_D p_i + \frac{C'_H b p_i}{1 + b p_i}$$

Where  $C'_H$  is the Langmuir sites capacity, and  $b$  is the interaction parameter [44]. **Fig. 2.7** shows the shape of the sorption modes previously described. Henry's sorption model is linear with respect to pressure increases whereas the Langmuir isotherm is concave to the pressure axis. The dual mode is simply the addition of both contributions. At low pressures, the Langmuir sites are saturated with the sorbent. At high pressures, the concentration rises steadily due to the Henry contribution.

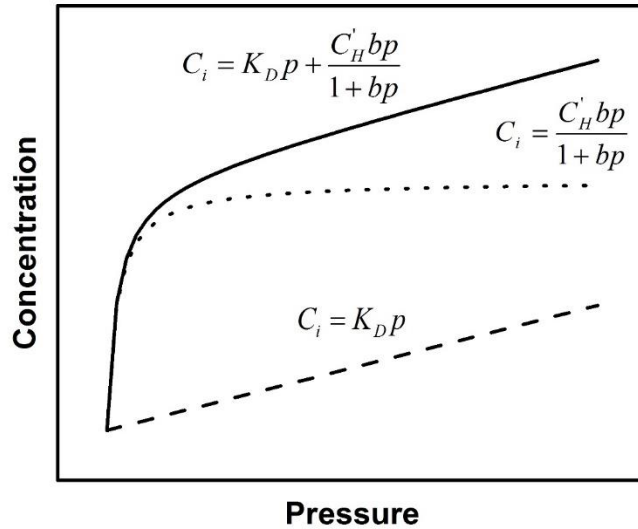


**Fig. 2.7.** Gas uptake in the Henry's and Langmuir sorption modes.

*2.1.4 The polymer upper bound: empirical and theoretical considerations*

In 1991, Robeson analyzed a large permeability and selectivity data base to define the existing polymer upper bound for several systems, such as O<sub>2</sub>/N<sub>2</sub>, CO<sub>2</sub>/CH<sub>4</sub>, and N<sub>2</sub>/CH<sub>4</sub> [45]. This upper limit performance of polymeric systems identified a trade-off relationship between selectivity and permeability. Subsequently, Freeman indicated that the polymers that could surpass the upper bound require very rigid chains and high free volume [46]. The upper bound limit of gas separation performance using polymers was represented as a function of permeability  $P_i$  as:

$$\alpha_{i/j} = \beta_{i/j} P_i^{-\lambda_{i/j}}$$

Where  $\lambda_{ij}$  is a parameter that depends only on the difference in molecular dimension between the permeant species, and  $\beta_{ij}$  is a factor that depends on  $\lambda_{ij}$ , the condensability of the permeant gases, and one empiric factor.

Rungta and Koros predicted the theoretical polymer upper bound for ethylene/ethane separation [47]. The following parameters were obtained:

$$\alpha_{C_2H_4/C_2H_6} = 7.3P_{C_2H_4}^{-0.14}$$

This equation represents the limit ethylene/ethane separation performance provided by several rigid polyimides, whose structures are shown in **Fig. 2.8**. These polymers share in common their chemistry and several physical properties, such as high  $T_g$  and rigid structure.

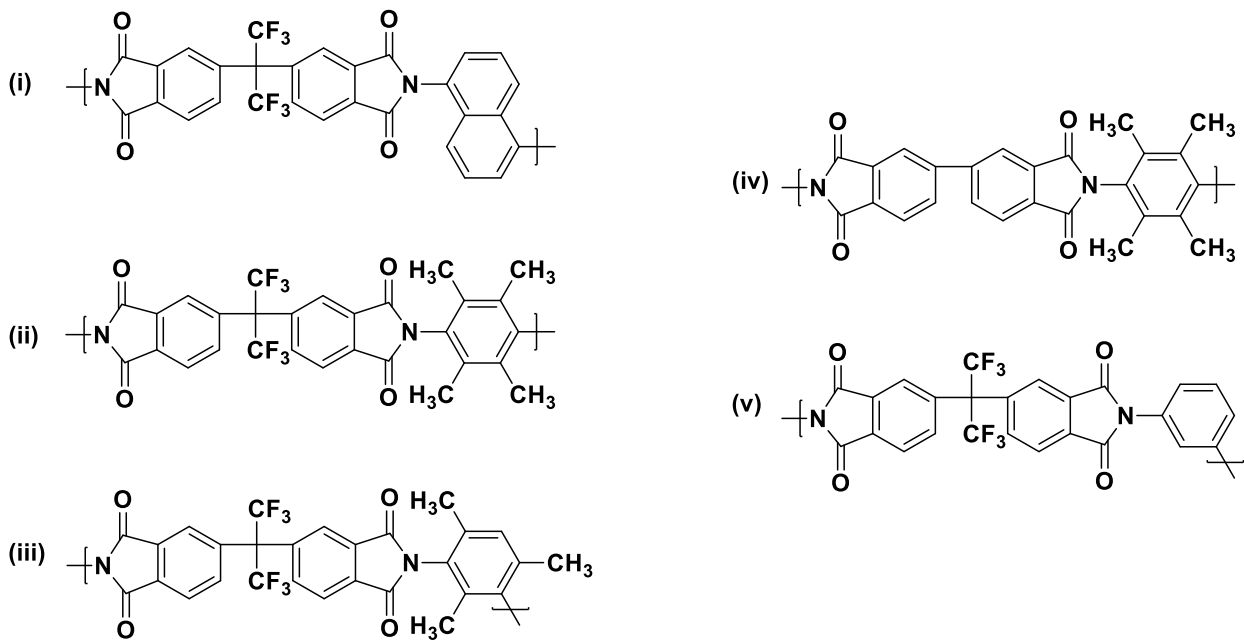


**Fig. 2.8.** Chemical structure of representative polyimides that were used to construct the ethylene/ethane upper bound: (i) 6FDA-NDA [48], (ii) 6FDA-Durene [49], (iii) 6FDA-TrMPD [49], (iv) BPDA-TeMPD [49], (v) 6FDA-mPD [50].

### 2.1.5 Transport in carbon molecular sieves (CMS)

#### 2.1.5.1 Carbon structure

Amorphous carbons generated through pyrolysis of polymeric substrates present narrower pore size distributions than their polymeric analogs [51] [52] [53] [54]. These carbon membranes comprise a matrix of disordered graphene layers as schematically presented in **Fig. 2.9**. Their gas transport properties significantly surpassed those of conventional polymeric systems [53, 55-57]. For example, Matrimid® carbonized at 800 °C showed CO<sub>2</sub>/CH<sub>4</sub> selectivity of ~200 paired with a CO<sub>2</sub> permeability of 100 Barrer [58];

thus, the CMS performance was 6 times more selective and 10 times more permeable than the pristine polymer tested under the same conditions. The unaligned sheets of  $sp^2$ -bonded honeycomb graphene provide exceptional diffusion selectivities and consequently very high permselectivities [59-62].

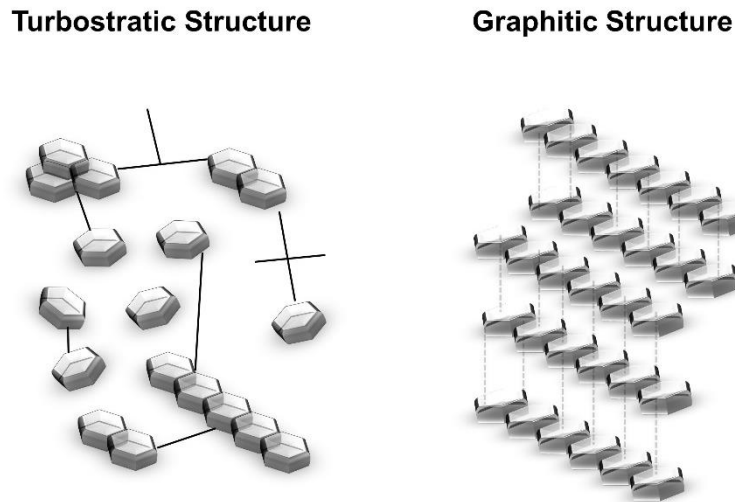


**Fig. 2.9.** The schematic structures of disordered carbon and regular graphite structure [63].

According to the studies by Koros and Steel [58] (**Fig. 2.10**), a CMS structure mainly achieves separation by molecular sieving. The size-sieving pores were ideally represented as large voids that allow fast diffusion connected by tight constrictions of size  $d_c$ , which is comparable in size to the permeant molecules.

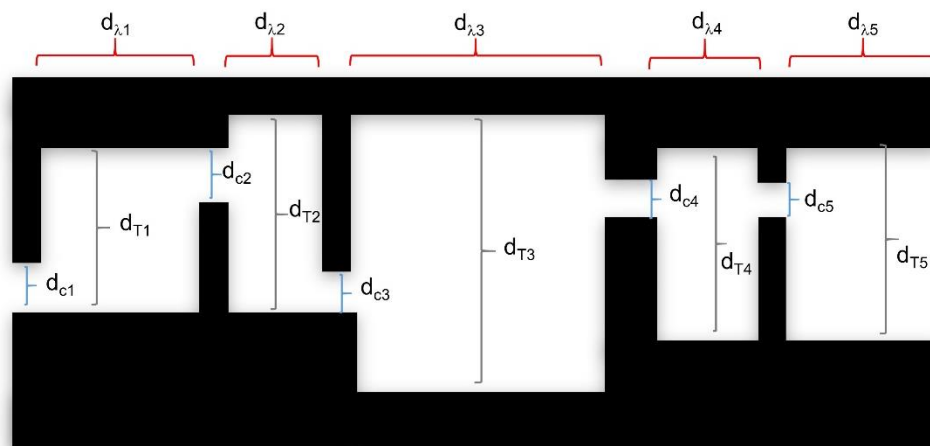


**Fig. 2.10.** Critical dimensions of an idealized carbon pore. The critical dimensions,  $d_c$ , are the ultra-microporous entrances that lead to the sorption chambers of dimensions  $d_T$ . Finally,  $d_\lambda$  is related to the fast diffusion jumps in the cavities of the chamber [58].

#### 2.1.5.2 Pyrolysis protocol and its effect on the carbon cavities

Carbons are greatly influenced by the thermal protocol by which they were generated [64]. Higher temperatures accelerate the degradation kinetics of the polymeric substrate; thus, a higher percentage of elemental carbon is embedded into the carbonaceous remains generated at higher temperatures [65]. Typically, carbons fabricated at 800 °C present an amorphous matrix that contains ~90% elemental carbon [66]. Furthermore, the effect of the duration of the heating protocol on the gas transport properties of the resulting CMS concluded that longer thermal soaks promote a pore-sintering effect [67]. For example, Steel reported that the CO<sub>2</sub> permeability decreased by ~30-fold, from 100 Barrer to 3 Barrer, by increasing the thermal soak time from 2 hours to 8 hours at 800 °C [64]. The temperature ramping rate has also been found to influence the speed at which the



cavities of the carbon pores sinter. Faster ramping rates accelerate the degradation of the carbon matrix and its sintering into tighter sieves [68]. Finally, the atmospheric composition during the pyrolysis is instrumental to the CMS-pore tailoring [69]. Kiyono proposed that O<sub>2</sub> was responsible for narrowing the carbonaceous pores through selective chemisorption during the pyrolysis process [70]. **Fig. 2.11** illustrates the observed effects of the pyrolysis protocol on the ultramicroporosity of a CMS.

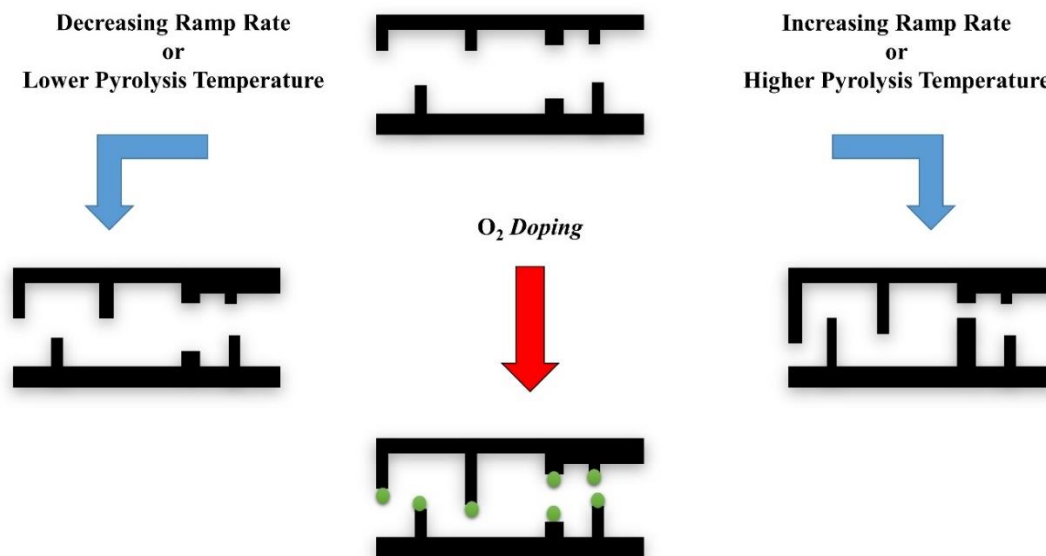


**Fig. 2.11.** Pyrolysis protocol effect on carbon ultramicroporous cavities [58, 68, 69].

### 2.1.5.3 Diffusion in carbon molecular sieves

Gaseous molecules diffusing through carbon molecular sieves follow the solution-diffusion mechanism as previously described for their polymeric counterparts [71]. Unlike most of their polymer analogs, carbons have very rigid structures. Therefore, the molecular

sieving mechanisms dominate the diffusion selectivity by reducing the entropic freedom of the molecules traversing their narrow-sized cavities [59].

#### 2.1.5.4 Sorption in carbonaceous materials

Sorption of gases in a CMS follows the Langmuir equation as [72]:

$$C_i = \frac{C'_H b p_i}{1 + b p_i}$$

Where  $C'_H$  represents the Langmuir hole capacity,  $b$  is the interaction parameter, and  $p_i$  is the partial pressure of the adsorbent.

## 2.2 Material characterization techniques

### 2.2.1 Gel permeation chromatography of polymeric materials

Polymeric materials are represented as mixtures of periodic chains characterized by several molecular weight average numbers [73]. They are calculated as:

$$M_n = \frac{\sum_i N_i M_i}{\sum_i N_i}$$

$$M_w = \frac{\sum_i N_i M_i^2}{\sum_i N_i M_i}$$

Where  $M_n$  is the number average molecular weight,  $M_w$  is the weight average molecular weight, and  $N_i$  is the number of molecules of molecular weight  $M_i$ . Finally, the polydispersity index (*PDI*) is computed as:

$$PDI = \frac{M_w}{M_n}$$

The physical properties of the polymer will vary depending on its molecular weight averages and PDI. For instance, the  $T_g$  of poly(ethylene terephthalate) changed from 56 to 66 °C as its  $M_n$  increased from 5000 to 40000 g mol<sup>-1</sup> [74]. Fundamentally, a membrane made of a polymeric material needs to be mechanical resistance to withstand the mechanical pressure. Therefore, a high molecular weight is typically required for film fabrication.

### 2.2.2 *Thermal stability of polymeric materials*

Polymers may have thermal transitions if heated at a particular temperature under the right atmospheric conditions [75, 76]. A thermal gravimetric analysis (TGA) is needed to ascertain such transitions. Furthermore, polymeric films, and especially those cast from microporous materials, may entrap significant amounts of solvent that need to be removed before the measurement of its transport properties [77]. Conversely, certain heat treatments may be desired and need to be planned extensively before burning expensive or scarce new polymer [78, 79].

### *2.2.3 Functional groups and microstructure determination*

The functional groups of a polymer modify its solid-state conformation and overall transport properties [80]. Accordingly, techniques such as nuclear magnetic resonance (NMR) and Fourier-transform infrared (FTIR) spectroscopy may quantify the individual moieties found in a polymeric matrix. NMR reports the electromagnetic interaction of the nuclei of the polymer atoms compared to a reference [81]. Similarly, a sample bombarded with infrared energies absorbs and reemits some of it, which provide information on the bonds found in the macromolecules. Raman spectroscopy depicts information on the membrane microstructure; such as the existence of graphitic domains [82].

### *2.2.4 Surface area and pore size distribution (PSD) estimation*

The pores relevant for gas separation applications are smaller than 2 nm width. Therefore, the evaluation of its size and distribution is instrumental to the prediction of the membrane separation performance. This task is not an easy challenge since the micropores cannot be surveyed by traditional microscopy techniques (e.g. SEM). Conversely, advanced qualitative methods have been developed to provide meaningful insight in that narrow region of 0.2-2 nm.

#### *2.2.4.1 X-Ray Diffraction*

X-Ray diffraction (XRD) is an analytical technique traditionally used for crystallography studies on ordered materials [83]. Furthermore, this method has also been

applied to amorphous and semicrystalline polymeric samples [84, 85]. Fundamentally, a solid sample interacts with the X-rays to generate a diffraction pattern that is unique to the sample. Bragg's law describes the diffraction phenomenon:

$$2d \sin \theta = n\lambda$$

Where  $d$  is the average distance between diffraction planes,  $\theta$  is the scattering angle,  $\lambda$  is the wavelength of the incident wave, and  $n$  is a positive integer.

The scattered rays intensity is measured with a detector by varying the incident angle at which the rays enter the system. Regular structures such as zeolites and carbons have very sharp intensity spectra [86], which can be correlated to their narrow pore distributions whereas polymers tend to show very broad spectra [85, 87]. However, isomeric polyimides where only a small portion of their dianhydride moiety was changed depicted significant changes in their d-spacing values [22]. Furthermore, sub- $T_g$ -thermal annealing of a glassy polymer may also result in a change of the XRD-spectra [88]. Amorphous carbons are also sensitive to this technique, which has been used to report changes in their microstructure as the pyrolysis temperature increased. For example, carbonizing Matrimid® at 800 °C enhanced its 3.8 Å peak compared to its 550 °C-CMS analog [58].

#### 2.2.4.2 Brunauer, Emmett and Teller (BET) Theory with $N_2$

Exposing a microporous solid to an atmosphere comprising a known gas in an isolated environment allows the estimation of the material sorption capability. If the system is kept isothermal, the shape of the sorption uptake trend at higher pressures provides

insight about the way the molecules enter and interact with the membrane cavities. Furthermore, several models may be used to infer features of the membrane from this sorption data. The BET model is the most popular tool used to assess the surface area of a porous medium [89]. N<sub>2</sub> is used as a molecular probe at -196 °C to cover the whole range of gas activity (i.e. saturated vapor pressure of N<sub>2</sub> at that temperature is 1 bar). The BET model is described by the following equation:

$$\frac{1}{v[(p_0/p) - 1]} = \frac{c - 1}{v_m} \frac{p}{p_0} + \frac{1}{v_m c}$$

Where  $p_0$  is the saturation pressure,  $p$  is the equilibrium pressure,  $v$  is the quantity of adsorbed gas,  $v_m$  is the monolayer adsorbed gas quantity, and  $c$  is the BET constant. This equation was estimated by assuming a Langmuir behavior of non-interacting equilibrium layers of gas adsorption. This method may be limited to those systems that do not show N<sub>2</sub> diffusion limitations at the very low temperatures at which the sorption experiment takes place [90].

#### *2.2.4.3 NLDFT method for the estimation of the membrane pore size distribution with CO<sub>2</sub> at 0 °C*

CO<sub>2</sub> is a smaller molecule than N<sub>2</sub> and should therefore be less restricted by diffusion limitations. CO<sub>2</sub> may be used as a probe of ultramicropores (< 7 Å) which are necessary for molecular size discrimination [91]. The non-local density functional theory (NLDFT) is the preferred technique to assess the inner structure of materials because it is rigorous in its evaluation of the adsorbate/adsorbent energy interactions. This computational technique deconvolutes the experimental adsorption isotherm into a

collection of theoretical isotherms of fixed pore widths [92, 93]. Therefore, the pore size distribution of the medium is determined by minimizing the grand potential of the fluid confined in those pores [94]. Furthermore, results obtained from the NLDFT method are very consistent compared to other analytical techniques, such as XRD [95].

### 2.3 *Non-idealities of membranes that could compromise their long-term performance*

#### 2.3.1 *Aging in glassy systems and its influence on transport properties*

Glassy polymers may densify over time due to a tendency of their chains to relax, and occupy the transient *FFV* [96]. This phenomenon is called physical aging, and it has been the subject of significant academic attention [97-99]. The aging behavior of the polymer chains is a kinetic effect. Therefore, it is dependent on the thickness of the film itself [100]. A reduction in permeability is expected after the chains have relaxed and occupied some of the initial *FFV*. For example, 20-nm-thick PSF presented an O<sub>2</sub> permeability change from 1.4 to 0.7 Barrer over a period of 1000 hours [101], which translated into a rise in its O<sub>2</sub>/N<sub>2</sub> selectivity from 5.8 to 6.3. Furthermore, Wang et al. demonstrated that the CH<sub>4</sub> permeability in a 1000-nm-thick 6FDA-HAB film decreased by a factor of 5 in 2000 hours [102]. The overall aging effect is more prominent in the thinner films (e.g. < 1 μm); therefore, thinner films reach a plateau in their transport properties to approach their equilibrium state faster [103, 104].

Like their lower *FFV* counterparts, intrinsically microporous polymers have been reported to age significantly [105, 106]. Ma et al. reported that SBFDA-DMN aged significantly where its O<sub>2</sub>/N<sub>2</sub> selectivity improved from 3 to 5 which is slightly above the

2008 Robeson tradeoff for that system [107]. Alghunaimi et al. reported a 15% permeability loss on various iptycene-derived polyimide analogs over a period of 150 days [108].

Similar to glassy polymers, an aging/thickness-dependent effect has been detected for CMS films [109]. This aging behavior has been particularly detrimental for very permeable and thin CMS films. Furthermore, oxygen chemisorption could block the CMS pores and potentially reduce permeability [69]. Indeed, the instability of the membranes under O<sub>2</sub> traces hindered the long-term separation performance of CMS greatly [110]. Conversely, ethylene/ethane separation is still a very attractive target for CMS membranes because there should be no significant presence of molecular O<sub>2</sub> in the actual distillation column [110].

The long term membrane stability is a critical design parameter of a membrane process. For economic reasons, the membrane flux is desired to remain high without compromising the selectivity. Accordingly, several techniques may be employed to counter aging of glassy polymers. For example, UV treatment for 40 minutes stabilized a PIM-1 matrix [111], which resulted in a 2-fold increase in aging resistance; after two months of testing, the methane pure gas permeability in PIM-1 only decreased by 20% compared to the 60% loss in the untreated polymer. Mixed polymeric-nanoparticles systems may be more tolerant to aging decay [112]. Mateucci et al. reported that TiO<sub>2</sub> nanoparticles allowed PTMSP to retain 80% of its CO<sub>2</sub> permeability as opposed to the pristine analog that lost 50% of its original permeation in a period of 120 days [113].



### 2.3.2 Plasticization and competitive sorption during mixed-gas settings

Membrane researchers commonly report the transport properties of pure feeds at 1-2 bar upstream pressure and vacuum downstream [107] that may hide some detrimental effects during real gas processing [114]. Most significantly, the membrane material itself may not be stable to the high activity of condensable molecules [115]. A permeant could act as a plasticizer and enhance the chain mobility of a membrane matrix [116]. Plasticization in a polymer takes place when there is a decrease in the local  $T_g$  in the neighborhood of a chain. Glassy polymers are vulnerable to penetrant-induced plasticization effects that reduce their gas separation performance [117]. Bos et al. correlated the CO<sub>2</sub> permeability change with varying upstream pressure [118]. The minima in the CO<sub>2</sub> permeability vs. pressure (i.e. the plasticization pressure) of Matrimid® took place around 15 bar. More importantly, the CO<sub>2</sub>/CH<sub>4</sub> binary mixture permeation test elucidated an increase on the CH<sub>4</sub> permeation rate much *earlier* than the original pure-gas plasticization pressure.

In addition to potential matrix swelling effects, gas molecules may compete for sorption sites while traversing a membrane at the same time. In the absence of plasticization, competitive sorption would translate into a permeability reduction for either permeating component [119]. A critical case of competitive sorption could occur if there are traces of a component that may systematically block the membrane pores. For example, CO<sub>2</sub> and CH<sub>4</sub> had up to ~25% permeability decrease through PBO-6FDA-HAB when the feed was saturated with water [120].

## 2.4 References

- [1] M. Mulder, Basic principles of membrane technology. Kluwer, Dordrecht, 1991.
- [2] W. Steckelmacher, Knudsen flow 75 years on: the current state of the art for flow of rarefied gases in tubes and systems, *Rep. Prog. Phys.*, 49 (1986) 1083.
- [3] P.T. Cardew and M.S. Le, Membrane processes: a technology guide, Royal Society of Chemistry, Cambridge, 1998.
- [4] J.G. Wijmans, R.W. Baker, The solution-diffusion model: a review, *J. Membr. Sci.*, 107 (1995) 1-21.
- [5] S. Thomas, I. Pinnau, N. Du, M.D. Guiver, Pure- and mixed-gas permeation properties of a microporous spirobisindane-based ladder polymer (PIM-1), *J. Membr. Sci.*, 333 (2009) 125-131.
- [6] F. Stoeckli, A. Slasli, D. Hugi-Cleary, A. Guillot, The characterization of microporosity in carbons with molecular sieve effects, *Microporous Mesoporous Mater.*, 51 (2002) 197-202.
- [7] [http://www.co2crc.com.au/aboutccs/cap\\_membranes.html](http://www.co2crc.com.au/aboutccs/cap_membranes.html).
- [8] S.C. George, S. Thomas, Transport phenomena through polymeric systems, *Prog. Polym. Sci.*, 26 (2001) 985-1017.
- [9] J.H. Gibbs, E.A. DiMarzio, Nature of the glass transition and the glassy state, *J. Chem. Phys.*, 28 (1958) 373-383.
- [10] S.M. Jordan, W.J. Koros, Permeability of pure and mixed gases in silicone rubber at elevated pressures, *J. Polym. Sci., Part B: Polym. Phys.*, 28 (1990) 795-809.
- [11] J.Y. Park, D.R. Paul, Correlation and prediction of gas permeability in glassy polymer membrane materials via a modified free volume based group contribution method, *J. Membr. Sci.*, 125 (1997) 23-39.
- [12] V. Ryzhikh, D. Tsarev, A. Alentiev, Y. Yampolskii, A novel method for predictions of the gas permeation parameters of polymers on the basis of their chemical structure, *J. Membr. Sci.*, 487 (2015) 189-198.
- [13] A. Bondi, Van der Waals volumes and radii, *J. Phys. Chem.*, 68 (1964) 441-451.
- [14] F.W. Mercer, M.T. McKenzie, A. Easteal, S.J. Moses, Synthesis and properties of new alternating copolyethers containing pendent cyano groups, *Polymer*, 35 (1994) 5355-5363.
- [15] I.A. Ronova, E.M. Rozhkov, A.Y. Alentiev, Y.P. Yampolskii, Occupied and accessible volumes in glassy polymers and their relationship with gas permeation parameters, *Macromol. Theory Simul.*, 12 (2003) 425-439.

- [16] R. Chern, W. Koros, H. Hopfenberg, V. Stannett, *Materials science of synthetic membranes*, American Chemical Society, Washington, 1985.
- [17] R.W. Baker, *Future directions of membrane gas Separation technology*, *Ind. Eng. Chem. Res.*, 41 (2002) 1393-1411.
- [18] W.J. Koros, G.K. Fleming, *Membrane-based gas separation*, *J. Membr. Sci.*, 83 (1993) 1-80.
- [19] T.A. Barbari, S.S. Datwani, *Gas separation properties of polysulfone membranes treated with molecular bromine*, *J. Membr. Sci.*, 107 (1995) 263-266.
- [20] T.H. Kim, W.J. Koros, G.R. Husk, K.C. O'Brien, *Relationship between gas separation properties and chemical structure in a series of aromatic polyimides*, *J. Membr. Sci.*, 37 (1988) 45-62.
- [21] J.G. Victor, J.M. Torkelson, *On measuring the distribution of local free volume in glassy polymers by photochromic and fluorescence techniques*, *Macromolecules*, 20 (1987) 2241-2250.
- [22] M. Coleman, W. Koros, *Isomeric polyimides based on fluorinated dianhydrides and diamines for gas separation applications*, *J. Membr. Sci.*, 50 (1990) 285-297.
- [23] S. A. Stern, *Polymers for gas separations: the next decade*, *J. Membr. Sci.*, 94 (1994) 1-65.
- [24] F. Wang, M. Hickner, Y.S. Kim, T.A. Zawodzinski, J.E. McGrath, *Direct polymerization of sulfonated poly(arylene ether sulfone) random (statistical) copolymers: candidates for new proton exchange membranes*, *J. Membr. Sci.*, 197 (2002) 231-242.
- [25] L.M. Costello, W.J. Koros, *Effect of structure on the temperature dependence of gas transport and sorption in a series of polycarbonates*, *J. Polym. Sci., Part B: Polym. Phys.*, 32 (1994) 701-713.
- [26] B.J. Story, W.J. Koros, *Sorption and transport of CO<sub>2</sub> and CH<sub>4</sub> in chemically modified poly(phenylene oxide)*, *J. Membr. Sci.*, 67 (1992) 191-210.
- [27] S.A. Stern, Y. Mi, H. Yamamoto, A.K.S. Clair, *Structure/permeability relationships of polyimide membranes. Applications to the separation of gas mixtures*, *J. Polym. Sci., Part B: Polym. Phys.*, 27 (1989) 1887-1909.
- [28] T. Masuda, E. Isobe, T. Higashimura, K. Takada, *Poly[1-(trimethylsilyl)-1-propyne]: a new high polymer synthesized with transition-metal catalysts and characterized by extremely high gas permeability*, *J. Am. Chem. Soc.*, 105 (1983) 7473-7474.
- [29] K. Nagai, T. Masuda, T. Nakagawa, B.D. Freeman, I. Pinnau, *Poly[1-(trimethylsilyl)-1-propyne] and related polymers: synthesis, properties and functions*, *Prog. Polym. Sci.*, 26 (2001) 721-798.

- [30] V. Compañ, L.F. Del Castillo, S.I. Hernández, M.M. López-González, E. Riande, Crystallinity effect on the gas transport in semicrystalline coextruded films based on linear low density polyethylene, *J. Polym. Sci., Part B: Polym. Phys.*, 48 (2010) 634-642.
- [31] A.C. Puleo, D.R. Paul, P.K. Wong, Gas sorption and transport in semicrystalline poly(4-methyl-1-pentene), *Polymer*, 30 (1989) 1357-1366.
- [32] B.S. Ghanem, N.B. McKeown, P.M. Budd, J.D. Selbie, D. Fritsch, High-performance membranes from polyimides with intrinsic microporosity, *Adv. Mater.*, 20 (2008) 2766-2771.
- [33] P.M. Budd, E.S. Elabas, B.S. Ghanem, S. Makhseed, N.B. McKeown, K.J. Msayib, C.E. Tattershall, D. Wang, Solution-processed, organophilic membrane derived from a polymer of intrinsic microporosity, *Adv. Mater.*, 16 (2004) 456-459.
- [34] B.S. Ghanem, R. Swaidan, E. Litwiller, I. Pinnau, Ultra-microporous triptycene-based polyimide membranes for high-performance gas separation, *Adv. Mater.*, 26 (2014) 3688-3692.
- [35] B.S. Ghanem, N.B. McKeown, P.M. Budd, N.M. Al-Harbi, D. Fritsch, K. Heinrich, L. Starannikova, A. Tokarev, Y. Yampolskii, Synthesis, characterization, and gas permeation properties of a novel group of polymers with intrinsic microporosity: PIM-polyimides, *Macromolecules*, 42 (2009) 7881-7888.
- [36] X. Ma, R. Swaidan, Y. Belmabkhout, Y. Zhu, E. Litwiller, M. Jouiad, I. Pinnau, Y. Han, Synthesis and gas transport properties of hydroxyl-functionalized polyimides with intrinsic microporosity, *Macromolecules*, 45 (2012) 3841-3849.
- [37] M. Carta, R. Malpass-Evans, M. Croad, Y. Rogan, J.C. Jansen, P. Bernardo, F. Bazzarelli, N.B. McKeown, An efficient polymer molecular sieve for membrane gas separations, *Science*, 339 (2013) 303-307.
- [38] B.F. Dodge, *Chemical Engineering Thermodynamics*, McGraw-Hill Book Company, New York, 1944.
- [39] A.T. DiBenedetto, D.R. Paul, An interpretation of gaseous diffusion through polymers using fluctuation theory, *J. Polym. Sci.*, 2 (1964) 1001-1015.
- [40] A.T. DiBenedetto, Molecular properties of amorphous high polymers. II. An interpretation of gaseous diffusion through polymers, *J. Polym. Sci.*, 1 (1963) 3477-3487.
- [41] N.F.A. van der Vegt, V.A. Kusuma, B.D. Freeman, Basis of solubility versus TC correlations in polymeric gas separation membranes, *Macromolecules*, 43 (2010) 1473-1479.
- [42] S. Takishima, G. Wibawa, Y. Sato, H. Masuoka, A generalized correlation for Henry's Law constants of nonpolar solutes in four polymers, *FFE*, 211 (2003) 241-256.
- [43] S. Kanehashi, K. Nagai, Analysis of dual-mode model parameters for gas sorption in glassy polymers, *J. Membr. Sci.*, 253 (2005) 117-138.

- [44] D.R. Paul, Gas sorption and transport in glassy polymers, *Berichte der Bunsengesellschaft für physikalische Chemie*, 83 (1979) 294-302.
- [45] L.M. Robeson, Correlation of separation factor versus permeability for polymeric membranes, *J. Membr. Sci.*, 62 (1991) 165-185.
- [46] B.D. Freeman, Basis of permeability/selectivity tradeoff relations in polymeric gas separation membranes, *Macromolecules*, 32 (1999) 375-380.
- [47] M. Rungta, C. Zhang, W.J. Koros, L. Xu, Membrane-based ethylene/ethane separation: The upper bound and beyond, *AIChE Journal*, 59 (2013) 3475-3489.
- [48] S.S. Chan, R. Wang, T.-S. Chung, Y. Liu, C2 and C3 hydrocarbon separations in poly(1,5-naphthalene-2,2'-bis(3,4-phthalic) hexafluoropropane) diimide (6FDA-1,5-NDA) dense membranes, *J. Membr. Sci.*, 210 (2002) 55-64.
- [49] K. Tanaka, A. Taguchi, J. Hao, H. Kita, K. Okamoto, Permeation and separation properties of polyimide membranes to olefins and paraffins, *J. Membr. Sci.*, 121 (1996) 197-207.
- [50] C. Staudt-Bickel, W.J. Koros, Olefin/paraffin gas separations with 6FDA-based polyimide membranes, *J. Membr. Sci.*, 170 (2000) 205-214.
- [51] A.J. Bird, D.L. Trimm, Carbon molecular sieves used in gas separation membranes, *Carbon*, 21 (1983) 177-180.
- [52] E. Fitzer, W. Schaefer, S. Yamada, The formation of glasslike carbon by pyrolysis of polyfurfuryl alcohol and phenolic resin, *Carbon*, 7 (1969) 643-648.
- [53] C.W. Jones, W.J. Koros, Carbon molecular sieve gas separation membranes - I. Preparation and characterization based on polyimide precursors, *Carbon*, 32 (1994) 1419-1425.
- [54] O.T. Inal, N. Leca, L. Keller, Characterization of polyacrylonitrile based carbon fibers, *Phys. Status Solidi A*, 62 (1980) 681-693.
- [55] M. Inagaki, N. Ohta, Y. Hishiyama, Aromatic polyimides as carbon precursors, *Carbon*, 61 (2013) 1-21.
- [56] J.E. Koresh, A. Soffer, The carbon molecular sieve membranes. General properties and the permeability of CH<sub>4</sub>/H<sub>2</sub> Mixture, *Sep. Sci. Technol.*, 22 (1987) 973-982.
- [57] A.B. Fuertes, I. Menendez, Separation of hydrocarbon gas mixtures using phenolic resin-based carbon membranes, *Sep. Purif. Technol.*, 28 (2002) 29-41.
- [58] K.M. Steel, W.J. Koros, Investigation of porosity of carbon materials and related effects on gas separation properties, *Carbon*, 41 (2003) 253-266.
- [59] S. Fu, E.S. Sanders, S.S. Kulkarni, W.J. Koros, Carbon molecular sieve membrane structure–property relationships for four novel 6FDA based polyimide precursors, *J. Membr. Sci.*, 487 (2015) 60-73.

- [60] L. Shao, T.-S. Chung, K.P. Pramoda, The evolution of physicochemical and transport properties of 6FDA-durene toward carbon membranes; from polymer, intermediate to carbon, *Microporous Mesoporous Mater.*, 84 (2005) 59-68.
- [61] Y.H. Sim, H. Wang, F.Y. Li, M.L. Chua, T.-S. Chung, M. Toriida, S. Tamai, High performance carbon molecular sieve membranes derived from hyperbranched polyimide precursors for improved gas separation applications, *Carbon*, 53 (2013) 101-111.
- [62] X. Zhang, H. Hu, Y. Zhu, S. Zhu, Carbon molecular sieve membranes derived from phenol formaldehyde novolac resin blended with poly(ethylene glycol), *J. Membr. Sci.*, 289 (2007) 86-91.
- [63] K. Dasgupta, D. Sathiyamoorthy, Disordered carbon—its preparation, structure, and characterisation, *Mater. Sci. Technol.*, 19 (2003) 995-1002.
- [64] K.M. Steel, W.J. Koros, An investigation of the effects of pyrolysis parameters on gas separation properties of carbon materials, *Carbon*, 43 (2005) 1843-1856.
- [65] K. Chrissafis, Kinetics of thermal degradation of polymers, *J. Therm. Anal. Calorim.*, 95 (2008) 273-283.
- [66] X. Ma, R. Swaidan, B. Teng, H. Tan, O. Salinas, E. Litwiller, Y. Han, I. Pinnau, Carbon molecular sieve gas separation membranes based on an intrinsically microporous polyimide precursor, *Carbon*, 62 (2013) 88-96.
- [67] S.M. Saufi, A.F. Ismail, Fabrication of carbon membranes for gas separation—a review, *Carbon*, 42 (2004) 241-259.
- [68] H. Suda, K. Haraya, Alkene/alkane permselectivities of a carbon molecular sieve membrane, *Chem. Commun.*, (1997) 93-94.
- [69] M. Kiyono, P.J. Williams, W.J. Koros, Effect of pyrolysis atmosphere on separation performance of carbon molecular sieve membranes, *J. Membr. Sci.*, 359 (2010) 2-10.
- [70] M. Kiyono, P.J. Williams, W.J. Koros, Effect of polymer precursors on carbon molecular sieve structure and separation performance properties, *Carbon*, 48 (2010) 4432-4441.
- [71] H. Qinglin, S.M. Sundaram, S. Farooq, Revisiting transport of gases in the micropores of carbon molecular sieves, *Langmuir*, 19 (2003) 393-405.
- [72] X. Ning, W.J. Koros, Carbon molecular sieve membranes derived from Matrimid® polyimide for nitrogen/methane separation, *Carbon*, 66 (2014) 511-522.
- [73] L.H. Sperling, *Introduction to physical polymer science*, John Wiley & Sons, New Jersey, 2005.
- [74] S. Montserrat, P. Colomer, The effect of the molecular weight on the glass transition temperature in amorphous poly(ethylene terephthalate), *Polym. Bull.*, 12 173-180.

- [75] K.T. Woo, J. Lee, G. Dong, J.S. Kim, Y.S. Do, W.-S. Hung, K.-R. Lee, G. Barbieri, E. Drioli, Y.M. Lee, Fabrication of thermally rearranged (TR) polybenzoxazole hollow fiber membranes with superior CO<sub>2</sub>/N<sub>2</sub> separation performance, *J. Membr. Sci.*, 490 (2015) 129-138.
- [76] N.A. Mohamed, N.A. Abd El-Ghany, M.M. Fahmy, Thermogravimetric analysis in the evaluation of the inhibition of degradation of rigid poly(vinyl chloride) using biologically active phthalimido aromatic hydrazide derivatives, *Polym. Degrad. Stab.*, 128 (2016) 46-54.
- [77] C. Joly, D. Le Cerf, C. Chappey, D. Langevin, G. Muller, Residual solvent effect on the permeation properties of fluorinated polyimide films, *Sep. Purif. Technol.*, 16 (1999) 47-54.
- [78] H.B. Park, S.H. Han, C.H. Jung, Y.M. Lee, A.J. Hill, Thermally rearranged (TR) polymer membranes for CO<sub>2</sub> separation, *J. Membr. Sci.*, 359 (2010) 11-24.
- [79] Z.P. Smith, G. Hernández, K.L. Gleason, A. Anand, C.M. Doherty, K. Konstas, C. Alvarez, A.J. Hill, A.E. Lozano, D.R. Paul, B.D. Freeman, Effect of polymer structure on gas transport properties of selected aromatic polyimides, polyamides and TR polymers, *J. Membr. Sci.*, 493 (2015) 766-781.
- [80] M.L. Jue, R.P. Lively, Targeted gas separations through polymer membrane functionalization, *React. Funct. Polym.*, 86 (2015) 88-110.
- [81] C.W. Wilson, E.R. Santee, Polymer analysis by high-resolution NMR, with applications to poly(vinylidene fluoride) and poly(vinyl fluoride), *J. Polym. Sci. Pol. Sym.*, 8 (1965) 97-112.
- [82] H.-J. Scheibe, D. Drescher, P. Alers, Raman characterization of amorphous carbon films, *Fresen. J. Anal. Chem.*, 353 (1995) 695-697.
- [83] C. Suryanarayana, M.G. Norton, X-ray diffraction: a practical approach, Springer Science & Business Media, New York, 2013.
- [84] M. Northolt, X-ray diffraction study of poly (p-phenylene terephthalamide) fibres, *Eur. Polym. J.*, 10 (1974) 799-804.
- [85] J.P. Pouget, M.E. Jozefowicz, A.J. Epstein, X. Tang, A.G. MacDiarmid, X-ray structure of polyaniline, *Macromolecules*, 24 (1991) 779-789.
- [86] X. Du, E. Wu, Porosity of microporous zeolites A, X and ZSM-5 studied by small angle X-ray scattering and nitrogen adsorption, *J. Phys. Chem. Solids*, 68 (2007) 1692-1699.
- [87] A. Windle, X-ray scattering measurements of order in non-crystalline polymers, *Pure Appl. Chem.*, 57 (1985) 1627-1638.
- [88] G.R. Mitchell, A.H. Windle, The effect of annealing on the local structure of glassy polycarbonate, *Colloid. Polym. Sci.*, 263 (1985) 280-285.

- [89] J.B. Condon, Surface area and porosity determinations by physisorption: measurements and theory, Elsevier, Amsterdam, 2006.
- [90] D. Lozano-Castelló, D. Cazorla-Amorós, A. Linares-Solano, Usefulness of CO<sub>2</sub> adsorption at 273 K for the characterization of porous carbons, *Carbon*, 42 (2004) 1233-1242.
- [91] D. Lozano-Castelló, D. Cazorla-Amorós, A. Linares-Solano, D.F. Quinn, Micropore size distributions of activated carbons and carbon molecular sieves assessed by high-pressure methane and carbon dioxide adsorption isotherms, *J. Phys. Chem. B*, 106 (2002) 9372-9379.
- [92] J. Landers, G.Y. Gor, A.V. Neimark, Density functional theory methods for characterization of porous materials, *Colloids Surf. A*, 437 (2013) 3-32.
- [93] C. Lastoskie, K.E. Gubbins, N. Quirke, Pore size distribution analysis of microporous carbons: a density functional theory approach, *J. Phys. Chem.*, 97 (1993) 4786-4796.
- [94] J. Jagiello, W. Betz, Characterization of pore structure of carbon molecular sieves using DFT analysis of Ar and H<sub>2</sub> adsorption data, *Microporous Mesoporous Mater.*, 108 (2008) 117-122.
- [95] J. Jagiello, M. Thommes, Comparison of DFT characterization methods based on N<sub>2</sub>, Ar, CO<sub>2</sub>, and H<sub>2</sub> adsorption applied to carbons with various pore size distributions, *Carbon*, 42 (2004) 1227-1232.
- [96] D. Cangialosi, V.M. Boucher, A. Alegria, J. Colmenero, Physical aging in polymers and polymer nanocomposites: recent results and open questions, *Soft Matter*, 9 (2013) 8619-8630.
- [97] J.M. Hutchinson, Physical aging of polymers, *Prog. Polym. Sci.*, 20 (1995) 703-760.
- [98] R. Swaidan, B. Ghanem, E. Litwiller, I. Pinnau, Physical aging, plasticization and their effects on gas permeation in “rigid” polymers of intrinsic microporosity, *Macromolecules*, 48 (2015) 6553-6561.
- [99] M.S. McCaig, D.R. Paul, Effect of film thickness on the changes in gas permeability of a glassy polyarylate due to physical aging. Part I. Experimental observations, *Polymer*, 41 (2000) 629-637.
- [100] P.H. Pfromm, W.J. Koros, Accelerated physical ageing of thin glassy polymer films: evidence from gas transport measurements, *Polymer*, 36 (1995) 2379-2387.
- [101] B.W. Rowe, B.D. Freeman, D.R. Paul, Physical aging of ultrathin glassy polymer films tracked by gas permeability, *Polymer*, 50 (2009) 5565-5575.
- [102] H. Wang, T.-S. Chung, D.R. Paul, Physical aging and plasticization of thick and thin films of the thermally rearranged ortho-functional polyimide 6FDA-HAB, *J. Membr. Sci.*, 458 (2014) 27-35.



- [103] Y. Huang, D.R. Paul, Physical aging of thin glassy polymer films monitored by gas permeability, *Polymer*, 45 (2004) 8377-8393.
- [104] L. Cui, W. Qiu, D.R. Paul, W.J. Koros, Physical aging of 6FDA-based polyimide membranes monitored by gas permeability, *Polymer*, 52 (2011) 3374-3380.
- [105] C.L. Staiger, S.J. Pas, A.J. Hill, C.J. Cornelius, Gas separation, free volume distribution, and physical aging of a highly microporous spirobisindane polymer, *Chem. Mater.*, 20 (2008) 2606-2608.
- [106] R. Swaidan, M. Al-Saeedi, B. Ghanem, E. Litwiller, I. Pinnau, Rational design of intrinsically ultramicroporous polyimides containing bridgehead-substituted triptycene for highly selective and permeable gas separation membranes, *Macromolecules*, 47 (2014) 5104-5114.
- [107] L.M. Robeson, The upper bound revisited, *J. Membr. Sci.*, 320 (2008) 390-400.
- [108] F. Alghunaimi, B. Ghanem, N. Alaslai, R. Swaidan, E. Litwiller, I. Pinnau, Gas permeation and physical aging properties of triptycene diamine-based microporous polyimides, *J. Membr. Sci.*, 490 (2015) 321-327.
- [109] L. Xu, M. Rungta, J. Hessler, W. Qiu, M. Brayden, M. Martinez, G. Barbay, W.J. Koros, Physical aging in carbon molecular sieve membranes, *Carbon*, 80 (2014) 155-166.
- [110] I. Menendez, A.B. Fuertes, Aging of carbon membranes under different environments, *Carbon*, 39 (2001) 733-740.
- [111] F.Y. Li, T.-S. Chung, Physical aging, high temperature and water vapor permeation studies of UV-rearranged PIM-1 membranes for advanced hydrogen purification and production, *Int. J. Hydrogen Energy*, 38 (2013) 9786-9793.
- [112] P. Rittigstein, J.M. Torkelson, Polymer-nanoparticle interfacial interactions in polymer nanocomposites: confinement effects on glass transition temperature and suppression of physical aging, *J. Polym. Sci., Part B: Polym. Phys.*, 44 (2006) 2935-2943.
- [113] S. Matteucci, V.A. Kusuma, D. Sanders, S. Swinnea, B.D. Freeman, Gas transport in TiO<sub>2</sub> nanoparticle-filled poly(1-trimethylsilyl-1-propyne), *J. Membr. Sci.*, 307 (2008) 196-217.
- [114] H. Lin, M. Yavari, Upper bound of polymeric membranes for mixed-gas CO<sub>2</sub>/CH<sub>4</sub> separations, *J. Membr. Sci.*, 475 (2015) 101-109.
- [115] M.D. Donohue, B.S. Minhas, S.Y. Lee, Permeation behavior of carbon dioxide-methane mixtures in cellulose acetate membranes, *J. Membr. Sci.*, 42 (1989) 197-214.
- [116] E.S. Sanders, Penetrant-induced plasticization and gas permeation in glassy polymers, *J. Membr. Sci.*, 37 (1988) 63-80.
- [117] A.F. Ismail, W. Lorna, Penetrant-induced plasticization phenomenon in glassy polymers for gas separation membrane, *Sep. Purif. Technol.*, 27 (2002) 173-194.

- [118] A. Bos, I.G.M. Pünt, M. Wessling, H. Strathmann, Plasticization-resistant glassy polyimide membranes for CO<sub>2</sub>/CO<sub>4</sub> separations, *Sep. Purif. Technol.*, 14 (1998) 27-39.
- [119] T. Visser, G.H. Koops, M. Wessling, On the subtle balance between competitive sorption and plasticization effects in asymmetric hollow fiber gas separation membranes, *J. Membr. Sci.*, 252 (2005) 265-277.
- [120] C.A. Scholes, B.D. Freeman, S.E. Kentish, Water vapor permeability and competitive sorption in thermally rearranged (TR) membranes, *J. Membr. Sci.*, 470 (2014) 132-137.

## Chapter 3

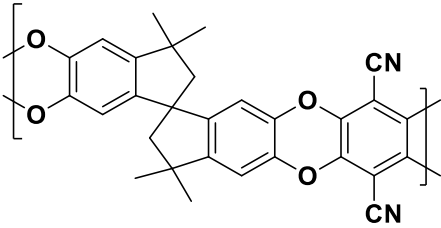
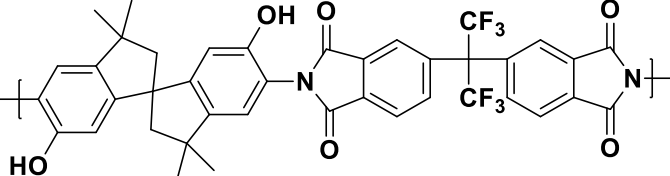
### Materials and Experimental Procedures

In this chapter, the PIM materials and the experimental procedures used in this work are described.

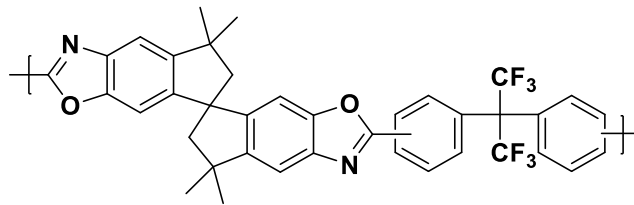
#### 3.1 Materials and thesis organization

The polymers presented in **Table 3.1** were evaluated as potential candidates for ethylene/ethane separation, which is the main topic of **Chapter 4** of this work. Furthermore, PIM-1, PIM-6FDA-OH and PIM-6FDA were used as pyrolysis substrates to generate CMS membranes, as discussed in **Chapters 5, 6** and **7**.

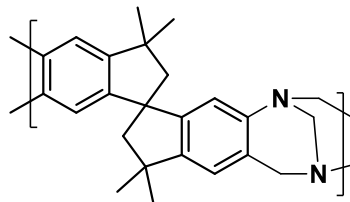
**Table 3.1.** Chemical structure of the PIMs tested in this work

Name	Chemical Structure
PIM-1	
PIM-6FDA-OH	

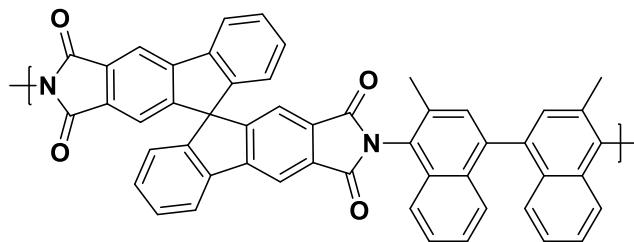
PIM-6FDA



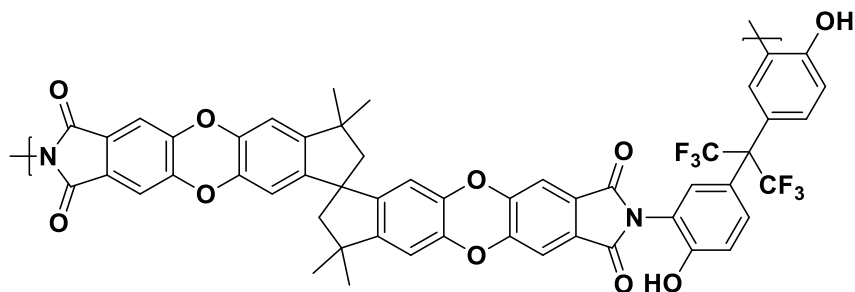
PIM-SBI-TB



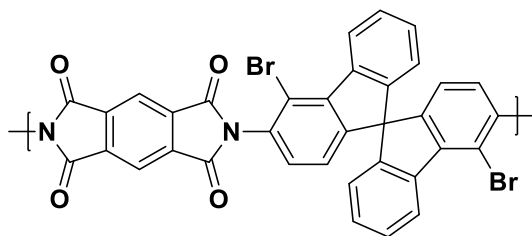
SBFDA-DMN



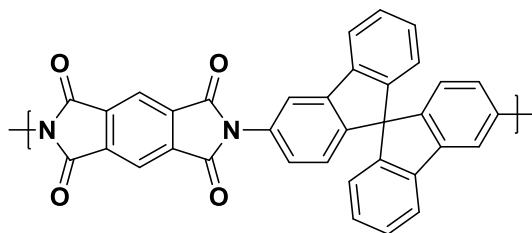
SPDA-APAF



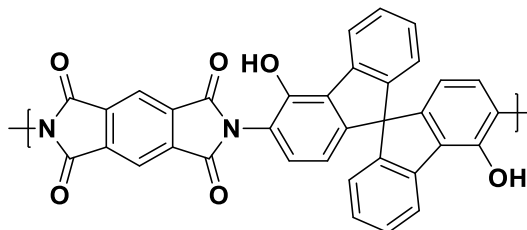
PMDA-BSBF



PMDA-SBF



PMDA-HSBF



### 3.1.1 Synthetic procedures

PIM-1 was synthesized by Dr. Bader Ghanem of the AMPMC according to the procedure of Du et al. [1]: 5,5',6,6'-tetrahydroxy-3,3,3',3'-tetramethyl-spirobisindane and 1,4-dicyanotetrafluorobenzene were reacted via polycondensation to generate the ladder polymer. PIM-6FDA-OH followed the synthesis by Ma et al. [2]. PIM-SBI-TB and SPDA-APAF were produced according to the methods elucidated by Carta et. al [3], and Shamsipur et. al [4], respectively. Furthermore, PMDA-SBF [5], PMDA-BSBF [5], and SBFDA-DMN [32] followed the synthetic path described by Ma et al. [6]. PMDA-HSBF is a new PIM of the spirobifluorene family whose synthetic procedure was the same as the previously reported synthesis of 6FDA-HSBF [7]. The resulting polyimide was obtained as a yellow powder with a yield of 96%.  $^1\text{H NMR}$  (400MHz,  $\text{DMSO-d}_6$ ):  $\delta$  10.13 (s, 2H), 8.53 (s, 2H), 8.07 (s, 2H), 7.92 (s, 2H), 7.47 (s, 4H), 7.20 (s, 2H), 6.82 (s, 2H), 6.38 (s, 2H). Lastly, PIM-6FDA was synthesized following the same general procedure previously reported for PIM-6FDA-OH [2]. PIM-6FDA was obtained as light yellow filaments with a yield of 95%.  $^1\text{H NMR}$  (500 MHz,  $\text{CDCl}_3$ ):  $\delta$  8.00 -8.05 (m, 2H), 7.88 -7.94 (m, 4H), 7.15 -7.32 (m, 4H), 6.85 -7.02 (m, 2H), 2.33 -2.44 (m, 4H), 1.39 - 1.44 (m, 12H).

### 3.2 Dense film fabrication

Dense polymeric films were made by the following general procedure:

- Dissolution of the polymer in the solvent at 3% w/v (see **Table 3.2**).
- Pouring of the solution into a glass Petri dish with a syringe while filtering the solution using a 0.45- $\mu\text{m}$  PTFE cartridge.
- Slow evaporation of 3% w/v polymer/solvent solutions covered in a glass Petri dish under ambient conditions.
- Air drying for 12 hours after casting of the film.
- Non-solvent conditioning, whenever applied (see **Table 3.2**).
- Drying under high vacuum to remove remaining solvent (see **Table 3.2**).
- Film thickness measured with a digital micrometer.
- Film densities were determined gravimetrically by measuring the weight of the films using a microbalance (Mettler Toledo) and their area with a scanner.
- Heat-treatment protocol (only for PIM-1, PIM-6FDA-OH, and PIM-6FDA).

**Table 3.2.** Membrane preparation conditions of the dense isotropic films.

Polymer	Casting solvent	Non-solvent conditioning	Drying temperature (°C) <sup>a</sup>
PIM-1	THF	CH <sub>3</sub> OH 12 hour soak	250
PIM-6FDA-OH	THF	no	250
PIM-6FDA	THF	no	250
PIM-SBI-TB	CHCl <sub>3</sub>	CH <sub>3</sub> OH 24 hour soak	120
SBFDA-DMN	CHCl <sub>3</sub>	CH <sub>3</sub> OH 24 hour soak	120

SPDA-APAF	THF	no	250
PMDA-BSBF	CHCl <sub>3</sub>	CH <sub>3</sub> OH 24 hour soak	120
PMDA-SBF	CHCl <sub>3</sub>	CH <sub>3</sub> OH 24 hour soak	120
PMDA-HSBF	THF	no	250

<sup>a</sup> heated for 24 hours under high vacuum.

### 3.3 Thermal-treatment protocol

Round, 25 mm diameter polymeric films were placed inside a Carbolite three-zone tube furnace (**Fig. 3.1**) in a quartz tube supplied with 1000 cm<sup>3</sup>(STP) min<sup>-1</sup> of N<sub>2</sub> from a mass flow controller. The temperature was measured with a thermocouple adjacent to the sample. The concentration of oxygen exiting the furnace was measured with a Cambridge Sensotec Rapidox 3100 and confirmed to be less than 2 ppm at all times.

The temperature protocol was ramped at 3 °C min<sup>-1</sup> and then held isothermally for 30 minutes for each thermal stage. After the isothermal soak, the furnace was allowed to cool to room temperature. The gas permeation properties of the films were immediately tested after removal from the furnace. These measures were used to ensure data reproducibility. The thermal treatment for each PIM is presented in **Table 3.3**.

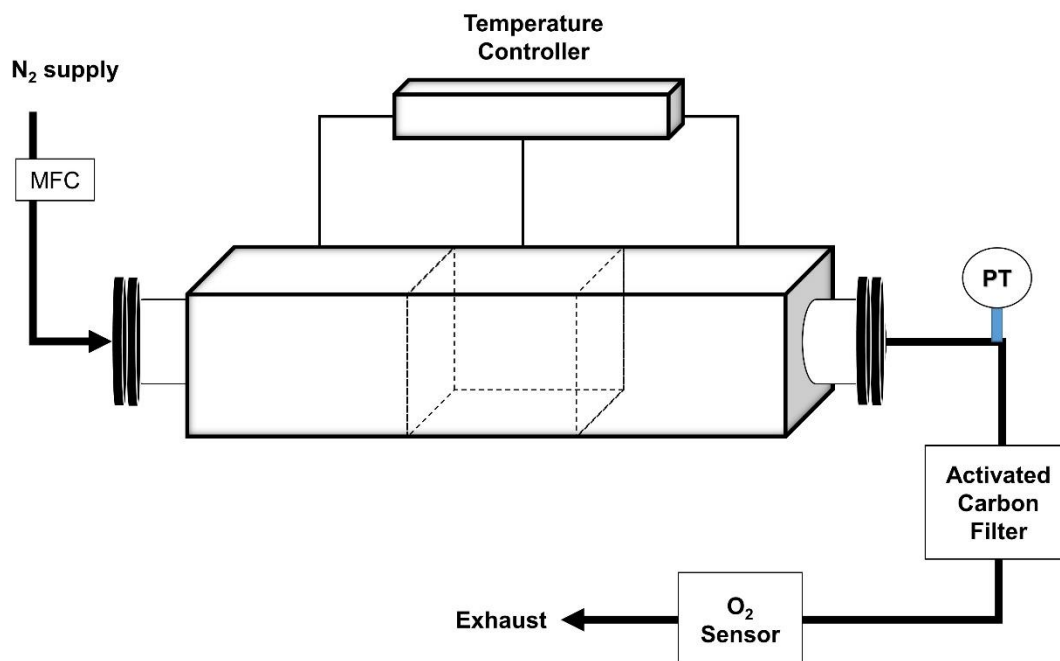


**Fig. 3.1.** Three-zone pipe furnace used to carbonize polymeric membranes.

**Table 3.3.** Protocol of the various thermally treated derivatives of PIM precursors.

Polymer	Ramping Rate (°C min <sup>-1</sup> )	Final Treatment Temperature (°C)	Soaking Time (min)
PIM-1	3	400, 600, 800	30
PIM-6FDA-OH	3	400, 500, 600, 800	30
PIM-6FDA	3	500, 600, 800	30

### 3.4 Pure-gas permeation

Gas-permeation experiments were performed at 35 °C in a constant-volume/variable-pressure apparatus as described in detail elsewhere [8]. The films were masked with special care to prevent damage under vacuum, as previously described [9].



Samples were degassed for at least 24 h to remove adsorbed molecules. Pure-gas permeability was calculated according to the following equation:

$$P_i = \frac{V_d l}{P_U T R A} \frac{dp_i}{dt},$$

where  $P_i$  is the pure-gas permeability,  $V_d$  is the downstream volume,  $l$  is the membrane thickness,  $P_U$  is the upstream pressure,  $T$  is the temperature in absolute units,  $R$  is the gas constant,  $A$  is the active permeation area, and  $dp_i/dt$  is the steady-state rise in pressure with respect to time. The pure-gas selectivity was calculated as the ratio of the pure-gas permeabilities:

$$\alpha_{i/j} = \frac{P_i}{P_j}.$$

Ultrahigh purity gases were used for permeation and sorption experiments in increasing order of condensability. O<sub>2</sub> was tested at the end in carbonaceous samples to prevent any chemisorption from taking place.

#### *3.4.1 Pure-gas permeation apparatus and testing protocol*

A custom-made permeation setup was used to measure the permeation properties, as detailed in the following procedure referenced to the scheme of the apparatus shown in

**Fig. 3.2:**

- Shutdown vacuum pump
- Remove old masked membrane
- Install new membrane
- Close all valves

- Turn on vacuum pump
- Open  $v_4$  to keep recently installed membrane fixed
- Apply epoxy and wait for it to dry
- Close permeation cell
- Open all valves except  $v_1$  (to degas the system)
- Close all valves
- Connect gas cylinder and open  $v_1$  to purge the system
- Regulate the upstream pressure and close  $v_1$
- Open  $v_2$  to start the permeation

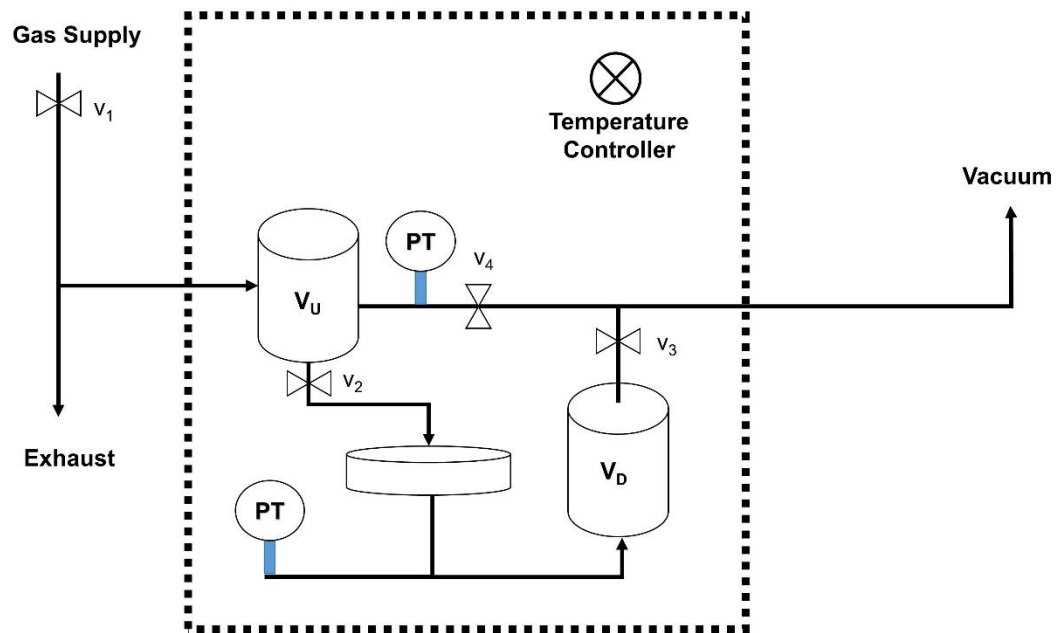


**Fig. 3.2.** Schematic representation of a pure-gas permeation setup.

### 3.5 Mixed-gas permeation

The mixed-gas permeability was measured with a 50:50 v/v ethylene/ethane mixture by the general technique described by O'Brien et al. [10]. The stage-cut, that is the permeate to feed flow rate, was less than 1%. Under this condition, the feed and residue concentrations were essentially equivalent. The feed and permeate compositions were determined with an Agilent 3000A Micro GC. Mixed-gas permeabilities were calculated as follows:

$$P_i = \frac{y_i V_d l}{x_i P_U T R A} \frac{dp}{dt},$$

where  $P_i$  is the permeability of the component  $i$ ,  $y_i$  and  $x_i$  are the molar fractions of  $i$  in the permeate and feed, respectively. Finally, the mixed-gas selectivity was calculated by,

$$\alpha_{i/j} = \frac{y_i/x_i}{y_j/x_j}.$$

The procedure used to obtain mixed-gas data is very similar to that described for the pure-gas experiment, with the following additions (**Fig. 3.3**):

- GC calibration with at least 5 mixtures covering the range of concentrations expected in the permeate is required prior to the experiment.
- The gas supply needs to be available throughout the test; therefore,  $v_1$  should remain open while permeating the mixture.

- Control the retentate flow to less than 1% by using  $v_5$ .
- At the beginning of the experiment open  $v_1$  and  $v_2$ , close the rest.
- Wait for the pressure rate increase to be constant.
- Discard that volume of gas by slowly opening  $v_3$ .
- Accumulate the permeate so that it matches your calibration pressure and sample to the GC using  $v_6$ .

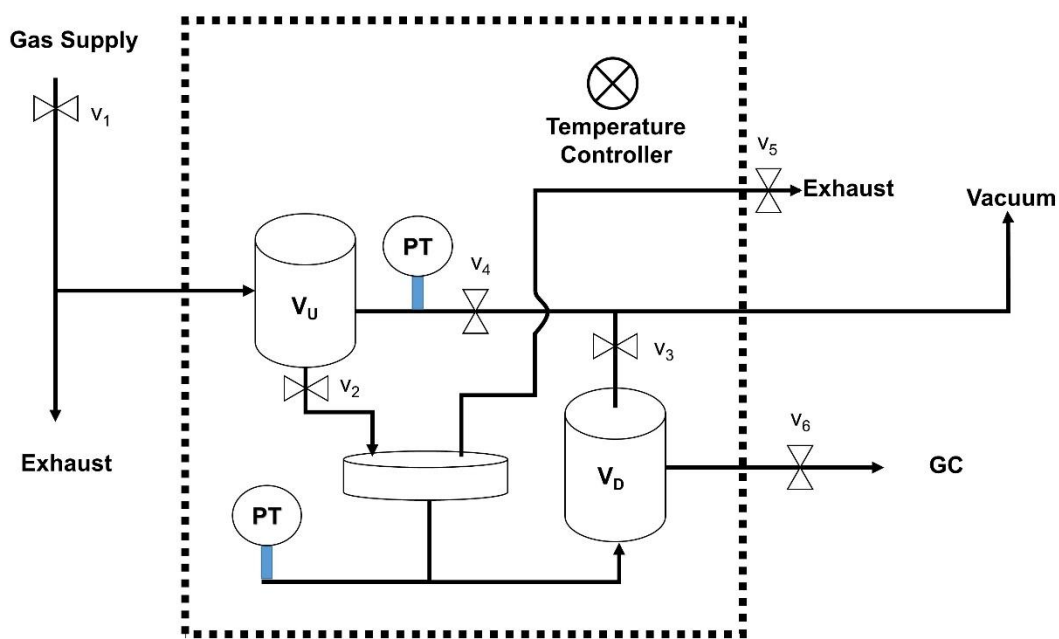


**Fig. 3.3.** Schematic representation of a mixed-gas permeation setup.

### 3.6 Morphology characterization

#### 3.6.1 TGA

A thermogravimetric analyzer (TGA, TA Instruments) was used to measure sample weight loss as a function of pyrolysis temperature. Evolved gases were identified with a

quadrupole mass spectrometer (Hiden Analytical) coupled to the TGA with N<sub>2</sub> as the carrier gas.

### 3.6.2 FTIR

Fourier-transform infrared (FTIR) spectra were acquired using a Thermo Nicolet iS10 infrared micro-spectrometer.

### 3.6.3 XRD

X-ray diffraction (XRD) scattering was conducted on a Bruker D8 Advance diffractometer. Raman spectra of the carbonized films were obtained with a Horiba LabRam HR visible microscope.

### 3.6.4 Micromeritics ASAP 2020

The internal structure of the samples was studied by CO<sub>2</sub> sorption at 0 °C using a Micromeritics 2020. The pore-size distribution was calculated with the nonlocal density functional theory (NLDFT) model assuming a carbon-slit pore geometry using the software version 4.02 provided by Micromeritics.

### 3.7 Gravimetric sorption

Gravimetric sorption isotherms for pure ethylene and ethane in the pressure range 1 to 15 bar were determined at 35 °C with a Hiden IGA apparatus. To determine the sorption capacity of the PIM and the CMS samples, their density was determined gravimetrically by measuring the weight, area, and film thickness.

Gas sorption in organic glassy polymers can be described by the dual-mode sorption model [11]:

$$C = K_D p + \frac{C'_H b p}{1 + b p},$$

where  $C$  is the total gas concentration in the glassy polymer,  $K_d$  is the Henry's law coefficient,  $C'_H$  is the Langmuir hole capacity,  $b$  is the interaction parameter, and  $p$  is the gas pressure. Gas isotherms of carbon materials were expressed by the Langmuir model [12]:

$$C = \frac{C'_H b p}{1 + b p}.$$

### 3.8 References

- [1] N. Du, J. Song, G.P. Robertson, I. Pinnau, M.D. Guiver, Linear high molecular weight ladder polymer via fast polycondensation of 5,5',6,6'-tetrahydroxy-3,3,3',3'-tetramethylspirobisindane with 1,4-dicyanotetrafluorobenzene, *Macromol. Rapid Commun.*, 29 (2008) 783-788.
- [2] X. Ma, R. Swaidan, Y. Belmabkhout, Y. Zhu, E. Litwiller, M. Jouiad, I. Pinnau, Y. Han, Synthesis and gas transport properties of hydroxyl-functionalized polyimides with intrinsic microporosity, *Macromolecules*, 45 (2012) 3841-3849.
- [3] M. Carta, R. Malpass-Evans, M. Croad, Y. Rogan, J.C. Jansen, P. Bernardo, F. Bazzarelli, N.B. McKeown, An efficient polymer molecular sieve for membrane gas separations, *Science*, 339 (2013) 303-307.
- [4] H. Shamsipur, B.A. Dawood, P.M. Budd, P. Bernardo, G. Clarizia, J.C. Jansen, Thermally rearrangeable PIM-polyimides for gas separation membranes, *Macromolecules*, 47 (2014) 5595-5606.
- [5] X. Ma, O. Salinas, E. Litwiller, I. Pinnau, Novel spirobifluorene- and dibromospirobifluorene-based polyimides of intrinsic microporosity for gas separation applications, *Macromolecules*, 46 (2013) 9618-9624.
- [6] X. Ma, B. Ghanem, O. Salinas, E. Litwiller, I. Pinnau, Synthesis and effect of physical aging on gas transport properties of a microporous polyimide derived from a novel spirobifluorene-based dianhydride, *ACS Macro Lett.*, 4 (2015) 231-235.
- [7] X. Ma, O. Salinas, E. Litwiller, I. Pinnau, Pristine and thermally-rearranged gas separation membranes from novel o-hydroxyl-functionalized spirobifluorene-based polyimides, *Polymer Chemistry*, 5 (2014) 6914-6922.
- [8] D.G. Pye, H.H. Hoehn, M. Panar, Measurement of gas permeability of polymers. I. Permeabilities in constant volume/variable pressure apparatus, *J. Appl. Polym. Sci.*, 20 (1976) 1921-1931.
- [9] T.T. Moore, S. Damle, P.J. Williams, W.J. Koros, Characterization of low permeability gas separation membranes and barrier materials; design and operation considerations, *J. Membr. Sci.*, 245 (2004) 227-231.
- [10] K.C. O'Brien, W.J. Koros, T.A. Barbari, E.S. Sanders, A new technique for the measurement of multicomponent gas transport through polymeric films, *J. Membr. Sci.*, 29 (1986) 229-238.
- [11] W.R. Vieth, P.M. Tam, A.S. Michaels, Dual sorption mechanisms in glassy polystyrene, *J. Colloid Interf. Sci.*, 22 (1966) 360-370.
- [12] L. Xu, M. Rungta, J. Hessler, W. Qiu, M. Brayden, M. Martinez, G. Barbay, W.J. Koros, Physical aging in carbon molecular sieve membranes, *Carbon*, 80 (2014) 155-166.

## Chapter 4

### Ethylene/Ethane Separation with Spirobisindane-Based Intrinsically Microporous Polymeric Membranes<sup>1</sup>

This chapter reports the ethylene and ethane gas transport properties of a collection of spiro-based PIMs. These PIMs represent a suitable body to study the effects of their structure on the ethylene/ethane diffusion and sorption selectivities. The ethylene and ethane sorption isotherms indicate that essentially no preferential sorption occurs in the polymers; thus the separation is controlled by diffusion. High free volume SBFDA-DMN and PIM-SBI-TB did not show significant ethylene/ethane separation. On the other hand, the pure-gas ethylene/ethane permselectivity of the hydroxyl-functionalized PMDA-HSBF and SPDA-APAF (measured at 35 °C and 2 bar) was comparable to that of low free volume polyimides. With an ethylene permeability of 3.3 Barrer and an ethylene/ethane permselectivity of 5.1, PMDA-HSBF is the most selective PIM-PI reported to date. PIMs of the spiro family were not able to exceed the selectivity limitations predicted in the 2013 polymer ethylene/ethane upper bound.

---

<sup>1</sup>Portions of this chapter were adapted from:

X. Ma, O. Salinas, E. Litwiller, I. Pinnau, *Macromolecules*, 46 (2013) 9618-9624.

X. Ma, O. Salinas, E. Litwiller, I. Pinnau, *Polymer Chemistry*, 5 (2014) 6914-6922.

X. Ma, B. Ghanem, O. Salinas, E. Litwiller, I. Pinnau, *ACS Macro Lett.*, (2015) 231-235.

Dr. Ma and Dr. Ghanem synthesized the polymers, Salinas characterized the polymers in terms of their transport properties, Dr. Litwiller directed the permeation devices construction, Prof. Pinnau supervised the work and edited the manuscripts.



#### 4.1 Introduction

Membranes, which purify components relying on the difference in diffusion and solubility, could potentially mitigate the need for extremely energy demanding distillation columns [1]. In a prime opportunity for membrane technology application, the ethylene production represents a 141 million ton market [2]. Process simulations of ethylene/ethane distillation columns operated synergistically with a membrane unit have qualitatively predicted economic incentives compared to the stand-alone distillation technology [3]. Unfortunately, there is a limit in gas transport performance through polymeric membranes [4]. This physical limitation precludes most economical materials from simultaneously attaining high selectivity and permeability. The polymer upper bound for the ethylene/ethane gas pair was reported in 2013 by Rungta and Koros [5]. Notwithstanding, the glassy polyimides that defined this upper bound [5-10] did not include the novel materials class of polymers of intrinsic microporosity (PIMs).

PIMs bear extremely rigid contortion centers (e.g. tetrahedral spiro carbon) that prevent efficient chain packing in their solid state, thus, developing a polymeric matrix of interconnected microporosity ( $< 20 \text{ \AA}$ ) in the form of super-micropores ( $7 \text{ \AA} - 20 \text{ \AA}$ ) and ultra-micropores ( $< 7 \text{ \AA}$ ). The inner structure of a PIM material can be visualized as a series of constrictions that connect chambers that allow a significant surface area for adsorption (typically  $200 - 1000 \text{ m}^2/\text{g}$ ). A wealth of research has been dedicated to the synthesis of PIM-based materials since the creation of the prototype spirobisindane polybenzodioxane ladder polymer [11-13] (PIM-1) in 2004 and the incorporation of the spirobisindane moiety into a dianhydride that was the precursor of several polyimides of intrinsic microporosity (PIM-PI), which presented moderate selectivities and commendable versatility of

synthesis. The most recent PIMs have been tailored with even less flexible bridgehead bicyclics: Tröger's base, ethanoanthracene, and triptycene moieties, which often surpassed the 2008 polymer upper bound for several important gas pairs [14-17].

Fundamentally, three parameters control the gas transport through PIMs: i) the size and distribution of their ultra-microporous cavities, ii) the sorption capacity in the PIM structure, and iii) the PIM stability towards sorbents in terms of swelling and plasticization. These factors may be interrelated; therefore, the rational design of advanced materials is a very active research topic nowadays that demands a deep knowledge of the polymer structure influence on the final gas transport properties [18]. Side groups and functionalities modify the conformation and rigidity of PIM materials in their solid state. For example, bromine-substituted PMDA-BSBF depicted limited torsional mobility of its spirobifluorene moiety which in turn enhanced its chain rigidity and restricted its packing; thus, effectively increased the polymer permeability with a slight decrease in selectivity compared to its unsubstituted analog [19]. Conversely, pendant groups may induce physical crosslinks to bring the chains together via intra-chain polar interactions (e.g. hydrogen bonding), which also increase intra-chain rigidity; thus, enhancing the diffusion selectivity [20-23]. PIM-PIs have been evaluated for the separation of the  $C_3H_6/C_3H_8$  pair and it was found that the triptycene-based KAUST-PI-1 commanded selectivities nearly as high as that of low-free volume polymers but with unmatched permeabilities [24]. Furthermore, PIM-6FDA-OH was more permeable than comparably selective polymers for  $H_2S$  removal [25].

In spite of their novelty, PIM-based membranes have been seldom proposed for ethylene/ethane separation, except for PIM-1 [26], whose pristine structure did not allow

for a very effective discrimination of ethylene from ethane. Nevertheless, the more advanced PIMs may offer valuable candidates for this challenging application. This chapter reports the ethylene/ethane gas transport properties of various PIMs that contain a tetrahedral carbon imbedded in their structure [14, 19, 27-30].

#### 4.2 Chemical structure and physical properties of PIM structures

The chemical structures of the PIMs reported in this chapter are shown in **Fig. 4.1**. The physical properties of all materials used to fabricate isotropic 80-100  $\mu\text{m}$ -thick membranes are presented in **Table 3.1**. Their corresponding synthesis yielded high molecular weight polymers ( $> 10\,000\text{ g mol}^{-1}$ ), which guaranteed the integrity and mechanical properties of their derived isotropic films. Similarly to the original polybenzodioxane-based PIM-1 [31], all polymers presented high thermal stability in inert  $\text{N}_2$  (i.e. degradation temperatures above  $380\text{ }^\circ\text{C}$ ). However, *o*-functionalization (e.g. hydroxyl) of the PIM-PIs made the films less thermally stable compared to their unfunctionalized analogs. For example, the *ortho*-functionalities of PMDA-HSBF are known to react to form polybenzoxazole by  $\text{CO}_2$  evolution at  $\sim 400\text{ }^\circ\text{C}$  [32], whereas its unfunctionalized counterpart, PMDA-SBF, began its decomposition at  $480\text{ }^\circ\text{C}$ . The Tröger's base moiety found in PIM-SBI-TB made the polymer less resistant to heat compared to PIM-1 in spite of its stiffer backbone [14].

$\text{N}_2$  Sorption at  $-196\text{ }^\circ\text{C}$  can be used to assess the BET surface area of PIM materials [20]. The data must be analyzed with caution since very size-selective PIMs may see their surface area underestimated by diffusion constraints at the very low temperatures at which

the experiment takes place [23]. Regardless, the ladder structures of PIM-SBI-TB and PIM-1 remained the highest surface area material presented in this work, presumably by virtue of their largely interconnected array of pores and open amorphous structure [31]. On the contrary, PMDA-HSBF showed the smallest surface area among the materials tested here due to its tighter cavities, and hypothetically, diffusion restrictions imposed by its matrix at -196 °C. PMDA-SBF showed 3 times higher surface area than PMDA-HSBF, whereas the brominated PMDA-BSBF depicted the highest capacity in the spirobifluorene-diamine-based family. The BET surface area of the PIMs reported here ranged from 80 - 720 m<sup>2</sup> g<sup>-1</sup>. The polymers shown in **Table 3.1** were listed in terms of decreasing BET surface area.

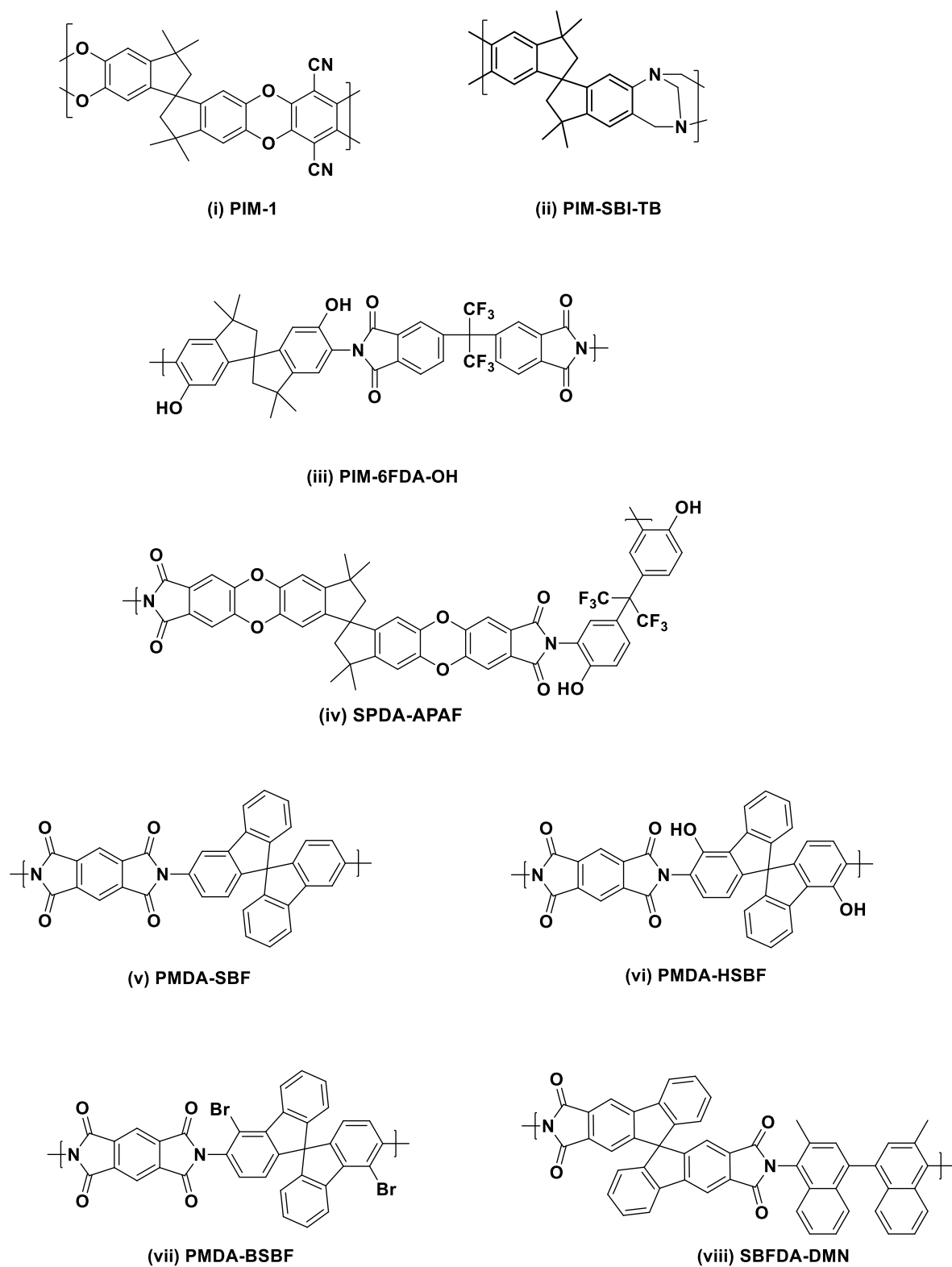


**Fig. 4.1.** Chemical structures of PIMs evaluated for ethylene/ethane separation presented in this chapter.

**Table 4.1.** Physical and thermal properties of the PIMs tested in this work.

Polymer	T <sub>d</sub> (°C)	M <sub>n</sub> x 10 <sup>-4</sup> (g mol <sup>-1</sup> )	PDI	Surface area N <sub>2</sub> BET (m <sup>2</sup> g <sup>-1</sup> )
PIM-1 <sup>a</sup>	472	6.9	2.42	780
PIM-SBI-TB	433	2.4	1.34	720
SBFDA-DMN <sup>b</sup>	520	6.5	1.92	686
PMDA-BSBF <sup>c</sup>	450	7.1	1.6	450
SPDA-APAF	461	0.92	1.04	360
PMDA-SBF <sup>c</sup>	480	9.4	1.6	320
PIM-6FDA-OH	385	8.54	1.94	186
PMDA-HSBF	413	1.44	1.22	80

<sup>a</sup> [31].<sup>b</sup> [30].<sup>c</sup> [19].

#### 4.3 Ethylene/ethane sorption isotherms at 35 °C in PIM membranes

Gravimetric sorption was used to qualitatively assess the ethylene/ethane solubility in the dense Henry mode and the immobilized Langmuir domains of the PIMs reported here. Once the steady state gas uptake was established at 35 °C for each sample, the molar uptake at each successive pressure point was used to build its corresponding sorption isotherm. As expected, the ethylene/ethane solubility selectivity in the PIMs is very close to 1; thus, there was no preferential sorption of either hydrocarbon in their polymeric matrices. The calculated dual-mode sorption parameters are shown in **Table 4.2**. Overall, the Langmuir capacity factor,  $C'_H$ , ranged from 30 cm<sup>3</sup> cm<sup>-3</sup> to 60 cm<sup>3</sup> cm<sup>-3</sup>, and it agreed with the BET surface area trend. Conversely, there was no apparent correlation between

the interaction parameter  $b$  and the structure of the polymers. Furthermore, the  $C_H$  of the PIMs tested here were comparatively higher than those of low free volume polymers [5].

**Table 4.2.** Parameters obtained from fitting experimental data to the dual-mode sorption model for the PIMs tested in this work.

Polymer	Ethylene			Ethane		
	$k_D * 10^{-2}$ ( $\text{cm}^3\text{cm}^{-3}$ $\text{cmHg}^{-1}$ )	$C'_H$ ( $\text{cm}^3$ $\text{cm}^{-3}$ )	$b * 10^{-2}$ ( $\text{cmHg}^{-1}$ )	$k_D * 10^{-2}$ ( $\text{cm}^3\text{cm}^{-3}$ $\text{cmHg}^{-1}$ )	$C'_H$ ( $\text{cm}^3$ $\text{cm}^{-3}$ )	$b * 10^{-2}$ ( $\text{cmHg}^{-1}$ )
PIM-1	3.1	58.1	1.4	3.9	56.0	1.4
PIM-SBI-TB	4.0	52.7	1.0	4.4	53.0	1.7
SBFDA-DMN	3.3	55.6	1.5	3.8	61.9	2.1
PMDA-BSBF	4.0	46.3	2.0	3.0	52.2	2.0
SPDA-APAF	2.5	30.8	1.2	2.8	28.4	1.6
PMDA-SBF	2.1	42.6	1.0	2.1	35.7	1.7
PIM-6FDA-OH	1.5	42.0	0.6	1.7	34.1	1.3
PMDA-HSBF	2.1	33.4	1.5	1.9	31.5	1.9

#### 4.4 Ethylene/ethane pure-gas transport at 35 °C and 2 bar upstream pressure in PIM membranes

The constant volume-variable pressure method was used to evaluate the pure-gas permeability through the PIMs at 2 bar upstream pressure and 35 °C. The pure-gas selectivity of ethylene/ethane through this PIM series varied from 1.7 to 5.1, as shown in **Table 4.3**. The highly open structures of PIM-SBI-TB, and SBFDA-DMN allowed for very high ethylene permeabilities of 522 Barrer and 405 Barrer respectively, however the

ethylene/ethane selectivity was low with values of less than 2. The relatively tight cavities of the hydrogen-bonded matrix of PMDA-HSBF allowed its ultramicroporosity to achieve significant diffusion selectivity. PMDA-HSBF has an ethylene permeability of 3.3 Barrer and an ethane permeability of only 0.6 Barrer; thus, translating into a pure-gas selectivity of 5.1, nearly matching that of low-free volume 6FDA-NDA [33]. On the other hand, its unfunctionalized analog, PMDA-SBF, showed an ethylene/ethane selectivity of only 3.2. Moreover, bromine-substituted PMDA-BSBF had a selectivity of 2.4 although the permeability was 4-fold higher compared to PMDA-HSBF.

**Table 4.3.** Single-gas permeation of various gases through spiro-based PIMs measured at 35 °C and 2 bar upstream pressure with vacuum downstream.

Polymer	Permeability (Barrer)						Selectivity (-)
	H <sub>2</sub>	N <sub>2</sub>	CH <sub>4</sub>	CO <sub>2</sub>	C <sub>2</sub> H <sub>4</sub>	C <sub>2</sub> H <sub>6</sub>	C <sub>2</sub> H <sub>4</sub> / C <sub>2</sub> H <sub>6</sub>
PIM-1 <sup>a</sup>	3085	434	705	6400	1631	906	1.8
PIM-SBI-TB	1816	161	291	2200	522	300	1.7
SBFDA-DMN	2134	186	264	3637	405	199	2.0
PMDA-BSBF	560	29	36.5	693	52	21	2.4
SPDA-APAF	200	7.3	6.2	160	10	2.7	3.7
PMDA-SBF	210	7.4	8.5	184	15.8	4.9	3.2
PIM-6FDA-OH <sup>b</sup>	181	5.5	3.4	119	5.5	1.4	4.0
PMDA-HSBF	122	2.0	1.5	66	3.3	0.6	5.1

<sup>a</sup> Previous work [31]

<sup>b</sup> Previous work [34].



4.5 Ethylene/ethane diffusivity and solubility coefficients at 35 °C and 2 bar upstream pressure in PIM membranes

The solubility and diffusivity coefficients of ethylene and ethane can be seen in **Table 4.4**. The separation of these small-chain hydrocarbons can be readily attributed to differences in their diffusion through the PIM porosity, since the ethylene/ethane pure-gas selectivity matched their corresponding diffusion selectivity. The solubility coefficients determined at 2 bar and 35 °C of the various PIMs ranged from 0.17 cm<sup>3</sup>(STP) cm<sup>-3</sup> cmHg<sup>-1</sup> to 0.31 cm<sup>3</sup>(STP) cm<sup>-3</sup> cmHg<sup>-1</sup>. Furthermore, a relation may be observed between the hydrocarbon solubility in the PIM and its respective BET surface area. The hydroxyl-functionalized polymers presented tighter cavities that diminished the surface area available for hydrocarbon sorption uptake. Alternatively, the highly microporous structures of SBFDA-DMN and PIM-SBI-TB adsorbed more hydrocarbons and concurrently showed two orders of magnitude higher diffusion coefficients than those of the hydroxyl-functionalized PIM-PIs: SPDA-APAF and PMDA-HSBF.

**Table 4.4.** Solubility and diffusivity of ethylene and ethane in various PIMs, measured at 35°C and 2 bar upstream pressure.

Polymer	Solubility <sup>a</sup>		$\alpha_s$	Diffusivity <sup>b</sup>		$\alpha_D$
	[cm <sup>3</sup> (STP) cm <sup>-3</sup> cmHg <sup>-1</sup> ]			10 <sup>-10</sup> * (cm <sup>2</sup> s <sup>-1</sup> )		
	Ethylene	Ethane	(-)	Ethylene	Ethane	(-)
PIM-1 <sup>c</sup>	0.29	0.31	0.93	5594.0	2896.4	1.93
PIM-SBI-TB	0.25	0.30	0.84	2102.9	1011.4	2.08
SBFDA-DMN	0.28	0.30	0.95	1433.7	666.8	2.15

PMDA-BSBF	0.19	0.19	1.03	270.5	114.1	2.37
SPDA-APAF	0.16	0.16	0.99	64.5	17.2	3.75
PMDA-SBF	0.19	0.19	1.03	81.7	25.9	3.16
PIM-6FDA-OH <sup>d</sup>	0.17	0.16	1.02	33.3	8.5	3.92
PMDA-HSBF	0.17	0.17	1.00	19.2	3.8	5.10

<sup>a</sup> Measured by gravimetric sorption

<sup>b</sup> Calculated from  $D = P S^{-1}$

<sup>c</sup> Previous work [31].

<sup>d</sup> Previous work [34].

#### 4.6 Ethylene/ethane upper bound

The ladder PIMs confirmed superior permeability coefficients compared to those of non-PIM materials, while operating under the upper bound of polymeric performance previously developed by Rungta and Koros [5] (Fig. 4.2). The strong dependence of diffusion contributions towards high ethylene/ethane selectivity makes this application a good target for membranes with much ordered and rigid porosities such as the ones found in carbon molecular sieves (CMS) [31, 34, 35]. Alternatively, PIM polymers with more rigid contortion centers (e.g. triptycene, and ethanoanthracene) in conjunction with hydroxyl functionalities and/or brominated moieties may produce the desired diffusion selectivity to surpass the current trade-off, as reported for other separation systems such as O<sub>2</sub>/N<sub>2</sub> and H<sub>2</sub>/CH<sub>4</sub> [17].

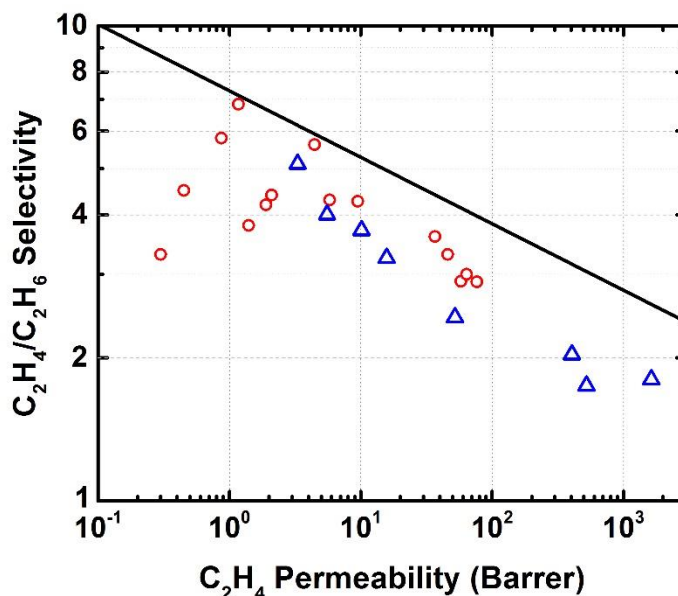


**Fig. 4.2.** Existing ethylene/ethane separation data with polymeric membranes. The red circles represent data from non-PIM glassy polyimides [5] whereas the blue triangles represent PIMs containing spiro-contortion centers.

#### 4.7 Conclusions

In this chapter the ethylene/ethane separation performance of various spiro-based PIMs was studied. The solubility separation factors,  $S_{C_2H_4/C_2H_6}$ , of the hydrocarbons in the PIM matrices were essentially 1, which indicated no preferential affinity of one molecule over the other one. The solubility of either hydrocarbon, measured at 2 bar and 35 °C, ranged from the lowest  $0.17 \text{ cm}^3(\text{STP}) \text{ cm}^{-3} \text{ cmHg}^{-1}$  in PMDA-HSBF to the highest  $0.29 \text{ cm}^3(\text{STP}) \text{ cm}^{-3} \text{ cmHg}^{-1}$  in PIM-1. The chain rigidity coupled with cavity tightness provided by –OH functionalized PIMs allowed them to sieve ethylene from ethane as well as a

standard low free volume polymer. However, all PIMs tested here were still limited by the current polymer upper bound for the ethylene/ethane system.

#### 4.8 References

- [1] W.J. Koros, Evolving beyond the thermal age of separation processes: membranes can lead the way, *AIChE Journal*, 50 (2004) 2326-2334.
- [2] T. Ren, M. Patel, K. Blok, Olefins from conventional and heavy feedstocks: energy use in steam cracking and alternative processes, *Energy*, 31 (2006) 425-451.
- [3] J.A. Caballero, I.E. Grossmann, M. Keyvani, E.S. Lenz, Design of hybrid distillation-vapor membrane separation systems, *Ind. Eng. Chem. Res.*, 48 (2009) 9151-9162.
- [4] L.M. Robeson, Correlation of separation factor versus permeability for polymeric membranes, *J. Membr. Sci.*, 62 (1991) 165-185.
- [5] M. Rungta, C. Zhang, W.J. Koros, L. Xu, Membrane-based ethylene/ethane separation: the upper bound and beyond, *AIChE Journal*, 59 (2013) 3475-3489.
- [6] K. Tanaka, A. Taguchi, J. Hao, H. Kita, K. Okamoto, Permeation and separation properties of polyimide membranes to olefins and paraffins, *J. Membr. Sci.*, 121 (1996) 197-207.
- [7] O.M. Ilinitich, G.L. Semin, M.V. Chertova, K.I. Zamaraev, Novel polymeric membranes for separation of hydrocarbons, *J. Membr. Sci.*, 66 (1992) 1-8.
- [8] S.S. Chan, R. Wang, T.-S. Chung, Y. Liu, C2 and C3 hydrocarbon separations in poly(1,5-naphthalene-2,2'-bis(3,4-phthalic) hexafluoropropane) diimide (6FDA-1,5-NDA) dense membranes, *J. Membr. Sci.*, 210 (2002) 55-64.
- [9] C. Staudt-Bickel, W.J. Koros, Olefin/paraffin gas separations with 6FDA-based polyimide membranes, *J. Membr. Sci.*, 170 (2000) 205-214.
- [10] R. Faiz, K. Li, Polymeric membranes for light olefin/paraffin separation, *Desalination*, 287 (2012) 82-97.
- [11] P.M. Budd, B.S. Ghanem, S. Makhseed, N.B. McKeown, K.J. Msayib, C.E. Tattershall, Polymers of intrinsic microporosity (PIMs): robust, solution-processable, organic nanoporous materials, *Chem. Commun.*, (2004) 230-231.
- [12] N.B. McKeown, P.M. Budd, K.J. Msayib, B.S. Ghanem, H.J. Kingston, C.E. Tattershall, S. Makhseed, K.J. Reynolds, D. Fritsch, Polymers of intrinsic microporosity (PIMs): Bridging the void between microporous and polymeric materials, *Chem. Eur. J.*, 11 (2005) 2610-2620.
- [13] P.M. Budd, N.B. McKeown, D. Fritsch, Polymers of intrinsic microporosity (PIMs): High free volume polymers for membrane applications, *Macromol. Symp.*, 245-246 (2006) 403-405.

- [14] M. Carta, R. Malpass-Evans, M. Croad, Y. Rogan, J.C. Jansen, P. Bernardo, F. Bazzarelli, N.B. McKeown, An efficient polymer molecular sieve for membrane gas separations, *Science*, 339 (2013) 303-307.
- [15] M. Carta, M. Croad, R. Malpass-Evans, J.C. Jansen, P. Bernardo, G. Clarizia, K. Friess, M. Lanč, N.B. McKeown, Triptycene induced enhancement of membrane gas selectivity for microporous Tröger's base polymers, *Adv. Mater.*, 26 (2014) 3526-3531.
- [16] B.S. Ghanem, R. Swaidan, E. Litwiller, I. Pinnau, Ultra-microporous triptycene-based polyimide membranes for high-performance gas separation, *Adv. Mater.*, 26 (2014) 3688-3692.
- [17] R. Swaidan, B. Ghanem, I. Pinnau, Fine-tuned intrinsically ultramicroporous polymers redefine the permeability/selectivity upper bounds of membrane-based air and hydrogen separations, *ACS Macro Lett.*, 4 (2015) 947-951.
- [18] R. Swaidan, M. Al-Saeedi, B. Ghanem, E. Litwiller, I. Pinnau, Rational design of intrinsically ultramicroporous polyimides containing bridgehead-substituted triptycene for highly selective and permeable gas separation membranes, *Macromolecules*, 47 (2014) 5104-5114.
- [19] X. Ma, O. Salinas, E. Litwiller, I. Pinnau, Novel spirobifluorene- and dibromospirobifluorene-based polyimides of intrinsic microporosity for gas separation applications, *Macromolecules*, 46 (2013) 9618-9624.
- [20] R. Swaidan, B.S. Ghanem, E. Litwiller, I. Pinnau, Pure- and mixed-gas CO<sub>2</sub>/CH<sub>4</sub> separation properties of PIM-1 and an amidoxime-functionalized PIM-1, *J. Membr. Sci.*, 457 (2014) 95-102.
- [21] N. Du, G.P. Robertson, J. Song, I. Pinnau, M.D. Guiver, High-performance carboxylated polymers of intrinsic microporosity (PIMs) with tunable gas transport properties, *Macromolecules*, 42 (2009) 6038-6043.
- [22] N. Du, H.B. Park, G.P. Robertson, M.M. Dal-Cin, T. Visser, L. Scoles, M.D. Guiver, Polymer nanosieve membranes for CO<sub>2</sub>-capture applications, *Nat. Mater.*, 10 (2011) 372-375.
- [23] J. Weber, N. Du, M.D. Guiver, Influence of intermolecular interactions on the observable porosity in intrinsically microporous polymers, *Macromolecules*, 44 (2011) 1763-1767.
- [24] R.J. Swaidan, B. Ghanem, R. Swaidan, E. Litwiller, I. Pinnau, Pure- and mixed-gas propylene/propane permeation properties of spiro- and triptycene-based microporous polyimides, *J. Membr. Sci.*, 492 (2015) 116-122.
- [25] S. Yi, X. Ma, I. Pinnau, W.J. Koros, A high-performance hydroxyl-functionalized polymer of intrinsic microporosity for an environmentally attractive membrane-based approach to decontamination of sour natural gas, *J. Mater. Chem. A*, (2015).

- [26] P. Li, T.S. Chung, D.R. Paul, Gas sorption and permeation in PIM-1, *J. Membr. Sci.*, 432 (2013) 50-57.
- [27] N. Du, J. Song, G.P. Robertson, I. Pinnau, M.D. Guiver, Linear high molecular weight ladder polymer via fast polycondensation of 5,5',6,6'-tetrahydroxy-3,3,3',3'-tetramethylspirobisindane with 1,4-dicyanotetrafluorobenzene, *Macromol. Rapid Commun.*, 29 (2008) 783-788.
- [28] X. Ma, R. Swaidan, Y. Belmabkhout, Y. Zhu, E. Litwiller, M. Jouiad, I. Pinnau, Y. Han, Synthesis and gas transport properties of hydroxyl-functionalized polyimides with intrinsic microporosity, *Macromolecules*, 45 (2012) 3841-3849.
- [29] H. Shamsipur, B.A. Dawood, P.M. Budd, P. Bernardo, G. Clarizia, J.C. Jansen, Thermally rearrangeable pim-polyimides for gas separation membranes, *Macromolecules*, 47 (2014) 5595-5606.
- [30] X. Ma, B. Ghanem, O. Salinas, E. Litwiller, I. Pinnau, Synthesis and effect of physical aging on gas transport properties of a microporous polyimide derived from a novel spirobifluorene-based dianhydride, *ACS Macro Lett.*, 4 (2015) 231-235.
- [31] O. Salinas, X. Ma, E. Litwiller, I. Pinnau, Ethylene/ethane permeation, diffusion and gas sorption properties of carbon molecular sieve membranes derived from the prototype ladder polymer of intrinsic microporosity (PIM-1), *J. Membr. Sci.*, 504 (2016) 133-140.
- [32] X. Ma, O. Salinas, E. Litwiller, I. Pinnau, Pristine and thermally-rearranged gas separation membranes from novel o-hydroxyl-functionalized spirobifluorene-based polyimides, *Polymer Chemistry*, 5 (2014) 6914-6922.
- [33] S.S. Chan, T.-S. Chung, Y. Liu, R. Wang, Gas and hydrocarbon (C2 and C3) transport properties of co-polyimides synthesized from 6FDA and 1,5-NDA (naphthalene)/Durene diamines, *J. Membr. Sci.*, 218 (2003) 235-245.
- [34] O. Salinas, X. Ma, E. Litwiller, I. Pinnau, High-performance carbon molecular sieve membranes for ethylene/ethane separation derived from an intrinsically microporous polyimide, *J. Membr. Sci.*, 500 (2016) 115-123.
- [35] M. Rungta, L. Xu, W.J. Koros, Carbon molecular sieve dense film membranes derived from Matrimid® for ethylene/ethane separation, *Carbon*, 50 (2012) 1488-1502.

## Chapter 5

### **Ethylene/Ethane Permeation, Diffusion and Gas Sorption Properties of Carbon Molecular Sieve Membranes Derived from the Prototype Ladder Polymer of Intrinsic Microporosity (PIM-1)<sup>1</sup>**

Fine-tuning the microporosity of PIM-1 by heat treatment was applied to develop a suitable carbon molecular sieve membrane for ethylene/ethane separation. Pristine PIM-1 films were heated from 400 to 800 °C under inert N<sub>2</sub> atmosphere (< 2 ppm O<sub>2</sub>). At 400 °C, PIM-1 self-cross-linked and developed polar carbonyl and hydroxyl groups due to partial dioxane splitting in the polymer backbone. Significant degradation occurred at 600 °C due to carbonization of PIM-1 and resulted in 30% increase in cumulative surface area compared to its physically cross-linked predecessor. In addition, PIM-1-based CMS developed smaller ultramicropores with increasing pyrolysis temperature, which enhanced their molecular sieving capability by restricted diffusion of ethylene and ethane through the matrix due to microstructural carbon densification. Consequently, the pure-gas ethylene permeability (measured at 35 °C and 2 bar) decreased from 1600 Barrer for the pristine PIM-1 to 1.3 Barrer for the amorphous carbon generated at 800 °C, whereas the ethylene/ethane pure-gas selectivity increased significantly from 1.8 to 13.

---

<sup>1</sup>adapted from:

O. Salinas, X. Ma, E. Litwiller, I. Pinnau, J. Membr. Sci., 504 (2016) 133-140.



## 5.1 Introduction

Ethylene/ethane separation is accomplished through equilibrium-based energy-intensive distillation processes [1]. Alternatively, membrane technology could offer substantial savings to this application [2] because membranes do not require a phase change for the separation of the feed components. In recent years, gas separation with membranes has successfully found large-scale commercial use for natural gas upgrading and nitrogen production from air [3, 4]. To date, however, polymer membranes have not reached the minimum requirements for viable ethylene/ethane separation due to: i) insufficient selectivity (e.g. ~3-6 under ideal pure-gas permeation conditions) and low permeability [5-10] and ii) potential penetrant-induced plasticization leading to reduced mixed-gas selectivity [9]. The former issue can be addressed by rational design of the pore size and pore distribution (PSD) of the membrane material, while the latter demands materials that can withstand the high activities of the ethylene/ethane feed under realistic industrial conditions.

Intrinsically microporous polymers (PIMs) represent the state-of-the-art among known solution-processable organic membrane materials for gas separation [11-16]. PIMs often define the permeability/selectivity performance upper bounds of gas transport through polymers [17] as defined by Robeson [18, 19] by virtue of their contorted and rigid polymer backbones that allow them to capitalize on interconnected pore sizes of less than 2 nm [20, 21]. The prototype of the PIM-family, PIM-1, was synthesized by polycondensation reaction of 5,5',6,6'-tetrahydroxy-3,3,3',3'-tetramethyl-1,1'-spirobisindane and tetrafluoroterephthalonitrile. The polymer structure is shown in **Fig. 5.1**. The tetrahedral-spirobisindane moiety in its backbone that promotes inefficient packing of

its chains in the solid state [12, 20, 22]. Although the gas separation performance of PIM-1 has been placed on the upper bounds for several gas pairs, such as O<sub>2</sub>/N<sub>2</sub> and H<sub>2</sub>/CH<sub>4</sub>, it is an inadequate material for ethylene/ethane separation with a high ethylene permeability of 573 Barrer but a very low ethylene/ethane selectivity of only 1.4 (measured at 25 °C and 1 atm) [23].

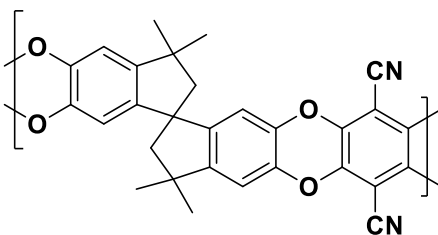


**Fig. 5.1.** Chemical structure of PIM-1.

To achieve higher selectivity, the PSD in PIMs can be tailored by chemical and/or thermal means to potentially improve their gas separation properties. One possibility simply requires the post-synthesis addition of functionalities to the polymer matrix to increase its inter- and intra-chain-interactions [24], which leads to enhanced densification of the polymer micropore structure. For example, the nitrile groups in PIM-1 can be substituted with polar moieties, such as carboxyl, amidoxime, thioamide or tetrazole, to enhance its permselectivity [24-27]. Another relevant approach to densify the PSD of PIM-1 via thermal annealing [28-32] or by further heat treatment so that specific chain degradation reactions are triggered. For example, PIM-1 self-cross-linked under vacuum at 300 °C and shown a 400% increase in CO<sub>2</sub>/CH<sub>4</sub> pure-gas selectivity, reportedly via triazine formation [33]. A different mechanism was proposed in a subsequent study [34], where it was reported that O<sub>2</sub> was responsible of covalently bridging the PIM-1 chains starting around 300 °C. Fine-tuning of the microporosity in PIM-1 was performed by varying the

O<sub>2</sub> content in the heating atmosphere (< 200 ppm) available prior to the onset of the polymer backbone decomposition (i.e. < 450 °C).

Pyrolysis of a polymer beyond its initial decomposition temperature under essentially inert conditions produces carbon molecular sieve (CMS) membranes, which can display outstanding gas separation performance [35]. CMS have strongly size-sieving PSDs by virtue of their large array of ultramicropores (i.e. < 0.7 nm) [36], which are instrumental in distinguishing permeants based on the small differences of their molecular dimensions [37]. Furthermore, CMS membranes may be stable under harsh hydrocarbon saturated atmospheres, as demonstrated in previous studies [38, 39]. However, in spite of their promising properties, only a few studies of CMS membranes have been reported for ethylene/ethane separation [38, 40-45].

The CMS separation performance is controlled by a wide variety of parameters involved in the pyrolysis process. For example, the heating protocol [46-48] and the atmospheric composition [43, 49-51] may lead to distinctly different microstructures in the CMS membranes are also influenced by several polymer precursor determined properties: i) pendant groups [52, 53], ii) glass transition temperature [54], and iii) free volume [53, 55, 56]. PIM-1 represents an extreme case in all of these categories as it possesses polar cyanide groups, undetectable glass transition temperature and, at the same time, it is one of the most permeable glassy polymers known to date do to its high free volume [57]. To the best of our knowledge, there is no rigorous assessment available for the gas transport properties of CMS membranes generated from the spirobisindane-ladder prototype PIM-1. Here, ethylene and ethane sorption, diffusion and permeation data are reported for the first

time in partially and fully carbonized membranes derived via thermal treatment from pristine PIM-1 films.

## 5.2 Thermal annealing and CMS formation of pristine PIM-1 films

The pure-gas H<sub>2</sub>, N<sub>2</sub>, O<sub>2</sub>, CH<sub>4</sub> and CO<sub>2</sub> permeation properties of methanol-exchanged PIM-1 films, followed by thermal annealing at 250 °C for 24 h under vacuum, and previously reported data for PIM-1 films made under a variety of conditions are shown in **Table 5.1**. The significant variance in the permeation properties of PIM-1 found in the literature can mainly be attributed to the casting solvent type, solvent exchange procedure as well as annealing temperature selected for removal of solvent traces from the film [21,23,63]. In all cases PIM-1 exhibited very high gas permeability with low-to moderate gas selectivity.

The thermal decomposition mechanisms of PIM-1 under inert nitrogen atmosphere (i.e. O<sub>2</sub> concentration < 2 ppm) where characterized by the evolution of specific gaseous products (**Fig. 5.2**).

**Table 5.1.** Permeation data of PIM-1 prepared under different protocols.

Drying temperature (°C)	Permeability					$\alpha_{x/y}$	
	H <sub>2</sub>	N <sub>2</sub>	O <sub>2</sub>	CH <sub>4</sub>	CO <sub>2</sub>	O <sub>2</sub> /N <sub>2</sub>	CO <sub>2</sub> /CH <sub>4</sub>
250 <sup>a</sup>	3085	434	1220	705	6400	2.8	9.2
(NA) <sup>b</sup>	1300	92	370	125	2300	4.0	18.4
80 <sup>c</sup>	2936	252	969	320	5303	3.8	16.5

<sup>a</sup> This work; films were cast from THF, methanol soaked, dried, and then tested at 35 °C

<sup>b</sup> Previous work; film was cast from THF and then tested at 30 °C [21]

<sup>c</sup> Previous work; film was cast from CHCl<sub>3</sub>, dried and then tested at 25 °C [23]

<sup>d</sup> 1 Barrer = 10<sup>-10</sup> cm<sup>3</sup> (STP) cm cm<sup>-2</sup> s<sup>-1</sup> cmHg<sup>-1</sup> or 7.5 × 10<sup>-18</sup> m<sup>3</sup> (STP) m m<sup>-2</sup> s<sup>-1</sup> Pa<sup>-1</sup>

Heat treatment of PIM-1 at 400 °C for 30 min caused only 1% weight loss which was related to CO<sub>2</sub> evolution from the partial thermolysis of its dioxane rings as was proposed by Song et al. [34]. Evidence of the splitting of the dioxane-ether linkage is shown in the FTIR spectra of the samples (**Fig. 5.3a**). The ether linkage (1110 cm<sup>-1</sup>) decreased in intensity, whereas the -OH stretch (3400 cm<sup>-1</sup>) and the C=O (1700 cm<sup>-1</sup>) increased significantly. In addition, the pristine fluorescent yellow PIM-1 films became brown after heat treatment at 400 °C and became partially insoluble in THF. Thermal treatment of PIM-1 at 400 °C for 30 min under < 2 ppm O<sub>2</sub> atmospheres effectively created an insoluble, cross-linked intermediate system with enhanced intra-chain interactions by virtue of the hydrogen bonding between the created polar hydroxyl groups and the other polar segments of the chain; in a similar fashion to other hydrogen-bonded-PIM-1 examples [24-27].

PIM-1 samples treated above 600 °C resulted in degradation of the cross-linked chains as shown by the peaks in evolution of both H<sub>2</sub>O and CO<sub>2</sub> during the degradation process (**Fig. 5.2**). During this thermal step, the initial weight decreased by ~26%, leading to the formation of amorphous carbon as revealed by the loss of functionalities in their FTIR spectra (**Fig. 5.3b**). In addition, a rise in Raman activity of the D and G peaks (1300 cm<sup>-1</sup> and 1600 cm<sup>-1</sup> respectively) (**Fig. 5.4**) confirmed the content of amorphous graphene in the carbon network [58]. It can be hypothesized that the ratio of intensities between the D and G peaks tend to reflect a maximum value as the matrix reconfigured at higher degradation temperatures into more ordered carbon sieves [59]. Furthermore,

complimentary XRD analysis supported the strong collapse in porosity towards CMS (**Fig. 5.5**). The broad trimodal XRD spectra of pristine and partially degraded PIM-1 ( $\sim 3.74 - 7$  Å) sintered into amorphous carbon configurations with average d-spacing  $< 3.8$  Å. The characteristic (1 0 0) graphene plane was associated to the 2.05 Å peak displayed in the spectrum of the carbon pyrolyzed at 800 °C [60]. Increased ultramicroporosity occurred simultaneously due to dehydrogenation of the carbon matrix which was related to  $< 1\%$  weight loss from 700 to 800 °C.

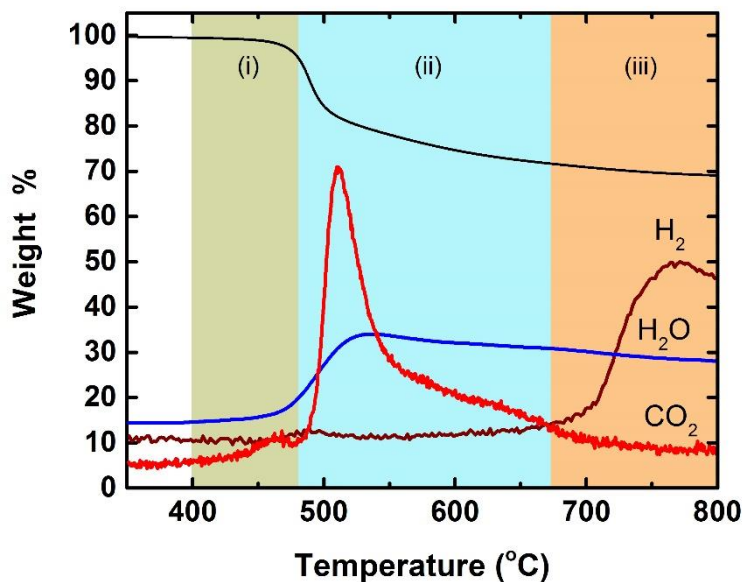


**Fig. 5.2.** Thermal gravimetric analysis of PIM-1 under an inert N<sub>2</sub> atmosphere at a ramping rate of 3 °C/min. Mass-spectrometry qualitatively depicts H<sub>2</sub>, H<sub>2</sub>O and CO<sub>2</sub> evolution. Shaded areas represent the dominating degradation mechanisms: (i) partial dioxane splitting, ii) complete dioxane and methyl groups degradation, iii) matrix dehydrogenation.

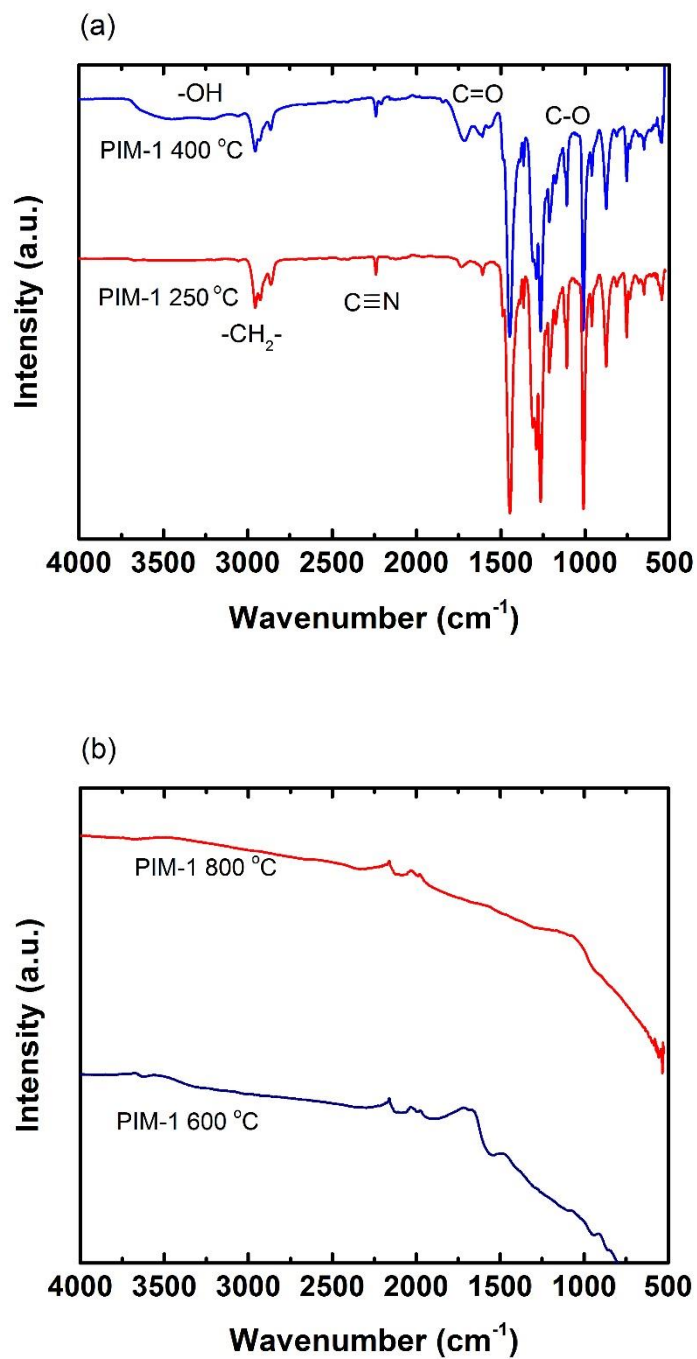


**Fig. 5.3.** FTIR spectra of (a) polymeric heated-annealed PIM-1 and (b) its CMS derivatives.

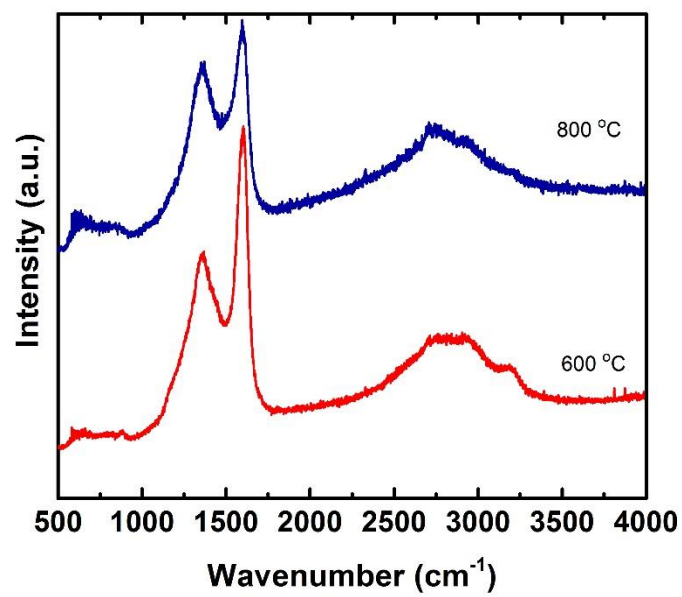


**Fig. 5.4.** Raman spectra of CMS generated from PIM-1 at 600 and 800 °C.



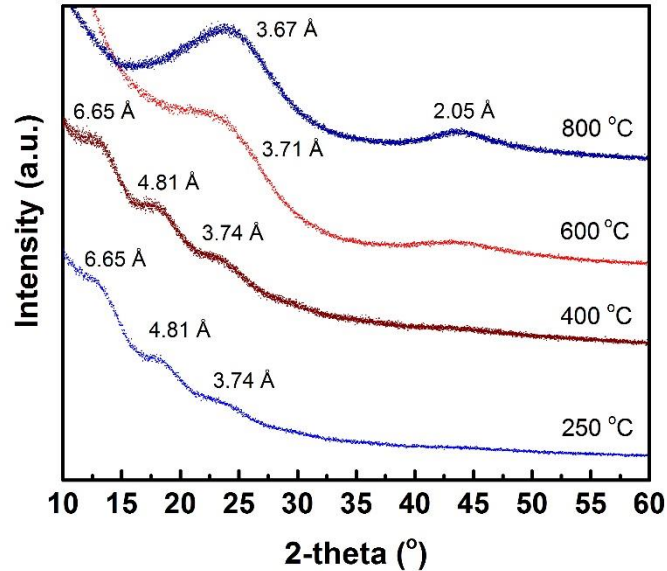
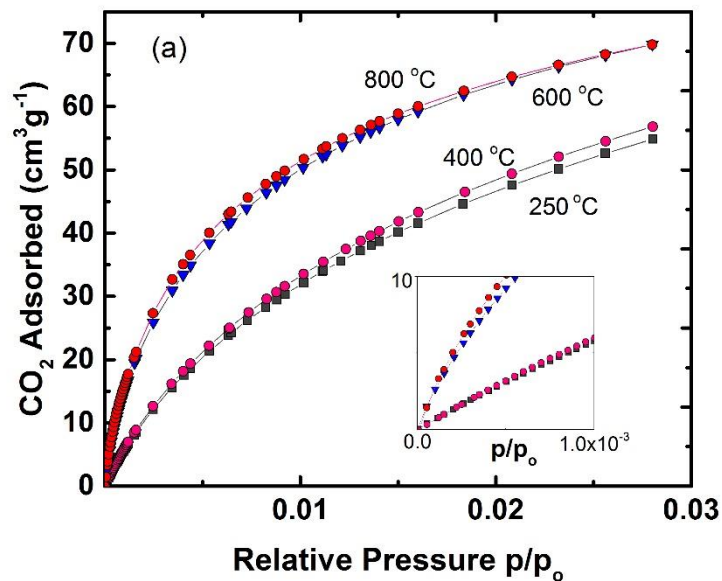


**Fig. 5.5.** XRD spectra of PIM-1 (250 °C) and cross-linked (400 °C) PIM-1 and its heat-derived CMS analogs (600 and 800 °C).

### 5.3 Surface area and PSD estimation of PIM-1 and its heat-derived CMS

NLDFT applied to CO<sub>2</sub> sorption data obtained at 0 °C can be used to use to *qualitatively* assess the PSD of a microporous membrane material [61]. CO<sub>2</sub> sorption in PIM-1 and its CMS counterparts (**Fig. 5.6a**) showed a very steep linear increase in concentration at small relative pressures (i.e.  $p/p_0 < 10^{-3}$ ), a common characteristic found in other microporous materials [62]. Interestingly, the CO<sub>2</sub>-NLDFT method confirmed that the pores of <0.7 nm found in pristine PIM/1 contribute to a large fraction of its total surface area, if compared to the bet surface area for the whole pore range determined with N<sub>2</sub> sorption at – 196 C° [25,68]. Furthermore, carbonization of the cross-linked PIM-1 yielded a significant rise of a bimodal ultramicroporous distribution (**Fig. 5.6b**). In addition, the surface area of PIM-1 carbonized

at 800 °C increased by 30% compared to the cross-linked precursor produced at 400 °C (Table 5.2), from 530 m<sup>2</sup>/g to 700 m<sup>2</sup>/g. Likewise to other CMS reported in the literature [53], PIM-1-derived carbons had higher densities than their precursor polymers as shown in Table 5.2



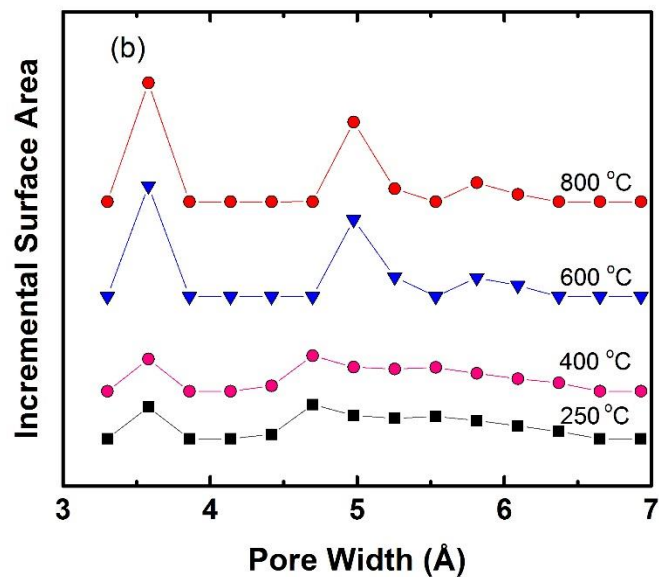


**Fig. 5.6.** (a) CO<sub>2</sub> sorption isotherms at 0 °C in heated-annealed PIM-1 (250 and 400 °C) and its CMS derivatives (600 and 800 °C). The lower right corner depicts low-pressure sorption. (b) Pore size distribution computed from this sorption data by NLDFT using Micromeritics software version 2.0.

**Table 5.2.** Bulk density and internal surface area of PIM-1 and its CMS derivatives.

Treatment Temperature (°C)	Bulk density <sup>a</sup> (g cm <sup>-3</sup> )	Cumulative <sup>b</sup> NLDFT CO <sub>2</sub> surface area (m <sup>2</sup> g <sup>-1</sup> )
250	1.04±0.01	513
400	1.03±0.01	531
600	1.39±0.01	690
800	1.43±0.01	700

<sup>a</sup> Measured gravimetrically,  $\rho = (\text{weight of sample}) (\text{volume})^{-1}$ .

<sup>b</sup> Total surface area of pores smaller than 7.2 Å according to the NLDFT method.

#### 5.4 *Pure-gas sorption isotherms of ethylene and ethane in PIM-1 and its heat-derived CMS analogs*

Sorption of ethylene and ethane at 35 °C was determined gravimetrically (**Fig. 5.7a**). As expected from the qualitative PSD description based on the XRD and NLDFT studies discussed above, cross-linked PIM-1 at 400 °C did not change the ethylene uptake due to its very slight variations in its PSD distribution before and after the partial dioxane degradations at 400 °C. Sorption in the carbonized samples derived from PIM-1 showed Langmuir-like behavior, with ~100% increase in the sorption capacity of ethylene at 1 bar, from 32 cm<sup>3</sup>(STP) cm<sup>-3</sup> in PIM-1 to 64 cm<sup>3</sup>(STP) cm<sup>-3</sup> in the 800°C-derived CMS. Remarkably, the total ethylene uptake at 15 bar in the polymeric PIM-1 samples surpassed the uptake of the CMS generated at 600 °C due to sintering of the CMS-micropores >0.7 nm during the pyrolysis procedure. Furthermore, solubility selectivity increased by ~30%, from its value of 0.95 in pristine PIM-1 to 1.25, for CMS carbonized at 800 °C (**Fig. 5.7b**). Possible  $\pi$ - $\pi$  interaction between ethylene and the walls of the amorphous carbon sheets could have caused this preferential sorption, as has been proposed elsewhere [45].

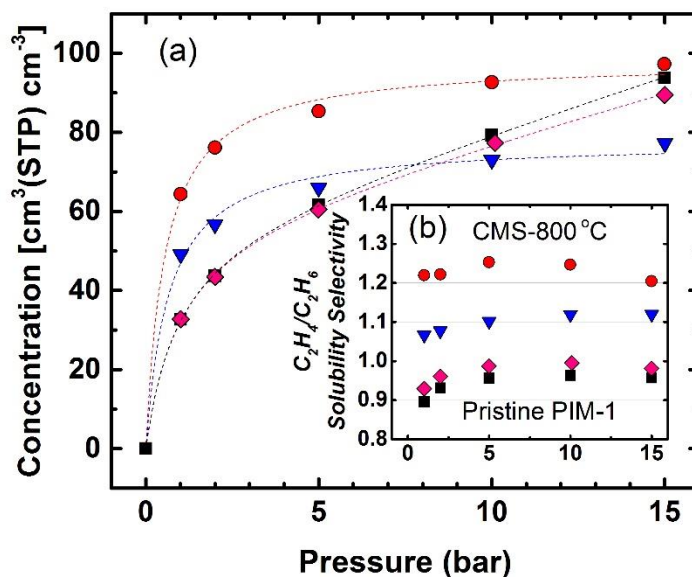


**Fig. 5.7.** (a) Pure-gas sorption isotherms of ethylene at 35 °C in pristine PIM-1-250 °C (■), its cross-linked PIM-1-400 °C derivative (◆), CMS-600 °C (▼) and CMS-800 °C (●) derivatives. Fitted dashed curves follow the dual-mode sorption model for the polymeric PIM-1 and its cross-linked analog samples, whereas the Langmuir model was used to describe sorption in the CMS. (b) Ethylene/ethane solubility selectivity as a function of pressure for all samples.

The parameters of the fitted sorption models are summarized in **Table 4.2**. The overall trend indicated an increase of  $C'_H$  and  $b$  with increasing treatment temperature. For example, ethylene  $C'_H$  of the 800 °C-treated PIM-1 sample had a value of 98 cm<sup>3</sup>(STP) cm<sup>-3</sup>, around 70% higher than the of the original PIM-1 precursor thermally annealed at 250 °C for 24 h. This result was consistent with the CO<sub>2</sub>-based NLDFT surface area data of heat-treated PIM-1 derivatives reported in the previous section of this work.

**Table 5.3.** Parameters obtained from fitting experimental ethylene and ethane sorption data to the dual-mode (polymers) and the Langmuir isotherms (carbons).

Treatment	Gas	$K_D * 10^{-2} (\text{cm}^3 \text{cm}^{-3} \text{cmHg}^{-1})$	$C'_H (\text{cm}^3 \text{cm}^{-3})$	$b * 10^{-2} (\text{cmHg}^{-1})$
Temperature				
250	Ethane	3.9	56.0	1.4
400		3.4	55.2	1.4
600			67.8	2.5
800			79.7	2.4
250	Ethylene	3.1	58.1	1.4
400		3.6	56.8	1.4
600			78.2	2.0
800			98.1	2.4

### 5.5 Pure- gas ethylene/ethane permeation properties

The ethylene/ethane permeation properties of heat-treated PIM-1 and its CMS samples are presented in **Table 5.4**. Additional gas permeation data of heat-treated PIM-1 and its CMS derivatives for H<sub>2</sub>, N<sub>2</sub>, O<sub>2</sub>, CH<sub>4</sub>, and CO<sub>2</sub> are listed in Appendix of this work. The permeability and diffusivity coefficients of ethylene and ethane decreased with increasing treatment temperature of the membrane. The pristine PIM-1 showed poor performance for ethylene/ethane separation with an ethylene permeability of 1640 Barrer and a selectivity of only 1.8. Nevertheless, in the beginning of the thermal treatment, formation of crosslinks at 400 °C increase selectivity to 2.4 with a concurrent reduction in the permeability of ethylene by 60% and of ethane by 200%. At 2 bar, there was no significant difference between the solubility coefficients of the pristine PIM-1 and its cross-linked analog (400 °C). Therefore, the drop in permeability can be attributed primarily to

a decrease in diffusion coefficients. Degradation of the cross-linked PIM-1 into the CMS membrane at 600 °C, caused a ~60% increase in solubility of both hydrocarbons in the membranes at 2 bar due to the creation of ultramicroporous voids. A significant drop occurred for the CMS membranes generated at 600 and 800 °C in the ethylene permeability from 44 and 1.3 Barrer, respectively. In a similar fashion, the diffusion coefficient of ethylene decreased 2000-fold from its original value of  $5.6 \times 10^{-7} \text{ cm}^2 \text{ s}^{-1}$  in pristine PIM-1 to its minimum value of  $2.6 \times 10^{-10} \text{ cm}^2 \text{ s}^{-1}$  in the CMS produced at 800 °C. The decrease in diffusion coefficients coupled with enhanced diffusion selectivities was a clear effect of the sintering of the dimensions of the ultramicropores in the CMS as suggested by the XRD and NLDFT results.

**Table 5.4.** Pure-gas permeability, diffusivity and solubility coefficients of ethylene and ethane at 35 °C and 2 bar for heat-treated PIM-1 and its CMS derivate samples.

Treatment temperature (°C)	Permeability, (Barrer)		Solubility <sup>a</sup> (cm <sup>3</sup> cm <sup>-3</sup> cmHg <sup>-1</sup> )		Diffusivity <sup>b</sup> *10 <sup>-10</sup> (cm <sup>2</sup> s <sup>-1</sup> )	
	Ethylene	Ethane	Ethylene	Ethane	Ethylene	Ethane
	250	1641	906	0.29	0.31	5600
400	1082	439	0.28	0.30	3900	1500
600	44	7	0.38	0.35	116	20
800	1.3	0.1	0.51	0.42	2.6	0.24

<sup>a</sup> Solubility calculated from the gravimetric sorption uptake at 2 bar

<sup>b</sup> Average diffusion coefficient calculated from  $D = P S^{-1}$

The ethylene/ethane separation performance of heat-treated PIM-1 and its CMS derivatives is compared against existing polymer and other CMS membranes in **Fig. 5.8**. The polymeric PIM-1 and its physically-cross-linked analog did not present high enough

selectivity to transcend the upper bound of the polymeric performance, whereas the carbonized PIM-1 samples exhibited selectivities very close to the previously reported values of carbons generated from Matrimid®, a low-free-volume polyimide. Interestingly, PIM-1 treated at 600 °C produced carbon membranes with moderate ethylene/ethane selectivities (i.e. 6 - 8) that match those generated from other polymeric precursors with clear structural differences (e.g. lower free volume and measureable  $T_g$ ). It is interesting to note, however, that high-temperature pyrolysis (800 °C) of the intrinsically microporous PIM-1 showed about 10-fold higher ethylene permeability compared to low-free-volume Matrimid® polyimide. This result indicates that intrinsically microporous polymers, such as PIM-1, may provide a new platform as precursors for the generation of more permeable and highly selective CMS membranes. However, to further support this preliminary conclusion drawn from this work, additional studies with structurally different PIMs are required. In addition, to assess the full potential of PIM-derived CMS membranes, future studies require high-pressure mixed ethylene/ethane permeation experiments, as previously demonstrated for a hydroxyl-functionalized PIM-PI precursor CMS membrane [69].



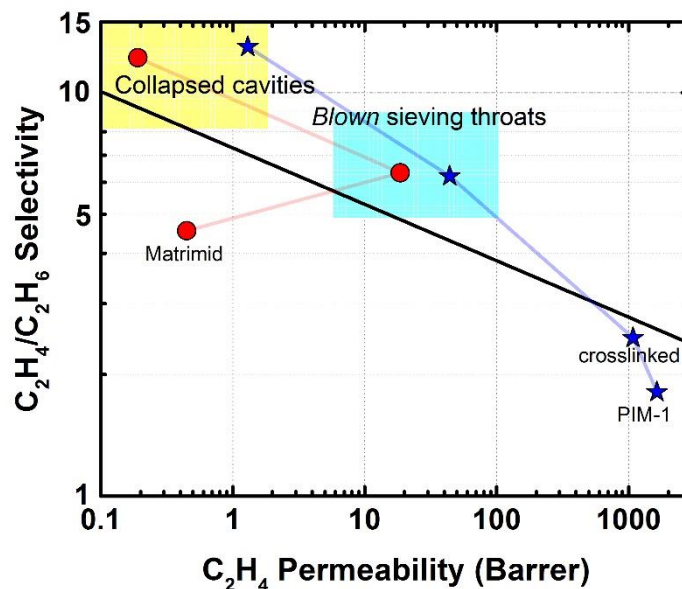


**Fig. 5.8.** Pure-gas ethylene/ethane permeation properties of heat-derived PIM-1 membranes (stars) from right to left: Pristine thermally annealed at 250 °C, cross-linked at 400 °C followed by CMS produced at 600 °C and 800 °C, respectively. For comparison, previously reported Matrimid® polyimide derived CMS heated to 550 and 800 °C [45]. Shaded areas represent the two main mechanism of carbon tailoring. The polymer upper bound is represented with the bold black line [5].

## 5.6 Conclusions

PIM-1 was heat-treated under inert N<sub>2</sub> atmosphere to provide materials with enhanced performance for ethylene/ethane separation and to provide insight about the pore evolution mechanism during carbon formation derived from intrinsically microporous

polymer precursors. The pristine dense films of PIM-1 were thermally treated at 400 °C to form a cross-linked structure which exhibited 36% increase in pure-gas ethylene-ethane selectivity from 1.8 to 2.4 with respect to its pristine precursor. Carbonization of the films at 600 °C enhanced the sorption capacity of both ethylene and ethane at lower pressures, as observed from the Langmuir behavior in their sorption isotherms measured at 35 °C. Sintering in the microporous region  $>0.7$  of the amorphous carbon membranes derived from PIM-1 prevented additional sorption of hydrocarbons at high pressures compared to their polymeric precursors. XRD and NLDFT were used to qualitatively confirm the growth in the ultramicroporous distribution found in the isotropic carbon films. The diffusion of ethylene decreased by 2000-fold as the pristine PIM-1 samples sintered into their final 800 °C-carbonaceous form, from  $5.6 \times 10^{-7} \text{ cm}^2 \text{ s}^{-1}$  to  $2.6 \times 10^{-10} \text{ cm}^2 \text{ s}^{-1}$ , while ethane decreased 12000-fold, from  $2.9 \times 10^{-7} \text{ cm}^2 \text{ s}^{-1}$  to  $2.4 \times 10^{-11} \text{ cm}^2 \text{ s}^{-1}$ ; therefore, confirming the strong molecular sieving improvement after shrinkage of the PSD closer to the molecular dimensions of ethylene and ethane.

## 5.7 References

- [1] T. Ren, M. Patel, K. Blok, Olefins from conventional and heavy feedstocks: energy use in steam cracking and alternative processes, *Energy*, 31 (2006) 425-451.
- [2] J.A. Caballero, I.E. Grossmann, M. Keyvani, E.S. Lenz, Design of hybrid distillation-vapor membrane separation systems, *Ind. Eng. Chem. Res.*, 48 (2009) 9151-9162.
- [3] R.W. Baker, *Membrane technology and applications*, John Wiley & Sons, West Sussex, 2004.
- [4] R.W. Baker, B.T. Low, Gas separation membrane materials: a perspective, *Macromolecules*, 47 (2014) 6999-7013.
- [5] M. Rungta, C. Zhang, W.J. Koros, L. Xu, Membrane-based ethylene/ethane separation: the upper bound and beyond, *AIChE Journal*, 59 (2013) 3475-3489.
- [6] K. Tanaka, A. Taguchi, J. Hao, H. Kita, K. Okamoto, Permeation and separation properties of polyimide membranes to olefins and paraffins, *J. Membr. Sci.*, 121 (1996) 197-207.
- [7] O.M. Ilinitich, G.L. Semin, M.V. Chertova, K.I. Zamaraev, Novel polymeric membranes for separation of hydrocarbons, *J. Membr. Sci.*, 66 (1992) 1-8.
- [8] S.S. Chan, R. Wang, T.-S. Chung, Y. Liu, C2 and C3 hydrocarbon separations in poly(1,5-naphthalene-2,2'-bis(3,4-phthalic) hexafluoropropane) diimide (6FDA-1,5-NDA) dense membranes, *J. Membr. Sci.*, 210 (2002) 55-64.
- [9] C. Staudt-Bickel, W.J. Koros, Olefin/paraffin gas separations with 6FDA-based polyimide membranes, *J. Membr. Sci.*, 170 (2000) 205-214.
- [10] R. Faiz, K. Li, Polymeric membranes for light olefin/paraffin separation, *Desalination*, 287 (2012) 82-97.
- [11] B.S. Ghanem, R. Swaidan, E. Litwiller, I. Pinnau, Ultra-microporous triptycene-based polyimide membranes for high-performance gas separation, *Adv. Mater.*, 26 (2014) 3688-3692.
- [12] N.B. McKeown, P.M. Budd, K.J. Msayib, B.S. Ghanem, H.J. Kingston, C.E. Tattershall, S. Makhseed, K.J. Reynolds, D. Fritsch, Polymers of intrinsic microporosity (PIMs): bridging the void between microporous and polymeric materials, *Chem. Eur. J.*, 11 (2005) 2610-2620.
- [13] R. Swaidan, M. Al-Saedi, B. Ghanem, E. Litwiller, I. Pinnau, Rational design of intrinsically ultramicroporous polyimides containing bridgehead-substituted triptycene for highly selective and permeable gas separation membranes, *Macromolecules*, 47 (2014) 5104-5114.

- [14] M. Carta, M. Croad, R. Malpass-Evans, J.C. Jansen, P. Bernardo, G. Clarizia, K. Friess, M. Lanč, N.B. McKeown, Triptycene induced enhancement of membrane gas selectivity for microporous Tröger's base polymers, *Adv. Mater.*, 26 (2014) 3526-3531.
- [15] Y. Zhuang, J.G. Seong, Y.S. Do, H.J. Jo, Z. Cui, J. Lee, Y.M. Lee, M.D. Guiver, Intrinsically microporous soluble polyimides incorporating Tröger's base for membrane gas separation, *Macromolecules*, 47 (2014) 3254-3262.
- [16] B.S. Ghanem, N.B. McKeown, P.M. Budd, N.M. Al-Harbi, D. Fritsch, K. Heinrich, L. Starannikova, A. Tokarev, Y. Yampolskii, Synthesis, characterization, and gas permeation properties of a novel group of polymers with intrinsic microporosity: PIM-polyimides, *Macromolecules*, 42 (2009) 7881-7888.
- [17] R. Swaidan, B. Ghanem, I. Pinnau, Fine-tuned intrinsically ultramicroporous polymers redefine the permeability/selectivity upper bounds of membrane-based air and hydrogen separations, *ACS Macro Lett.*, 4 (2015) 947-951.
- [18] L.M. Robeson, Correlation of separation factor versus permeability for polymeric membranes, *J. Membr. Sci.*, 62 (1991) 165-185.
- [19] L.M. Robeson, The upper bound revisited, *J. Membr. Sci.*, 320 (2008) 390-400.
- [20] P.M. Budd, B.S. Ghanem, S. Makhseed, N.B. McKeown, K.J. Msayib, C.E. Tattershall, Polymers of intrinsic microporosity (PIMs): robust, solution-processable, organic nanoporous materials, *Chem. Commun.*, (2004) 230-231.
- [21] P.M. Budd, K.J. Msayib, C.E. Tattershall, B.S. Ghanem, K.J. Reynolds, N.B. McKeown, D. Fritsch, Gas separation membranes from polymers of intrinsic microporosity, *J. Membr. Sci.*, 251 (2005) 263-269.
- [22] P.M. Budd, N.B. McKeown, D. Fritsch, Polymers of intrinsic microporosity (PIMs): High free volume polymers for membrane applications, *Macromol. Symp.*, 245-246 (2006) 403-405.
- [23] P. Li, T.S. Chung, D.R. Paul, Gas sorption and permeation in PIM-1, *J. Membr. Sci.*, 432 (2013) 50-57.
- [24] N. Du, G.P. Robertson, J. Song, I. Pinnau, M.D. Guiver, High-performance carboxylated polymers of intrinsic microporosity (PIMs) with tunable gas transport properties, *Macromolecules*, 42 (2009) 6038-6043.
- [25] R. Swaidan, B.S. Ghanem, E. Litwiller, I. Pinnau, Pure- and mixed-gas CO<sub>2</sub>/CH<sub>4</sub> separation properties of PIM-1 and an amidoxime-functionalized PIM-1, *J. Membr. Sci.*, 457 (2014) 95-102.
- [26] C.R. Mason, L. Maynard-Atem, N.M. Al-Harbi, P.M. Budd, P. Bernardo, F. Bazzarelli, G. Clarizia, J.C. Jansen, Polymer of intrinsic microporosity incorporating thioamide functionality: Preparation and gas transport properties, *Macromolecules*, 44 (2011) 6471-6479.

- [27] N. Du, G.P. Robertson, M.M. Dal-Cin, L. Scoles, M.D. Guiver, Polymers of intrinsic microporosity (PIMs) substituted with methyl tetrazole, *Polymer*, 53 (2012) 4367-4372.
- [28] R. Swaidan, B. Ghanem, E. Litwiller, I. Pinnau, Effects of hydroxyl-functionalization and sub-T<sub>g</sub> thermal annealing on high pressure pure- and mixed-gas CO<sub>2</sub>/CH<sub>4</sub> separation by polyimide membranes based on 6FDA and triptycene-containing dianhydrides, *J. Membr. Sci.*, 475 (2015) 571-581.
- [29] R.J. Swaidan, X. Ma, E. Litwiller, I. Pinnau, Enhanced propylene/propane separation by thermal annealing of an intrinsically microporous hydroxyl-functionalized polyimide membrane, *J. Membr. Sci.*, 495 (2015) 235-241.
- [30] A. Bos, I.G.M. Pünt, M. Wessling, H. Strathmann, Plasticization-resistant glassy polyimide membranes for CO<sub>2</sub>/CO<sub>4</sub> separations, *Sep. Purif. Technol.*, 14 (1998) 27-39.
- [31] F. Zhou, W.J. Koros, Study of thermal annealing on Matrimid® fiber performance in pervaporation of acetic acid and water mixtures, *Polymer*, 47 (2006) 280-288.
- [32] E.D. Wachsman, C.W. Frank, Effect of cure history on the morphology of polyimide: fluorescence spectroscopy as a method for determining the degree of cure, *Polymer*, 29 (1988) 1191-1197.
- [33] F.Y. Li, Y. Xiao, T.-S. Chung, S. Kawi, High-performance thermally self-cross-linked polymer of intrinsic microporosity (PIM-1) membranes for energy development, *Macromolecules*, 45 (2012) 1427-1437.
- [34] Q. Song, S. Cao, R.H. Pritchard, B. Ghalei, S.A. Al-Muhtaseb, E.M. Terentjev, A.K. Cheetham, E. Sivaniah, Controlled thermal oxidative crosslinking of polymers of intrinsic microporosity towards tunable molecular sieve membranes, *Nat. Commun.*, 5 (2014).
- [35] S.M. Saufi, A.F. Ismail, Fabrication of carbon membranes for gas separation—a review, *Carbon*, 42 (2004) 241-259.
- [36] X. Ma, R. Swaidan, B. Teng, H. Tan, O. Salinas, E. Litwiller, Y. Han, I. Pinnau, Carbon molecular sieve gas separation membranes based on an intrinsically microporous polyimide precursor, *Carbon*, 62 (2013) 88-96.
- [37] K.M. Steel, W.J. Koros, Investigation of porosity of carbon materials and related effects on gas separation properties, *Carbon*, 41 (2003) 253-266.
- [38] A.B. Fuertes, I. Menendez, Separation of hydrocarbon gas mixtures using phenolic resin-based carbon membranes, *Sep. Purif. Technol.*, 28 (2002) 29-41.
- [39] I. Menendez, A.B. Fuertes, Aging of carbon membranes under different environments, *Carbon*, 39 (2001) 733-740.
- [40] J.-i. Hayashi, H. Mizuta, M. Yamamoto, K. Kusakabe, S. Morooka, S.-H. Suh, Separation of ethane/ethylene and propane/propylene systems with a carbonized BPDA–pp'ODA polyimide membrane, *Ind. Eng. Chem. Res.*, 35 (1996) 4176-4181.

- [41] K.-i. Okamoto, S. Kawamura, M. Yoshino, H. Kita, Y. Hirayama, N. Tanihara, Y. Kusuki, Olefin/paraffin separation through carbonized membranes derived from an asymmetric polyimide hollow fiber membrane, *Ind. Eng. Chem. Res.*, 38 (1999) 4424-4432.
- [42] H. Suda, K. Haraya, Alkene/alkane permselectivities of a carbon molecular sieve membrane, *Chem. Commun.*, (1997) 93-94.
- [43] M. Yamamoto, K. Kusakabe, J.-i. Hayashi, S. Morooka, Carbon molecular sieve membrane formed by oxidative carbonization of a copolyimide film coated on a porous support tube, *J. Membr. Sci.*, 133 (1997) 195-205.
- [44] L. Xu, M. Rungta, W.J. Koros, Matrimid® derived carbon molecular sieve hollow fiber membranes for ethylene/ethane separation, *J. Membr. Sci.*, 380 (2011) 138-147.
- [45] M. Rungta, L. Xu, W.J. Koros, Carbon molecular sieve dense film membranes derived from Matrimid® for ethylene/ethane separation, *Carbon*, 50 (2012) 1488-1502.
- [46] K.M. Steel, W.J. Koros, An investigation of the effects of pyrolysis parameters on gas separation properties of carbon materials, *Carbon*, 43 (2005) 1843-1856.
- [47] A.C. Lua, J. Su, Effects of carbonisation on pore evolution and gas permeation properties of carbon membranes from Kapton® polyimide, *Carbon*, 44 (2006) 2964-2972.
- [48] V.C. Geiszler, W.J. Koros, Effects of polyimide pyrolysis conditions on carbon molecular sieve membrane properties, *Ind. Eng. Chem. Res.*, 35 (1996) 2999-3003.
- [49] M. Kiyono, P.J. Williams, W.J. Koros, Effect of pyrolysis atmosphere on separation performance of carbon molecular sieve membranes, *J. Membr. Sci.*, 359 (2010) 2-10.
- [50] J.-i. Hayashi, M. Yamamoto, K. Kusakabe, S. Morooka, Effect of oxidation on gas permeation of carbon molecular sieving membranes based on BPDA-pp'ODA polyimide, *Ind. Eng. Chem. Res.*, 36 (1997) 2134-2140.
- [51] M. Kiyono, P.J. Williams, W.J. Koros, Effect of polymer precursors on carbon molecular sieve structure and separation performance properties, *Carbon*, 48 (2010) 4432-4441.
- [52] Y. Xiao, Y. Dai, T.-S. Chung, M.D. Guiver, Effects of brominating matrimid polyimide on the physical and gas transport properties of derived carbon membranes, *Macromolecules*, 38 (2005) 10042-10049.
- [53] Y.K. Kim, J.M. Lee, H.B. Park, Y.M. Lee, The gas separation properties of carbon molecular sieve membranes derived from polyimides having carboxylic acid groups, *J. Membr. Sci.*, 235 (2004) 139-146.
- [54] S. Fu, E.S. Sanders, S.S. Kulkarni, W.J. Koros, Carbon molecular sieve membrane structure–property relationships for four novel 6FDA based polyimide precursors, *J. Membr. Sci.*, 487 (2015) 60-73.

- [55] H.B. Park, Y.K. Kim, J.M. Lee, S.Y. Lee, Y.M. Lee, Relationship between chemical structure of aromatic polyimides and gas permeation properties of their carbon molecular sieve membranes, *J. Membr. Sci.*, 229 (2004) 117-127.
- [56] Y. Xiao, T.-S. Chung, M.L. Chng, S. Tamai, A. Yamaguchi, Structure and properties relationships for aromatic polyimides and their derived carbon membranes: experimental and simulation approaches, *J. Phys. Chem. B*, 109 (2005) 18741-18748.
- [57] S. Thomas, I. Pinnau, N. Du, M.D. Guiver, Pure- and mixed-gas permeation properties of a microporous spirobisindane-based ladder polymer (PIM-1), *J. Membr. Sci.*, 333 (2009) 125-131.
- [58] L. Xu, M. Rungta, J. Hessler, W. Qiu, M. Brayden, M. Martinez, G. Barbay, W.J. Koros, Physical aging in carbon molecular sieve membranes, *Carbon*, 80 (2014) 155-166.
- [59] L.G. Cançado, A. Jorio, E.H.M. Ferreira, F. Stavale, C.A. Achete, R.B. Capaz, M.V.O. Moutinho, A. Lombardo, T.S. Kulmala, A.C. Ferrari, Quantifying defects in graphene via raman spectroscopy at different excitation energies, *Nano Lett.*, 11 (2011) 3190-3196.
- [60] L. Shao, T.-S. Chung, K.P. Pramoda, The evolution of physicochemical and transport properties of 6FDA-durene toward carbon membranes; from polymer, intermediate to carbon, *Microporous Mesoporous Mater.*, 84 (2005) 59-68.
- [61] J. Landers, G.Y. Gor, A.V. Neimark, Density functional theory methods for characterization of porous materials, *Colloids Surf., A*, 437 (2013) 3-32.
- [62] A. Wahby, J. Silvestre-Albero, A. Sepúlveda-Escribano, F. Rodríguez-Reinoso, CO<sub>2</sub> adsorption on carbon molecular sieves, *Microporous Mesoporous Mater.*, 164 (2012) 280-287.

## Chapter 6

### **High-Performance Carbon Molecular Sieve and Polybenzoxazole Membranes for Ethylene/Ethane Separation Derived from an Intrinsically Microporous Polyimide<sup>1</sup>**

An intrinsically microporous polymer with hydroxyl functionalities, PIM-6FDA-OH, was used as a precursor for various types of carbon molecular sieve (CMS) and polybenzoxazole (PBO) membranes for ethylene/ethane separation. The pristine polyimide films were heated under controlled N<sub>2</sub> atmosphere at different stages from 400 to 800 °C. The PBO membranes had poor ethylene/ethane separation properties ( $\alpha \sim 2.2$ ). However, all CMS samples carbonized above 600 °C surpassed the polymeric ethylene/ethane upper bound. Pure-gas selectivity reached 17.5 for the CMS carbonized at 800 °C with an ethylene permeability of about 10 Barrer at 2 bar and 35 °C, becoming the most selective CMS for ethylene/ethane separation reported to date. As expected, gravimetric sorption experiments showed that all CMS membranes had ethylene/ethane solubility selectivities close to one. The permselectivity increased with increasing pyrolysis temperature due to densification of the micropores in the CMS membranes, leading to enhanced diffusivity selectivity. Mixed-gas tests with a binary 50:50 v/v ethylene/ethane feed showed a decrease in selectivity from 14 to 8.3 as the total feed pressure was increased from 4 to 20 bar. The selectivity drop under mixed-gas conditions was attributed to non-ideal effects: (i) competitive sorption that reduced the permeability of ethylene and (ii) dilation of the CMS that resulted in an increase in the ethane permeability.



<sup>1</sup>Adapted from O. Salinas, X. Ma, E. Litwiller, I. Pinnau, J. Membr. Sci., 500 (2016) 115-123.

## 6.1 Introduction

The worldwide ethylene production by steam cracking was 141 million tons in 2011 which is higher than that of any other organic compound [1]. The ethylene-rich stream exiting the cracker must be separated from other organic compounds such as ethane. The ethylene/ethane separation step is extremely challenging due to the similarities in size of the molecules (Lennard-Jones diameter: 4.23 Å for ethylene and 4.42 Å for ethane [2] and condensability (critical temperature: 9.2 °C for ethylene and 32.3 °C for ethane). In current practice this separation is accomplished by highly energy-intensive cryogenic distillation. Membranes separate mixtures without requiring a phase change [3], so incorporating a membrane into the cryogenic process can potentially reduce its energy consumption, provided that a suitable membrane material can be developed. Recent process modeling indicated that coupling the ethylene/ethane distillation column with a membrane process to debottleneck the operation could potentially save energy [4-6]. However, the advantages of using a hybrid system will only outweigh the cost of implementation if a membrane material exhibits high ethylene/ethane selectivity (15-20) and withstands realistic process conditions [7].

Currently available commercial membrane materials used for gas separation mainly comprise low-free-volume, solution-processable, glassy polymers, which exhibit an inverse relationship between permeability and selectivity [8, 9]. In 2013, Rungta and Koros reported the polymer upper bound for the ethylene/ethane system [10] based on pure-gas permeation properties, with 6FDA-NDA copolymers providing the highest combination of

permeability and selectivity [11, 12]. To date, the best performing polymers offer pure-gas ethylene/ethane selectivities of  $< 7$ , even at low pressures. Under high feed pressure mixed-gas conditions (i.e. high hydrocarbon activities) penetrant-induced plasticization typically causes even lower selectivity [13, 14].

Recent research efforts have been devoted to the study of polymers of intrinsic microporosity (PIMs) for various gas separation applications [15-21]. PIMs possess high BET surface area (up to  $1000 \text{ m}^2/\text{g}$ ) with pores of less than 2 nm. Remarkably, PIM polymers have a large free volume fraction of finer pores  $< 7 \text{ \AA}$  (i.e. ultra-micropores), which may discriminate between gases with small differences in molecular dimensions and some types have significantly surpassed previously reported 2008 polymeric upper bound performance for air and hydrogen separation [22]. So far, pure-gas ethylene/ethane separation performance of PIM-materials has only been reported for PIM-1 [23], which offered poor separation due to its very broad pore size distribution (PSD). Tailoring microporosity is essential to developing advanced materials for ethylene/ethane separation.

In general, polymers can gain microporosity if they are heated beyond their degradation temperature. Reactions that occur when the polymer is heated depend on reaction conditions (temperature [24], thermal-soak [25], and atmosphere composition [26, 27]), and the nature of the precursor itself [28-30]. Pyrolysis of the polymer chains leads to the formation of carbon molecular sieves (CMS) [31-33]. CMS membranes have narrower PSDs than polymers and, therefore, better molecular sieving capabilities [34]. Furthermore, carbon membranes have shown chemical stability after long-term exposure to hydrocarbons at low pressures [35, 36], which makes them promising candidates for olefin/paraffin separation. Thermal treatment may lead to materials with the PSD and

stability needed to meet the benchmarks for improving ethylene/ethane separation. In fact, the ethylene/ethane transport properties of CMS materials usually surpass the polymeric upper bound due to their high permselectivities ( $\alpha_{C_2H_4/C_2H_6} \sim 7-12$ ) [36-42]. Recently, a polymeric precursors used to generate these carbons have been either traditional low-free-volume polymers (e.g. Matrimid®) or polymers that do not have contortion centers that inhibit chain packing as the ones reported in the PIM literature (e.g. tetrahedral spiro carbon).

Recently, a polyimide with intrinsic microporosity (PIM-PI), PIM-6FDA-OH, containing hydroxyl functionalities in ortho position relative to the imide linkage showed enhanced inter- and intra-chain interactions [43]. As a result, the polymer matrix was more diffusion-selective compared to the prototypes from the PIM-polyimide family [44]. Previous studies indicated that CMS derived from PIM-6FDA-OH showed attractive pure-gas selectivity for CO<sub>2</sub>/CH<sub>4</sub> and O<sub>2</sub>/N<sub>2</sub> separations [44]. In addition, the mixed-gas CO<sub>2</sub>/CH<sub>4</sub> permeation properties of carbonized samples derived from PIM-6FDA-OH were assessed while increasing the feed pressure to realistic industrial values [45].

In this chapter, carbonized PIM-6FDA-OH samples were evaluated for ethylene/ethane separation. Pure-gas ethylene and ethane permeation properties of isotropic films prepared under a range of treatment conditions are reported. The effect of pressure on membrane performance was evaluated for a 50:50 mixed-gas feed. These results are complemented with sorption isotherms at 35 °C where the appropriate sorption models were fitted to the data.

## 6.2 Thermal-annealing of PIM-6FDA-OH

Freshly-cast films showed an increase in bulk density from 1.22 g cm<sup>-3</sup> for the 120 °C-dried film reported in [43] to 1.28 g cm<sup>-3</sup> for a 250 °C-annealed film reported in this study. This densification due to thermal annealing decreased the permeability of H<sub>2</sub>, N<sub>2</sub>, O<sub>2</sub>, CH<sub>4</sub> and CO<sub>2</sub> in PIM-6FDA-OH by about 50%, as shown in the **Table 5.1**. Annealing microporous functionalized polyimides is known to be beneficial for their selectivity due to the formation of charge transfer complexes (CTCs) [46, 47].

**Table 6.1.** Gas permeation properties of thermally annealed PIM-6FDA-OH measured at 2 bar and 35 °C.

Drying protocol (°C)	Permeability					$\alpha_{x/y}$	
	H <sub>2</sub>	N <sub>2</sub>	O <sub>2</sub>	CH <sub>4</sub>	CO <sub>2</sub>	O <sub>2</sub> /N <sub>2</sub>	CO <sub>2</sub> /CH <sub>4</sub>
250 <sup>a</sup>	181	5.5	23.8	3.4	119	4.4	35
120 <sup>b</sup>	259	11	45	9	251	4.2	28

<sup>a</sup> This work

<sup>b</sup> Previous communication; the film was conditioned for 24 h at 120 °C [48]

<sup>c</sup> 1 Barrer = 10<sup>-10</sup> cm<sup>3</sup> (STP) cm cm<sup>-2</sup> s<sup>-1</sup> cmHg<sup>-1</sup> or 7.5 × 10<sup>-18</sup> m<sup>3</sup> (STP) m m<sup>-2</sup> s<sup>-1</sup> Pa<sup>-1</sup>

## 6.3 Heat treatment of PIM-6FDA-OH

As reported previously, the onset of the decomposition temperature of PIM-6FDA-OH is ~380 °C [48]. CO<sub>2</sub> evolution (related to PBO formation [48, 49]) occurred mainly from 400 to 450 °C, while H<sub>2</sub>O peaked at 550 °C confirming backbone scission reactions (**Fig. 6.1**). The PBO formation can be confirmed in the FTIR spectra shown in **Fig. 6.2**.

The carbonization of PIM-6FDA-OH was related to the decrease in infrared-sensitivity (i.e. loss of functionalities) of the PIM-PI for pyrolysis above 500 °C (**Fig. 6.3**). The weight loss of PIM-6FDA-OH for each heat-treatment temperature is shown in **Fig. 6.4a**. After 30 min thermal-soak at 500 °C, PIM-6FDA OH lost ~30% of its initial (pristine) weight and the films became pitch-black. In addition, the samples gained Raman sensitivity (**Fig. 6.5**), which proved the existence of graphene in its damaged form [50].

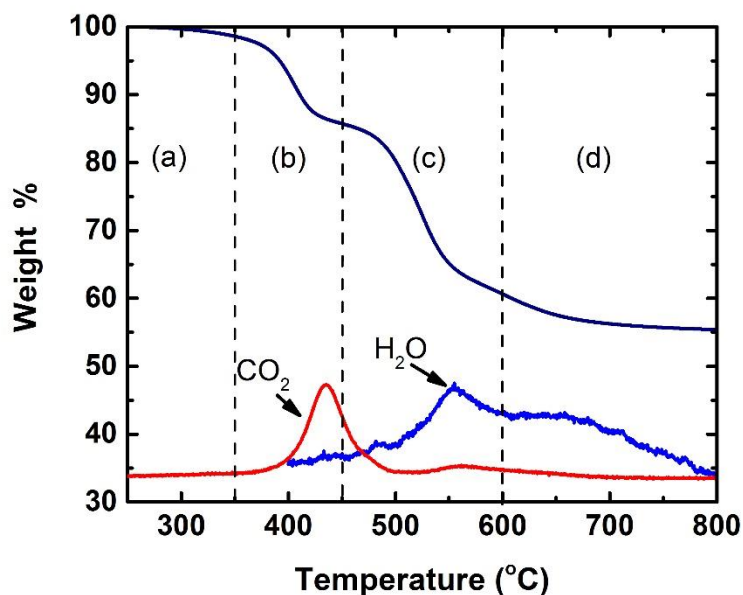


**Fig. 6.1.** Thermal gravimetric analysis of PIM-6FDA-OH under an inert N<sub>2</sub> atmosphere at a ramping rate of 3 °C min<sup>-1</sup>. Mass-spectrometry qualitative depicts H<sub>2</sub>O and CO<sub>2</sub> evolution. Four different stages of degradation can be detected (a) limit of thermal stability, (b) polybenzoxazole formation, (c) degradation into amorphous carbon, (d) sintering of CMS.

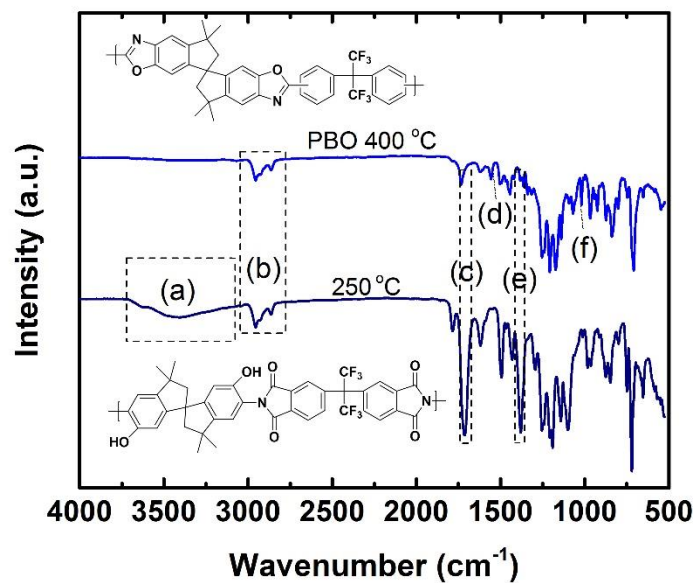


**Fig. 6.2.** FTIR spectra of PIM-6FDA-OH and derived PBO: (a) represents hydroxyl groups, (b) methyl stretch that remain unchanged after the PBO formation, (c) and (e) decrease representing the imide stretch; lastly, PBO characteristics peaks: (d) and (f) are shown after the film was treated at 400 °C.

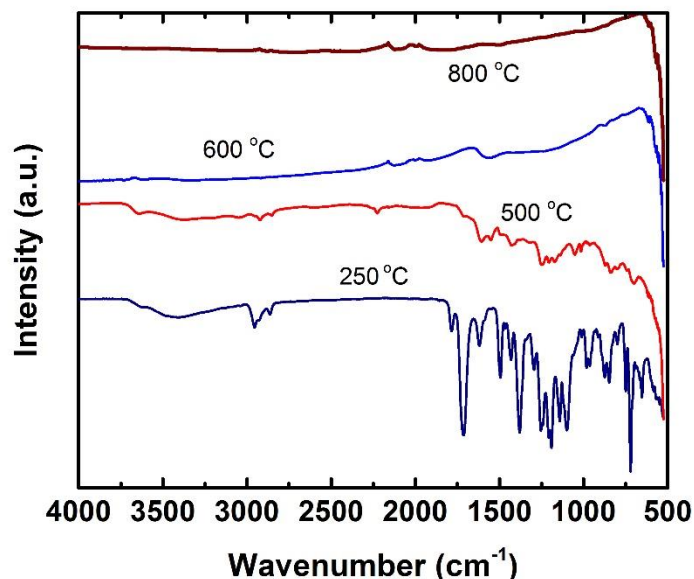


**Fig. 6.3.** FTIR spectra of PIM-6FDA-OH and derived heat-treated samples.

The thermal degradation of the samples can be divided into two prominent regimes: i) pore opening and ii) pore sintering. The former is associated with nearly 30% of the weight loss, (i.e. for a pyrolysis temperature of 500 °C) whereas the latter showed only 15% mass loss above 600 °C. These pore formation mechanisms can be elucidated from the XRD spectra shown in **Fig. 6.4(b)**. Degradation of the pristine PI at 500 °C increased the d-spacing from 5.53 to 6.22 Å by virtue of the formation of damaged graphene. Carbonization above 600 °C was related to internal reconfigurations towards a more ordered molecular sieve, as demonstrated in the bimodal XRD spectra. An increase in the intensity of the 2.05 Å (1 0 0) graphene plane peak [51] indicated an enhancement of the ultramicroporosity in the samples. The larger d-spacing reached a minimum of 3.75 Å for samples made at 800 °C. However, even the most carbonized samples had wide halos in

the XRD spectra, indicating a high percentage of amorphous material was still imbedded in the final structure. The carbonization process is depicted in **Fig. 6.6**.

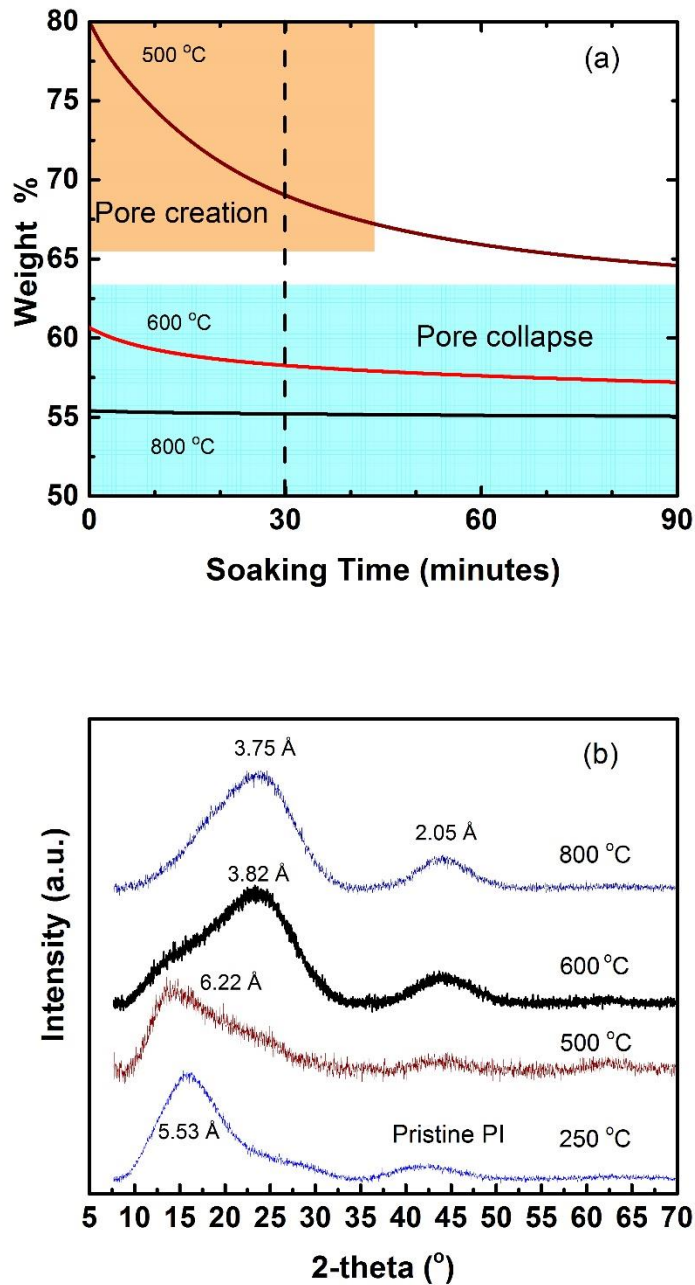


**Fig. 6.4.** (a) Weight loss of PIM-6FDA-OH for each isothermal stage of degradation. Shaded areas show the dominating porosity evolution mechanisms during heat treatment



while the dashed line was the actual soak time used in the pyrolysis protocol; (b) XRD spectra of all samples.

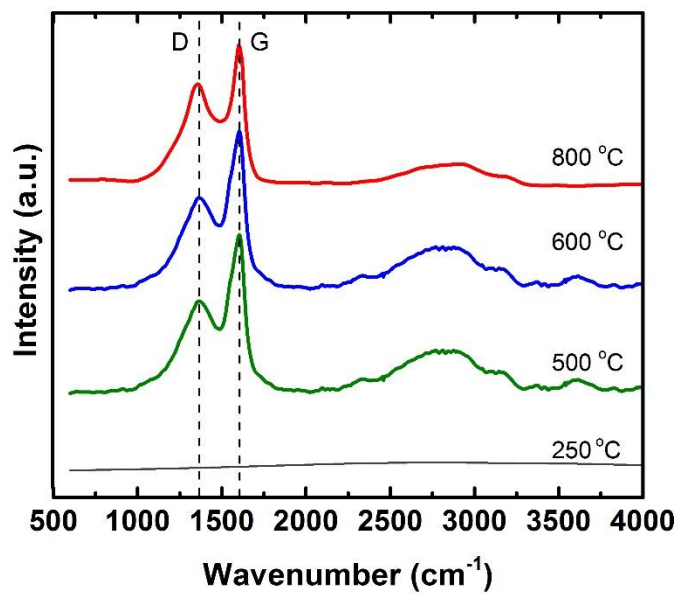


**Fig. 6.5.** Raman spectrum becomes active at 500 °C due to the growth of carbonaceous domains in the CMS samples as elucidated with the D and G peaks (dashed lines).

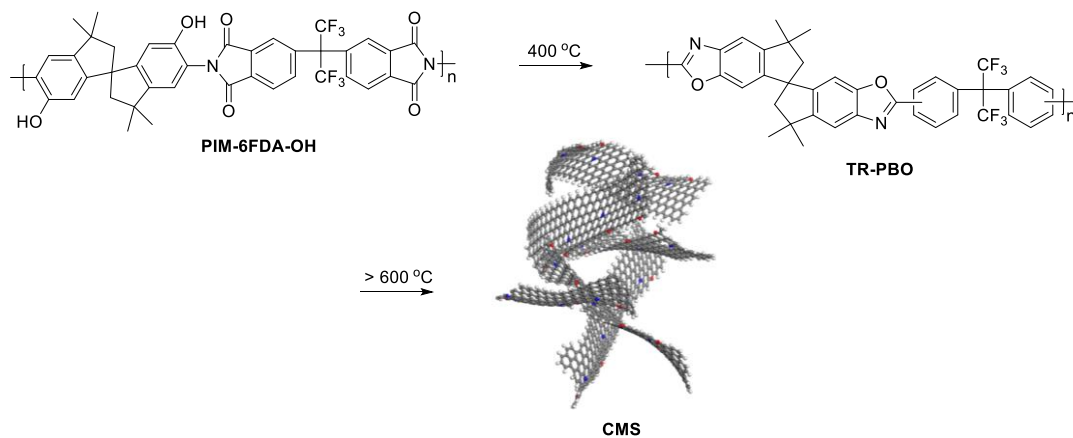


**Fig. 6.6.** Heat treatment of PIM-6FDA-OH. At 600 °C the thermally rearranged PBO structure degrades into turbostratic graphene layers that sinter as the pyrolysis temperature increases. Non-carbon impurities (as significant as 10% molar [48]) are contained within the honeycomb array of the turbostratic graphene sheets (generated in Material Studio, version 8.0).

#### 6.4 *CO<sub>2</sub> sorption for PSD estimation of carbonized samples*

CO<sub>2</sub> sorption can be used to probe the smallest of the CMS ultra-micropores [52], which could potentially discriminate ethylene from ethane. PIM-6FDA-OH derived CMS samples exhibited a larger CO<sub>2</sub> uptake in the low-pressure range (i.e.  $p/p_o < 10^{-3}$ ) as the carbonization temperature increased, as shown in **Fig. 6.7**. The carbonization of PIM-6FDA-OH at 500 °C amplified the ultramicroporous gates that connect the initially generated microporous cavities. In addition, CO<sub>2</sub> uptake nearly doubled after PIM-6FDA-OH was carbonized at 500 °C, from 1.5 mmol g<sup>-1</sup> to 2.6 mmol g<sup>-1</sup> at  $p/p_o$  of 0.028. Uptake then further increased to 3.6 mmol g<sup>-1</sup> at 600 °C and 4 mmol g<sup>-1</sup> at 800 °C, respectively.

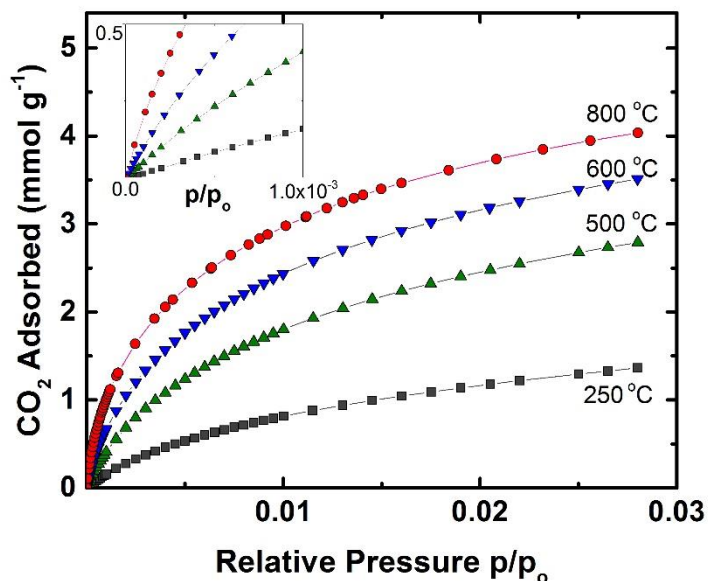


**Fig. 6.7.** Physisorption of CO<sub>2</sub> at 0 °C in PIM-6FDA-OH and its heat-derived CMS membranes. Low-pressure sorption is shown in the upper left corner of the graph.

The PSD obtained from CO<sub>2</sub> sorption at 0 °C is shown in **Fig. 6.8**. A bimodal ultramicropore distribution was detected in all samples. It can be seen that there was a strong growth of the 3.6 Å pores with an increase in pyrolysis temperature. Similarly, the fraction of larger pores from 4.5 - 6 Å increased after heat treatment of 500 °C or higher.

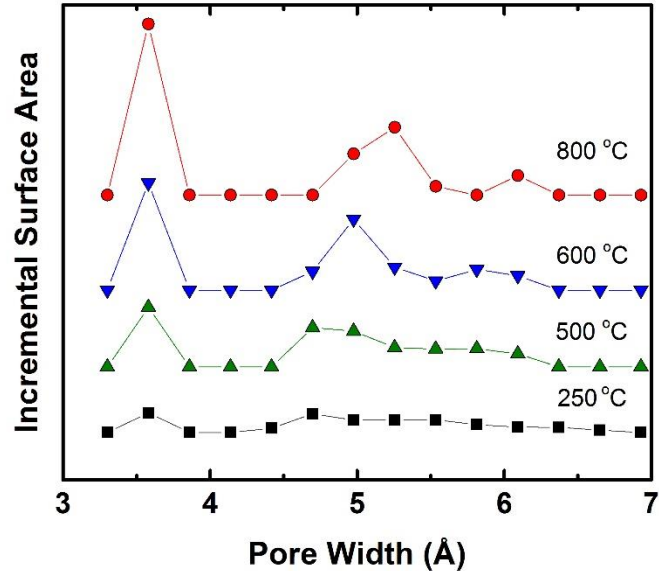


**Fig. 6.8.** PSD from the NLDFT method derived from CO<sub>2</sub> sorption data at 0 °C for the pristine PIM-6FDA-OH conditioned at 250 °C and its derived CMS samples.

Steel and Koros proposed an idealized pore structure model that can be used to qualitatively describe the molecular sieving mechanism in a CMS membrane [53]. PIM-6FDA-OH is a rigid polymer with entrapped free volume that remains “static” compared to the time scale of molecular diffusion. Therefore, the Steel and Koros model may be applied to understand changes on the critical dimension,  $d_c$ , of the ultra-micropores responsible for the separation. The overall effect of heat-treating PIM-6FDA-OH is shown schematically in **Fig. 6.9**.

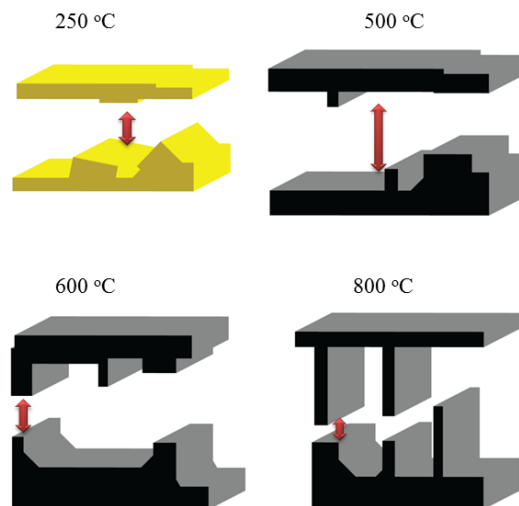
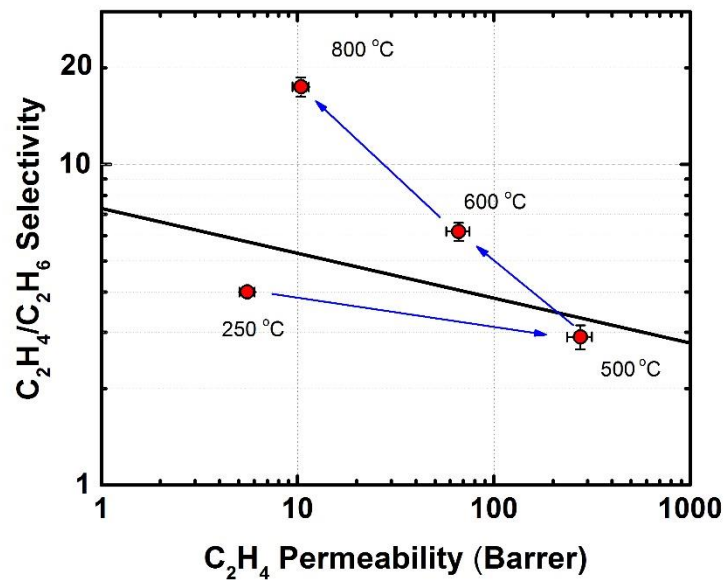


**Fig. 6.9.** Schematic pore evolution of PIM-6FDA-OH and its heat-derived CMS samples. The red arrow represents the critical dimension  $d_c$  of ultramicropores, which determines the molecular sieving behavior of the membranes.

### 6.5 Ethylene/ethane pure-gas permeation properties

Ethylene/ethane pure-gas permeabilities and ideal selectivities are shown in **Fig. 6.10** whereas the rest of the gases may be found the Appendix of this thesis. The 250 °C-annealed PIM-6FDA-OH showed modest performance with a selectivity of 4 and an ethylene permeability of 5.5 Barrer. The PBO derived sample from PIM-6FDA-OH was an order of magnitude more permeable than PIM-6FDA-OH; however, the ethylene/ethane selectivity dropped to only 2. Heat treatment at 500 °C increased the ethylene permeability of the CMS by a factor of 50 relative to PIM-6FDA-OH but its selectivity was only 2.9. The 500 °C-treated sample was the most ethylene permeable film tested in this work, with

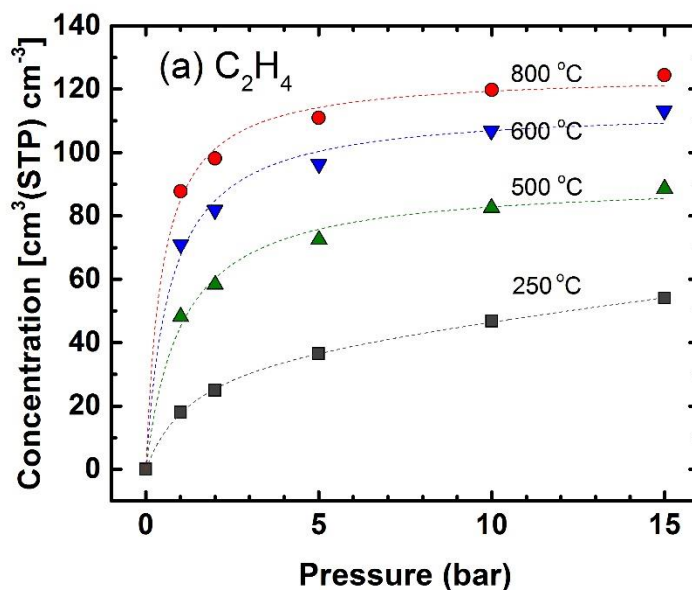
a value of 276 Barrer. This is most likely due to the formation of some larger pores around 4.5 to 6 Å, as shown in **Fig. 6.8**. Heat treatment at higher temperatures reduced permeability, as a result of the pore contraction confirmed by XRD and CO<sub>2</sub> sorption tests. From 600 to 800 °C, ethylene permeability decreased from 66.1 to 10.4 Barrer. All samples treated at temperatures above 600 °C surpassed the polymeric ethylene/ethane upper bound. Selectivity reached 17.5 when the samples were carbonized at 800 °C



**Fig. 6.10.** Pure-gas ethylene/ethane permeation properties of CMS membranes derived from PIM-6FDA-OH. The polymer upper bound is represented with the bold black line [10].

## 6.6 Gravimetric sorption isotherms at 35 °C for ethylene and ethane

Sorption isotherms of ethylene and ethane, shown in **Fig. 5.7**, were determined by gravimetric sorption. Gas uptake for the 250 °C annealed PIM-6FDA-OH displayed the expected dual-mode sorption behavior for both gases. The CMS derivatives presented much larger sorption capacity than their polyimide precursor. The shapes of the CMS isotherms resembled Langmuir sorption behavior due to the significant growth of their ultramicroporous domains (i.e. the smaller pores are filled at low pressures). Fitted dashed curves followed the dual-mode sorption model for the polymeric PIM-PI sample heated at 250 °C, whereas the Langmuir model was used to describe sorption in the CMS.



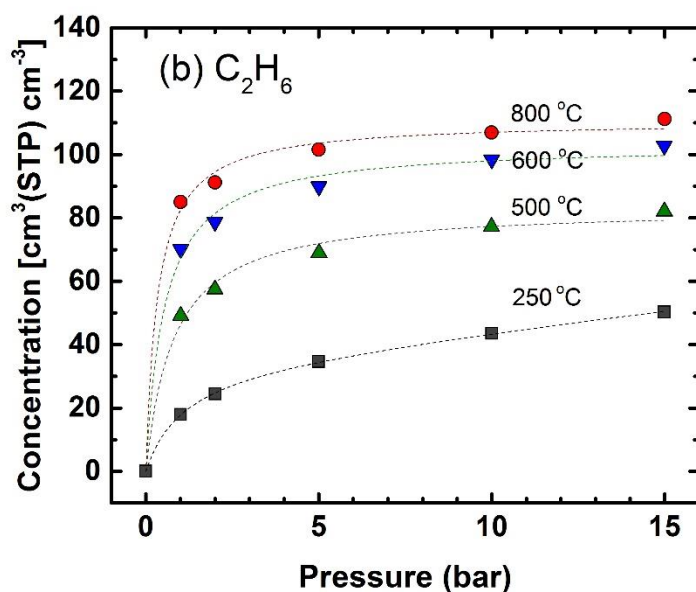


**Fig. 6.11.** Pure-gas sorption isotherms of (a) ethylene and (b) ethane at 35 °C in PIM-6FDA-OH and its CMS derivatives. Fitted dashed curves follow the dual-mode sorption model for the polymeric PIM-PI annealed at 250 °C, whereas the Langmuir model was used to describe sorption in the CMS samples.

The parameters of the fitted sorption models are summarized in **Table 6.2**. The overall trend indicates an increase of  $C'_H$  and  $b$  with increasing treatment temperature. For example, ethylene  $C'_H$  of the 800 °C-treated film has a value of 125 cm<sup>3</sup>(STP)/cm<sup>3</sup>, three times higher than the  $C'_H$  of the original polymeric precursor annealed at 250 °C. This result is consistent with the enhanced CO<sub>2</sub> sorption uptake for carbonized PIM-6FDA-OH shown previously.

**Table 6.2.** Parameters obtained from fitting experimental data to the dual-mode (pristine PIM-6FDA-OH) and the Langmuir isotherms (carbons).



Treatment Temperature (°C)	Gas	$K_D$ $10^{-2} * (\text{cm}^3 \text{cm}^{-3} \text{cmHg}^{-1})$	$C'_H$ $(\text{cm}^3 \text{cm}^{-3})$	$b$ $10^{-2} * (\text{cmHg}^{-1})$
250	Ethylene	1.53	42.0	0.62
	Ethane	1.65	34.1	1.25
500	Ethylene	-	91.4	1.29
	Ethane	-	83.5	3.07
600	Ethylene	-	114.3	1.91
	Ethane	-	103.3	2.48
800	Ethylene	-	125.0	2.83
	Ethane	-	110.6	3.91

### 6.7 Pure-gas diffusivity and solubility of ethylene and ethane

The solubility coefficients of PIM-6FDA-OH and its heat-treated samples are shown in **Fig. 6.12**. Carbon formation in samples treated above 500 °C led to considerable enhancement in solubility of both gases. Ethylene solubility increased from 0.17 at 250 °C to 0.39 at 500 °C, and then to 0.66 cm<sup>3</sup>(STP) cm<sup>-3</sup> cmHg<sup>-1</sup> in the most graphitic 800 °C sample. However, solubility selectivity in all samples remained very close to 1 due to the very similar condensabilities of both hydrocarbons.

Ethylene and ethane diffusion coefficients of all membranes are shown in **Fig. 6.13**. The evolution of the pore structure is the most important factor influencing diffusivity. Intermediate carbonization at 500 °C resulted in a 20-fold increase in ethylene diffusivity and a 30-fold increase in ethane diffusivity compared to the pristine PI. At 800 °C, pore collapse and the rise of the ultramicroporosity in the CMS decreased diffusion coefficients 44-fold from 7.1x10<sup>-8</sup> to 1.6x10<sup>-9</sup> cm<sup>2</sup> s<sup>-1</sup> for ethylene and 255-fold from 2.5x10<sup>-8</sup> to 9.8x10<sup>-10</sup>

$^{11} \text{ cm}^2 \text{ s}^{-1}$  for ethane. The diffusivity ratio essentially matched the actual pure-gas selectivity for the whole temperature range, verifying the dominance of the molecular sieving mechanism (**Fig. 6.14**).

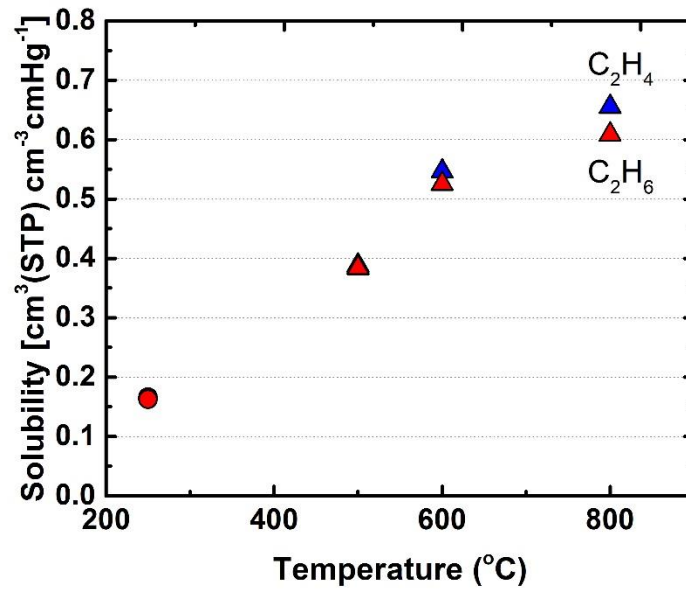


**Fig. 6.12.** Solubility of ethylene and ethane in PIM-6FDA-OH (●) and its CMS (▲) derivatives at 35 °C and 2 bar.

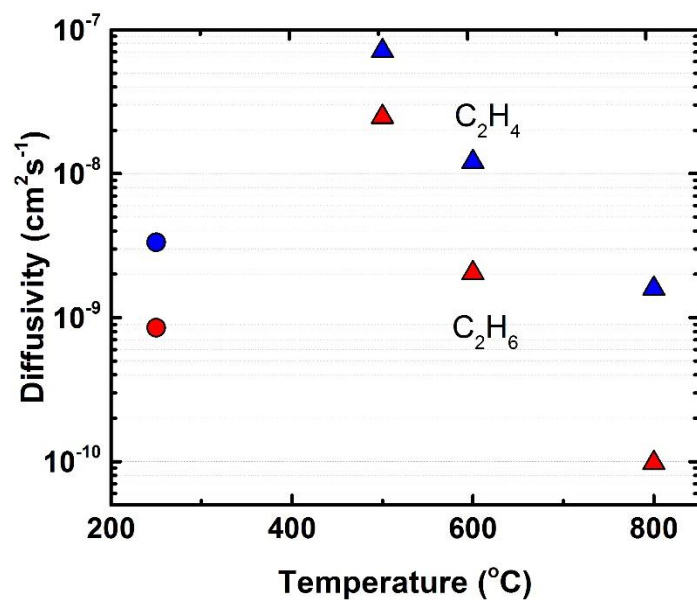


**Fig. 6.13.** Diffusivity of ethylene and ethane in PIM-6FDA-OH (●) and its CMS (▲) samples at 35 °C and 2 bar.

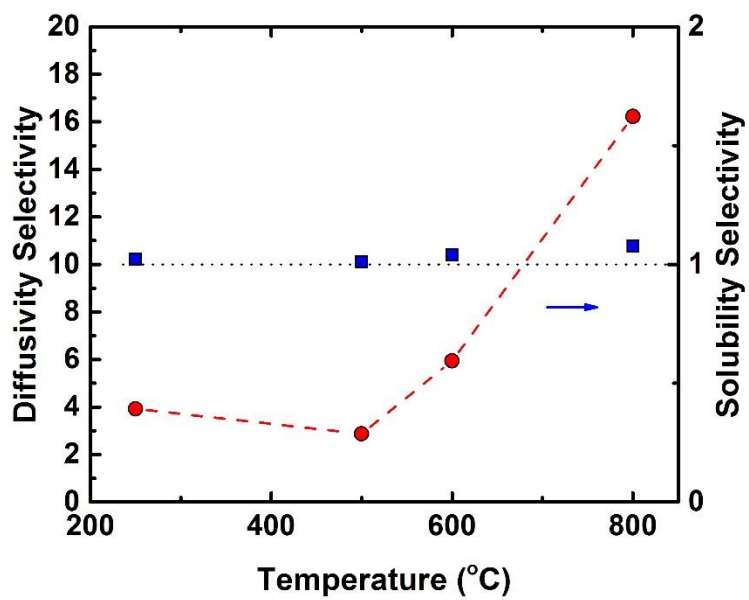


**Fig. 6.14.** Ethylene/ethane diffusivity and solubility selectivities in PIM-6FDA-OH (●) and its CMS derivatives (▲). The fitted lines are drawn to guide the eye.

### 6.8 *Mixed-gas permeability and selectivity of the 800 °C CMS membrane*

The PIM-6FDA-OH sample carbonized at 800 °C was tested with a 50:50 v/v ethylene/ethane mixture and the results are shown in **Fig. 6.15a**. Ethylene permeability decreased from 10.6 Barrer at 4 bar total pressure to 9.6 Barrer at 20 bar, possibly due to competitive sorption of ethylene and ethane in the CMS. On the other hand, ethane permeability increased from 0.75 to 1.16 Barrer over the same pressure range, which could be the result of a subtle dilation of the critical ultramicropores in the presence of ethylene. The strongly time-dependent effect of the pressure on the mixed-gas selectivity is illustrated in **Fig. 6.15b**. At a feed pressure of 4 bar it took about 300 h to reach pseudo-equilibrium state. At intermediate pressures of 8 to 12 bar the equilibration time was reduced to about 120 h. A similar carbon matrix dilation was observed previously for the CO<sub>2</sub>/CH<sub>4</sub> gas pair for PIM-6FDA-OH-derived CMS membranes [45]. Despite the losses in selectivity, the performance remains above the pure-gas polymer upper bound, as seen in **Fig. 6.16**.

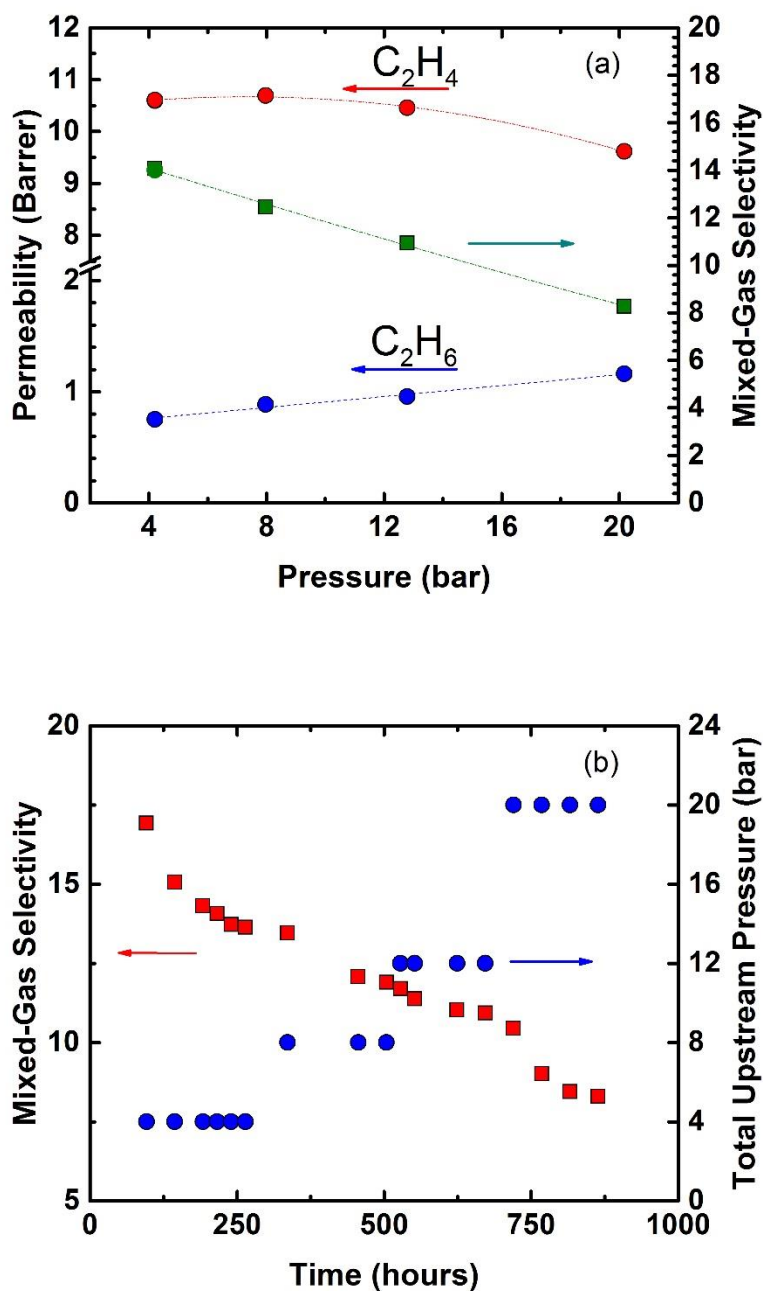


**Fig. 6.15.** (a) Pressure dependence of the mixed-gas transport properties of a 1:1 ethylene/ethane binary mixture and (b) time required to reach pseudo-equilibrium at each pressure for the CMS membrane heat-treated at 800 °C derived from PIM-6FDA-OH.

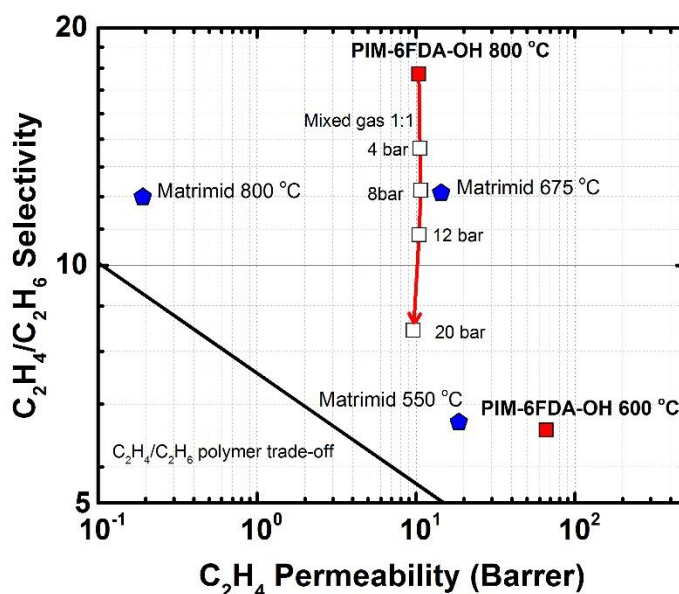


**Fig. 6.16.** Single ethylene permeability and ethylene/ethane selectivity of CMS derived from PIM-6FDA-OH (red closed squares). Mixed-gas selectivity dropped from 14 to 8.3 as the feed pressure was increased from 4 to 20 bar (open squares). Matrimid® polyimide-based CMS (blue) pure-gas permeation at 35 °C and 3.4 bar [41].

## 6.9 Conclusions

Carbon membranes and PBO derived from an intrinsically microporous PIM-6FDA-OH precursor via thermal treatment were evaluated for ethylene/ethane separation. The PBO structure was too open to selectively discriminate between the ethylene and ethane molecules. However, separation performance increased dramatically with temperature for the carbonized samples. In contrast to CMS membranes derived from lower-free-volume polyimides (e.g. Matrimid®), the CMS derived from PIM-6FDA-OH underwent degradations that prevented the full collapse (shift to smaller pore size) of its

PSD even for the most carbonized sample, retaining a pure-gas ethylene permeability of about 10 Barrer. It is suggested that the spiro-containing PIM-6FDA-OH possesses properties (high free volume, chain rigidity and thermal stability) responsible for hindering sintering of the graphene sheets as they were formed during the pyrolysis process.

Mixed-gas permeation experiments for the CMS membrane pyrolyzed at 800 °C performed at 20 bar showed that the ethylene permeability dropped by ~10% most likely due to competitive sorption effects. On the other hand, slight dilatation of the CMS ultramicropore structure resulted in an increase in the ethane permeability by 54%. Consequently, the mixed-gas ethylene/ethane selectivity dropped from pure-gas value of 17.5 at 2 bar to 8.3 at a feed pressure of 20 bar. Our study provides further evidence that the choice of the polymer precursor strongly determines the final structure and gas transport properties of CMS membranes.

## 6.10 References

- [1] T. Ren, M. Patel, K. Blok, Olefins from conventional and heavy feedstocks: energy use in steam cracking and alternative processes, *Energy*, 31 (2006) 425-451.
- [2] J.O. Hirschfelder, C.F. Curtiss, R.B. Bird, M.G. Mayer, *Molecular theory of gases and liquids*, Wiley, New York, 1954.
- [3] R.W. Baker, J.G. Wijmans, J.H. Kaschemekat, The design of membrane vapor-gas separation systems, *J. Membr. Sci.*, 151 (1998) 55-62.
- [4] J.A. Caballero, I.E. Grossmann, M. Keyvani, E.S. Lenz, Design of hybrid distillation-vapor membrane separation systems, *Ind. Eng. Chem. Res.*, 48 (2009) 9151-9162.
- [5] A. Motelica, O.S.L. Bruinsma, R. Kreiter, M. den Exter, J.F. Vente, Membrane retrofit option for paraffin/olefin separation—a technoeconomic evaluation, *Ind. Eng. Chem. Res.*, 51 (2012) 6977-6986.
- [6] J. Ploegmakers, A.R.T. Jelsma, A.G.J. van der Ham, K. Nijmeijer, Economic evaluation of membrane potential for ethylene/ethane separation in a retrofitted hybrid membrane-distillation plant using unisim design, *Ind. Eng. Chem. Res.*, 52 (2013) 6524-6539.
- [7] R.W. Baker, B.T. Low, Gas separation membrane materials: a perspective, *Macromolecules*, 47 (2014) 6999-7013.
- [8] L.M. Robeson, Correlation of separation factor versus permeability for polymeric membranes, *J. Membr. Sci.*, 62 (1991) 165-185.
- [9] L.M. Robeson, The upper bound revisited, *J. Membr. Sci.*, 320 (2008) 390-400.
- [10] M. Rungta, C. Zhang, W.J. Koros, L. Xu, Membrane-based ethylene/ethane separation: the upper bound and beyond, *AIChE Journal*, 59 (2013) 3475-3489.
- [11] S.S. Chan, R. Wang, T.-S. Chung, Y. Liu, C2 and C3 hydrocarbon separations in poly(1,5-naphthalene-2,2-bis(3,4-phthalic) hexafluoropropane) diimide (6FDA-1,5-NDA) dense membranes, *J. Membr. Sci.*, 210 (2002) 55-64.
- [12] S.S. Chan, T.-S. Chung, Y. Liu, R. Wang, Gas and hydrocarbon (C2 and C3) transport properties of co-polyimides synthesized from 6FDA and 1,5-NDA (naphthalene)/Durene diamines, *J. Membr. Sci.*, 218 (2003) 235-245.
- [13] C. Staudt-Bickel, W.J. Koros, Olefin/paraffin gas separations with 6FDA-based polyimide membranes, *J. Membr. Sci.*, 170 (2000) 205-214.



- [14] R.J. Swaidan, B. Ghanem, R. Swaidan, E. Litwiller, I. Pinnau, Pure- and mixed-gas propylene/propane permeation properties of spiro- and triptycene-based microporous polyimides, *J. Membr. Sci.*, 492 (2015) 116-122.
- [15] P.M. Budd, K.J. Msayib, C.E. Tattershall, B.S. Ghanem, K.J. Reynolds, N.B. McKeown, D. Fritsch, Gas separation membranes from polymers of intrinsic microporosity, *J. Membr. Sci.*, 251 (2005) 263-269.
- [16] P.M. Budd, B.S. Ghanem, S. Makhseed, N.B. McKeown, K.J. Msayib, C.E. Tattershall, Polymers of intrinsic microporosity (PIMs): robust, solution-processable, organic nanoporous materials, *Chem. Commun.*, (2004) 230-231.
- [17] P.M. Budd, N.B. McKeown, D. Fritsch, Polymers of intrinsic microporosity (PIMs): high free volume polymers for membrane applications, *Macromol. Symp.*, 245-246 (2006) 403-405.
- [18] Y. Zhuang, J.G. Seong, Y.S. Do, H.J. Jo, Z. Cui, J. Lee, Y.M. Lee, M.D. Guiver, Intrinsically microporous soluble polyimides incorporating Tröger's base for membrane gas separation, *Macromolecules*, 47 (2014) 3254-3262.
- [19] B.S. Ghanem, R. Swaidan, E. Litwiller, I. Pinnau, Ultra-microporous triptycene-based polyimide membranes for high-performance gas separation, *Adv. Mater.*, 26 (2014) 3688-3692.
- [20] M. Carta, M. Croad, R. Malpass-Evans, J.C. Jansen, P. Bernardo, G. Clarizia, K. Friess, M. Lanč, N.B. McKeown, Triptycene induced enhancement of membrane gas selectivity for microporous Tröger's base polymers, *Adv. Mater.*, 26 (2014) 3526-3531.
- [21] N. Du, H.B. Park, G.P. Robertson, M.M. Dal-Cin, T. Visser, L. Scoles, M.D. Guiver, Polymer nanosieve membranes for CO<sub>2</sub>-capture applications, *Nat. Mater.*, 10 (2011) 372-375.
- [22] R. Swaidan, B. Ghanem, I. Pinnau, Fine-tuned intrinsically ultramicroporous polymers redefine the permeability/selectivity upper bounds of membrane-based air and hydrogen separations, *ACS Macro Lett.*, (2015) 947-951.
- [23] P. Li, T.S. Chung, D.R. Paul, Gas sorption and permeation in PIM-1, *J. Membr. Sci.*, 432 (2013) 50-57.
- [24] L. Shao, T.-S. Chung, G. Wensley, S.H. Goh, K.P. Pramoda, Casting solvent effects on morphologies, gas transport properties of a novel 6FDA/PMDA-TMMDA copolyimide membrane and its derived carbon membranes, *J. Membr. Sci.*, 244 (2004) 77-87.
- [25] K.M. Steel, W.J. Koros, An investigation of the effects of pyrolysis parameters on gas separation properties of carbon materials, *Carbon*, 43 (2005) 1843-1856.
- [26] M. Kiyono, P.J. Williams, W.J. Koros, Effect of pyrolysis atmosphere on separation performance of carbon molecular sieve membranes, *J. Membr. Sci.*, 359 (2010) 2-10.

- [27] Q. Song, S. Cao, R.H. Pritchard, B. Ghalei, S.A. Al-Muhtaseb, E.M. Terentjev, A.K. Cheetham, E. Sivaniah, Controlled thermal oxidative crosslinking of polymers of intrinsic microporosity towards tunable molecular sieve membranes, *Nat. Commun.*, 5 (2014).
- [28] M. Kiyono, P.J. Williams, W.J. Koros, Effect of polymer precursors on carbon molecular sieve structure and separation performance properties, *Carbon*, 48 (2010) 4432-4441.
- [29] P.S. Tin, Y. Xiao, T.S. Chung, Polyimide - carbonized membranes for gas separation: Structural, composition, and morphological control of precursors, *Sep. Purif. Rev.*, 35 (2006) 285-318.
- [30] Y. Xiao, T.-S. Chung, M.L. Chng, S. Tamai, A. Yamaguchi, Structure and properties relationships for aromatic polyimides and their derived carbon membranes: experimental and simulation approaches, *J. Phys. Chem. B*, 109 (2005) 18741-18748.
- [31] S.M. Saufi, A.F. Ismail, Fabrication of carbon membranes for gas separation—a review, *Carbon*, 42 (2004) 241-259.
- [32] M. Inagaki, N. Ohta, Y. Hishiyama, Aromatic polyimides as carbon precursors, *Carbon*, 61 (2013) 1-21.
- [33] M. Yoshimune, K. Mizoguchi, K. Haraya, Alcohol dehydration by pervaporation using a carbon hollow fiber membrane derived from sulfonated poly(phenylene oxide), *J. Membr. Sci.*, 425–426 (2013) 149-155.
- [34] M. Mulder, *Basic principles of membrane technology*, Kluwer, Dordrecht, 1991.
- [35] I. Menendez, A.B. Fuertes, Aging of carbon membranes under different environments, *Carbon*, 39 (2001) 733-740.
- [36] A.B. Fuertes, I. Menendez, Separation of hydrocarbon gas mixtures using phenolic resin-based carbon membranes, *Sep. Purif. Technol.*, 28 (2002) 29-41.
- [37] J.-i. Hayashi, H. Mizuta, M. Yamamoto, K. Kusakabe, S. Morooka, S.-H. Suh, Separation of ethane/ethylene and propane/propylene systems with a carbonized BPDA–pp‘ODA polyimide membrane, *Ind. Eng. Chem. Res.*, 35 (1996) 4176-4181.
- [38] K.-i. Okamoto, S. Kawamura, M. Yoshino, H. Kita, Y. Hirayama, N. Tanihara, Y. Kusuki, Olefin/paraffin separation through carbonized membranes derived from an asymmetric polyimide hollow fiber membrane, *Ind. Eng. Chem. Res.*, 38 (1999) 4424-4432.
- [39] H. Suda, K. Haraya, Alkene/alkane permselectivities of a carbon molecular sieve membrane, *Chem. Commun.*, (1997) 93-94.
- [40] M. Yamamoto, K. Kusakabe, J.-i. Hayashi, S. Morooka, Carbon molecular sieve membrane formed by oxidative carbonization of a copolyimide film coated on a porous support tube, *J. Membr. Sci.*, 133 (1997) 195-205.

- [41] M. Rungta, L. Xu, W.J. Koros, Carbon molecular sieve dense film membranes derived from Matrimid® for ethylene/ethane separation, *Carbon*, 50 (2012) 1488-1502.
- [42] L. Xu, M. Rungta, W.J. Koros, Matrimid® derived carbon molecular sieve hollow fiber membranes for ethylene/ethane separation, *J. Membr. Sci.*, 380 (2011) 138-147.
- [43] X. Ma, R. Swaidan, Y. Belmabkhout, Y. Zhu, E. Litwiller, M. Jouiad, I. Pinnau, Y. Han, Synthesis and gas transport properties of hydroxyl-functionalized polyimides with intrinsic microporosity, *Macromolecules*, 45 (2012) 3841-3849.
- [44] B.S. Ghanem, N.B. McKeown, P.M. Budd, N.M. Al-Harbi, D. Fritsch, K. Heinrich, L. Starannikova, A. Tokarev, Y. Yampolskii, Synthesis, characterization, and gas permeation properties of a novel group of polymers with intrinsic microporosity: PIM-polyimides, *Macromolecules*, 42 (2009) 7881-7888.
- [45] R. Swaidan, X. Ma, E. Litwiller, I. Pinnau, High pressure pure- and mixed-gas separation of CO<sub>2</sub>/CH<sub>4</sub> by thermally-rearranged and carbon molecular sieve membranes derived from a polyimide of intrinsic microporosity, *J. Membr. Sci.*, 447 (2013) 387-394.
- [46] R. Swaidan, B. Ghanem, E. Litwiller, I. Pinnau, Effects of hydroxyl-functionalization and sub-T<sub>g</sub> thermal annealing on high pressure pure- and mixed-gas CO<sub>2</sub>/CH<sub>4</sub> separation by polyimide membranes based on 6FDA and triptycene-containing dianhydrides, *J. Membr. Sci.*, 475 (2015) 571-581.
- [47] R.J. Swaidan, X. Ma, E. Litwiller, I. Pinnau, Enhanced propylene/propane separation by thermal annealing of an intrinsically microporous hydroxyl-functionalized polyimide membrane, *J. Membr. Sci.*, 495 (2015) 235-241.
- [48] X. Ma, R. Swaidan, B. Teng, H. Tan, O. Salinas, E. Litwiller, Y. Han, I. Pinnau, Carbon molecular sieve gas separation membranes based on an intrinsically microporous polyimide precursor, *Carbon*, 62 (2013) 88-96.
- [49] S. Li, H.J. Jo, S.H. Han, C.H. Park, S. Kim, P.M. Budd, Y.M. Lee, Mechanically robust thermally rearranged (TR) polymer membranes with spirobisindane for gas separation, *J. Membr. Sci.*, 434 (2013) 137-147.
- [50] A.C. Ferrari, J. Robertson, Resonant Raman spectroscopy of disordered, amorphous, and diamondlike carbon, *Phys. Rev. B*, 64 (2001) 075414.
- [51] L. Shao, T.-S. Chung, K.P. Pramoda, The evolution of physicochemical and transport properties of 6FDA-durene toward carbon membranes; from polymer, intermediate to carbon, *Microporous Mesoporous Mater.*, 84 (2005) 59-68.
- [52] M.C. Campo, F.D. Magalhães, A. Mendes, Comparative study between a CMS membrane and a CMS adsorbent: part I—Morphology, adsorption equilibrium and kinetics, *J. Membr. Sci.*, 346 (2010) 15-25.
- [53] K.M. Steel, W.J. Koros, Investigation of porosity of carbon materials and related effects on gas separation properties, *Carbon*, 41 (2003) 253-266.

## Chapter 7

### **Fine-Tuning Ultramicroporosity of a Carbon Molecular Sieve Membrane from a Spirobisindane-Containing Microporous Polyimide for Enhanced Ethylene/Ethane Selectivity**

Ethylene is typically produced by steam cracking of various hydrocarbon feedstocks. The gaseous products are then separated in a demethanizer followed by a deethanizer unit and finally send to a C<sub>2</sub> splitter for the final purification step. Cryogenic distillation of ethylene from ethane is the most energy-intensive unit operation process in the chemical industry. Therefore, development of more energy-efficient processes for ethylene purification are highly desirable. Membrane-based separation has been proposed as an alternative option for replacement or debottlenecking of C<sub>2</sub> splitters but current polymer membrane materials exhibit insufficient mixed-gas C<sub>2</sub>H<sub>4</sub>/C<sub>2</sub>H<sub>6</sub> selectivity (< 5) to be technically and economically attractive. In this paper, a highly selective carbon molecular sieve (CMS) membrane derived from a spirobisindane-based polyimide of intrinsic microporosity (PIM-6FDA) was developed and characterized. PIM-6FDA showed a single degradation stage under inert nitrogen atmosphere which commenced at ~480 °C, confirming the cleavage of its polyimide structure. At 500 °C, the CMS obtained from PIM-6FDA formed pores in the 4 to 6.4 Å range, which according to XRD spectra sintered into 3.6 Å cavities after 800 °C heat treatment. The resulting pseudo-graphitic PIM-6FDA structure had a diffusion/size-sieving-controlled morphology with up to now unmatched pure-gas transport properties for a solution/diffusion-based membrane material

( $P_{C_2H_4} = 3.0$  Barrer,  $\alpha_{C_2H_4/C_2H_6} = 25$  measured at 35 °C and 2 bar). Mixed-gas (50%  $C_2H_4$ /50%  $C_2H_6$ ) permeation results showed reduced ethylene/ethane CMS membrane performance. The mixed-gas ethylene/ethane selectivity dropped only slightly from 18 at 4 bar to 15.6 at 20 bar feed pressure due to a subtle CMS dilation as evidenced by the rise in the permeability of both hydrocarbons. Notwithstanding, the mixed-gas ethylene/ethane selectivity is the highest reported for CMS-type membranes to date.

---

<sup>1</sup>Adapted from manuscript submitted to Journal of Materials Chemistry A

## 7.1 Introduction

Ethylene is produced in larger quantity than any other organic compound with a world-wide production of 141 million tons in 2011 [1]. Most commonly, ethylene is produced by steam cracking of hydrocarbon-based feedstock, such as naphtha, ethane etc., which is the most energy-intensive process in the chemical process industry. After cracking, hydrogen and methane are first removed in a demethanizer unit and the dried hydrocarbon feed is then send to a deethanizer to split the C<sub>2</sub> from C<sub>3+</sub> hydrocarbons. In the final process step, ethylene and ethane are separated in a highly energy-intensive cryogenic distillation C<sub>2</sub> splitter. The required distillations columns operate typically at 20 bar and ~ -20 °C, are often more than 100 m tall and contain over 200 trays. The total world energy consumption for ethylene production was about 2-3 EJ (1 EJ = 1 x 10<sup>18</sup> J) in 2004 [1]. Therefore, alternative unit operation processes, such as membrane technology, which may require less energy input for efficient ethylene/ethane separation are highly desirable [2]. Recent process modeling suggested that a membrane/distillation hybrid process to debottleneck ethylene/ethane distillation units could potentially save energy [3-5], provided that a membrane material has high ethylene/ethane selectivity of  $\geq 10$  and withstands realistic process conditions [4, 6].

Currently available commercial membrane materials used for gas separation applications mainly comprise low-free-volume, solution-processable, glassy polymers, which exhibit an inverse relationship between permeability and selectivity [7, 8]. In 2002, Fuertes and Menendez reported the upper bound for the ethylene/ethane system [9], which was updated in 2013 by Rungta and Koros [10].

To date, the best performing polymers offer pure-gas ethylene/ethane selectivities of only  $\sim 7$ , when tested at low feed pressures. Under high pressure mixed-gas conditions (i.e. high hydrocarbon activity) penetrant-induced plasticization and competitive sorption typically causes even lower selectivity [11].

Recently, polymers of intrinsic microporosity (PIMs) were introduced as potential membrane materials for various gas separation applications [12-18]. PIMs are characterized by high BET surface area (up to  $1000 \text{ m}^2/\text{g}$ ) with micropores of less than 2 nm. Optimized PIM polymers have a large free volume fraction of ultramicropores of less than  $7 \text{ \AA}$ , which can discriminate between gases with small differences in molecular dimensions and some types have significantly surpassed previously reported 2008 polymeric upper bound performance for air and hydrogen separations [19]. So far, pure-gas ethylene/ethane separation performance of PIM-materials has only been reported for PIM-1,

**Fig. 7.1a**, and PIM-6FDA-OH,

**Fig. 7.1b**, [20], which offered poor selectivity of less than 4. On the other hand, ultramicroporous carbon molecular sieve (CMS) membranes derived from Matrimid® polyimide [21], PIM-6FDA-OH [22, 23] and PIM-1 [24] precursors have demonstrated promising gas separation performance for ethylene/ethane separation. For example, a CMS membrane formed by pyrolysis of PIM-6FDA-OH at  $800 \text{ }^\circ\text{C}$  showed a mixed-gas ethylene/ethane selectivity ranging from 14 to 8.3 at 4 and 20 bar feed pressure, respectively [23].

CMS membranes comprise a disordered array of stacked graphene sheets generated from thermally degraded polymeric matrices [25, 26]. Fundamentally, the

formation of size-sieving ultramicropores in CMS membranes is determined by a series of complex reactions (e.g. cyclization, dehydrogenation, crosslinking, and oxidation) during the pyrolysis of the polymer precursor structure [27]. The evolution of the pore size distribution (PSD) during the pyrolysis protocol is a strong function of the polymer precursor structure itself [28-30]. Functional groups, such as -OH and -COOH, can lead to potential reactions during the various stages of the pyrolysis process. In general, heat-reactive segments of a polymer chain may create voids left by evolved molecules [31, 32] or may form crosslinks to produce a tighter final CMS structure [33-35]. Recently, the prototype ladder polymer of intrinsic microporosity, PIM-1, carbonized at 800 °C resulted in significant densification of its resulting CMS structure with a dominant crosslinking/sintering effect. As a result, the ethylene permeability of the CMS decreased by 1000-fold compared to its pristine value but the pure-gas selectivity over ethane increased by 7-fold from 1.8 to 13 [24]. In another study, a CMS membrane derived from a hydroxyl-functionalized PIM polyimide at 800 °C, PIM-6FDA-OH, showed an ideal pure-gas C<sub>2</sub>H<sub>4</sub>/C<sub>2</sub>H<sub>6</sub> selectivity of ~ 18 measured at 2 bar [23]. When tested under mixed-gas conditions, the selectivity dropped to ~ 8.3 at a feed pressure of 20 bar and 35 °C. The CMS precursor polyimide, PIM-6FDA-OH, contained hydroxyl groups in ortho position to the imide linkages. Consequently, its pyrolysis process proceeded in three major stages: (i) transformation of the *o*-OH-functionalized polyimide to the corresponding polybenzoxazole (PBO) by thermal rearrangement at ~ 400 °C,

**Fig. 7.1c** – in this step, an opening of the micropore structure was observed with an increase in gas permeability and decrease in selectivity [36-39]; (ii) partial



carbonization of the PBO from 500-600 °C, characterized by large pore modification [28, 40]; (iii) development of an amorphous, ultramicroporous carbon structure from 600-800 °C with further decrease in pore size and permeability but significant increase in selectivity [23].



**Fig. 7.1d**, was used for fine-tuning of the morphology of high-performance CMS membranes for C<sub>2</sub>H<sub>4</sub>/C<sub>2</sub>H<sub>6</sub> separation. The ethylene/ethane transport properties of the PIM-6FDA-derived CMS membranes were evaluated to assess the role of the hydroxyl groups and intermediate PBO formation to the degradation route towards final CMS formation at 800 °C. Pure- and mixed-gas transport tests were conducted with an equimolar feed up to 20 bar and 35 °C for the 800 °C CMS derived from PIM-6FDA to determine potential non-idealities that could affect its industrial applicability.

## 7.2 *Physical properties and carbonization of PIM-6FDA*

The molecular weight ( $M_n$ ) of PIM-6FDA was  $\sim 6 \times 10^4$  g mol<sup>-1</sup> with a *PDI* of 2.85. The PIM-6FDA film annealed at 250 °C had a density of 1.24 g cm<sup>-3</sup>, which was slightly lower than that of its hydroxyl-functionalized analog PIM-6FDA-OH ( $\rho = 1.28$  g cm<sup>-3</sup>) annealed under the same conditions (**Table 7.1**). The degradation profiles of PIM-6FDA and its hydroxyl-functionalized analog PIM-6FDA-OH as a function of temperature are distinctively different, as shown in **Fig. 7.2a**. PIM-6FDA remained in its polymeric glassy state prior to the onset of carbonization above 500 °C according to the gain in Raman sensitivity of the membranes (**Fig. 7.3**). The onset of degradation in PIM-6FDA commenced at  $\sim 480$  °C and its backbone decomposed in a single stage that reached a maximum rate at  $\sim 550$  °C with H<sub>2</sub>O and CO<sub>2</sub> as the main decomposition products. The PIM-6FDA membranes heated at 500 °C suffered a significant 23% weight loss after a 30 min isothermal soak (**Fig. 7.4**). This

degradation stage can be attributed to the cleavage of the polyimide rings and the creation of polar segments in the vestigial chains via free radicals mechanism. The decrease in the infrared spectra intensity confirmed the elimination of most methyl, carbonyl, and hexafluoroisopropylidene moieties as the samples were treated at higher temperatures (**Fig. 7.5**).

On the other hand, PIM-6FDA-OH showed a lower onset of degradation temperature of  $\sim 350$  °C, and more importantly, its degradation profile proceeded in two stages. In the first stage, between 400-450 °C the polyimide was thermally converted to a polybenzoxazole, as previously reported for a wide variety of polyimides bearing an ortho-hydroxyl group adjacent to the imide linkage [41-44]. This stage is characterized by the evolution of CO<sub>2</sub> as a reaction byproduct, as clearly shown in **Fig. 7.2b**. In the second stage, at temperatures higher than 500 °C, amorphous carbon is formed by main chain degradation as evidenced by the evolution of water.

**Table 7.1.** Bulk density and internal surface area of the spirobisindane-based polyimides and its heat-treated derivatives.

Treatment Temperature (°C)	Bulk density <sup>a</sup> (g cm <sup>-3</sup> )		Cumulative <sup>b</sup> NLDFT area (m <sup>2</sup> g <sup>-1</sup> )	
	PIM-6FDA	PIM-6FDA-OH	PIM-6FDA	PIM-6FDA-OH
	250	1.24	1.28	146
400	1.24	1.18	146	145
500	1.21	1.20	340	334

600	1.31	1.32	410	470
800	1.53	1.50	775	760

<sup>a</sup>Measured gravimetrically,  $\rho=(\text{weight of sample}) (\text{volume})^{-1}$ . Error= 1%

<sup>b</sup>Total surface area of pores smaller than 7.2 Å according to the NLDFT method.

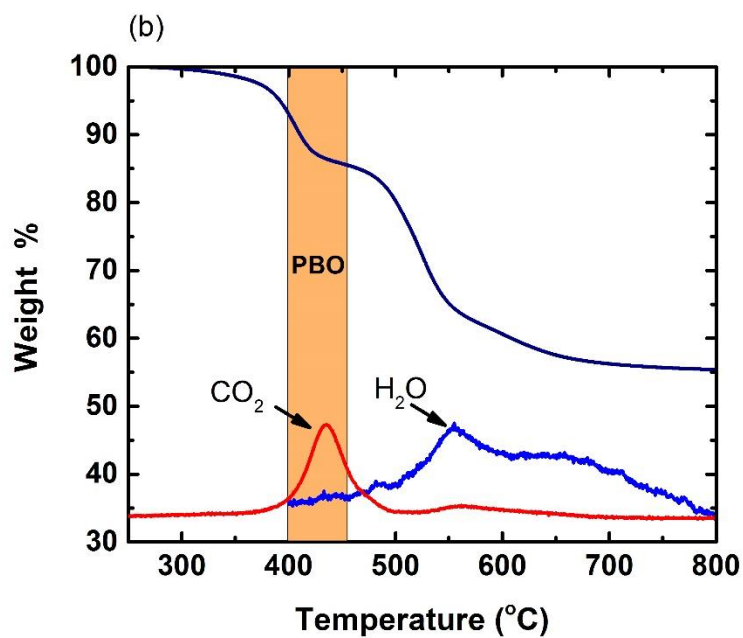
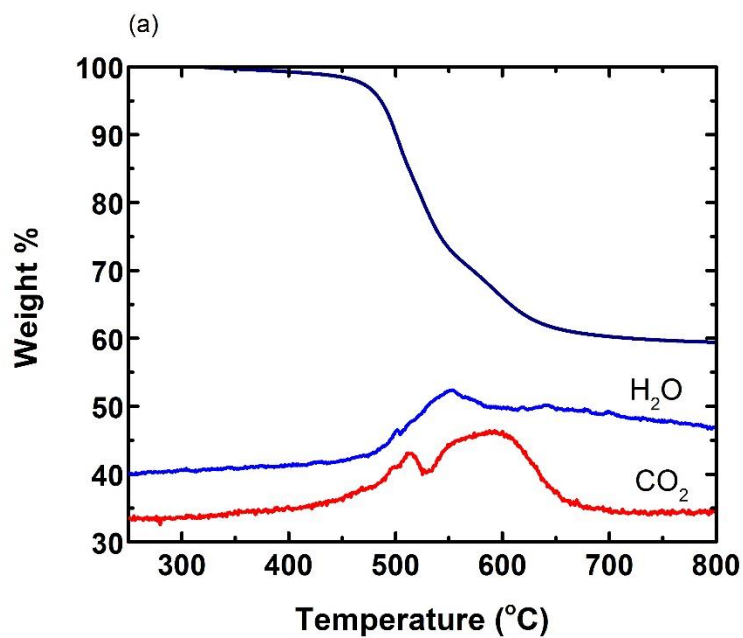


**Fig. 7.2.** Weight loss and mass spectra of evolved gases during the degradation of a) PIM-6FDA and b) PIM-6FDA-OH. Ramping rate 3 °C/min under N<sub>2</sub> atmosphere.

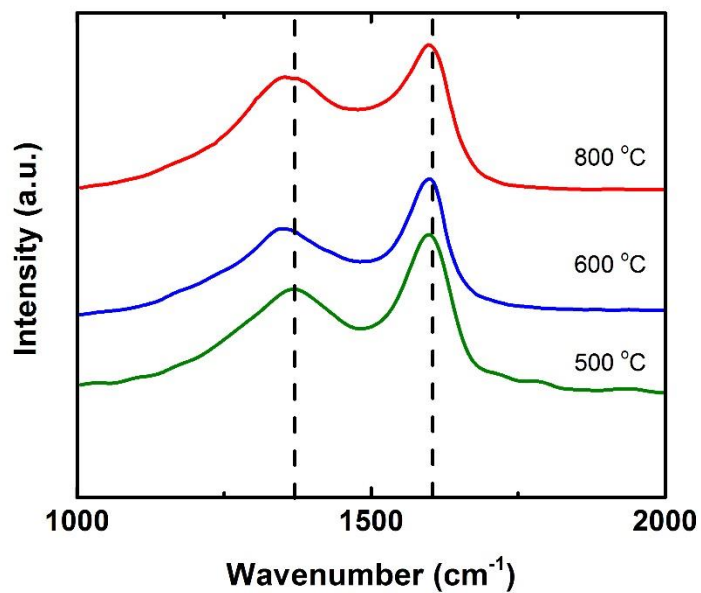


**Fig. 7.3.** Raman spectra of CMS generated from PIM-6FDA at 500, 600 and 800 °C. D and G peaks indicate amorphous graphene configurations are marked with dashed lines.

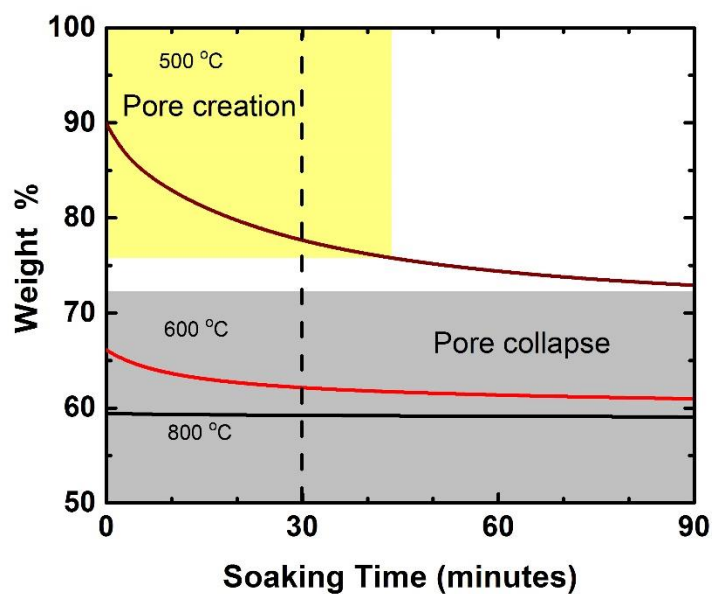


**Fig. 7.4.** Weight loss of PIM-6FDA for each isothermal stage of carbonization. Shaded areas show the dominating porosity evolution mechanisms during heat treatment while the dashed line was the actual soak time used in the pyrolysis protocol.

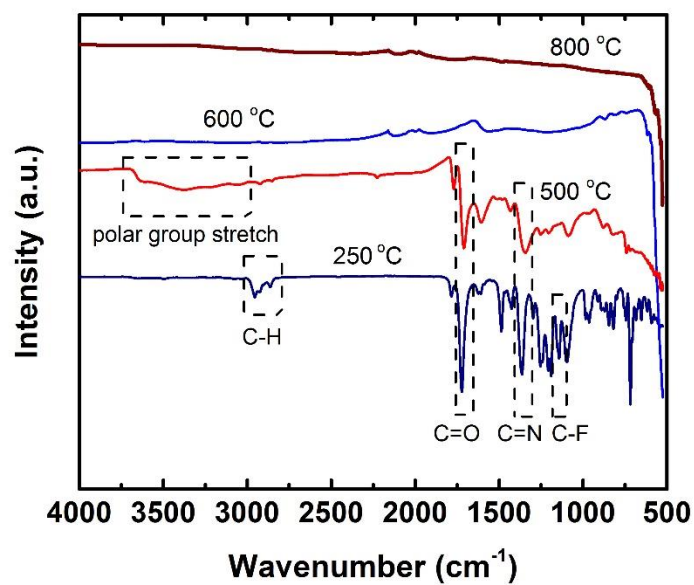


**Fig. 7.5.** FTIR spectra of PIM-6FDA and derived CMS membranes at 500, 600 and 800 °C.

The carbonization process caused an enhancement in the ultramicroporosity of the membranes as clearly shown in the XRD spectra in **Fig. 7.6**. In the first stage of PIM-6FDA pyrolysis at 500°C, the partially degraded polymer formed a fraction of larger pores (4-6.4 Å), as indicated by the significant broadening of the amorphous peak of the pristine polyimide. This result is consistent with an increase in ethylene permeability and drop in ethylene/ethane selectivity, as discussed below. At 600 °C, a bimodal ultramicroporous distribution was observed. The spectra show two distinctive peaks: the first represents the bulk distance between the unaligned graphene layers (i.e. 4.0 Å at 600 °C), and the second is related to the appearance of the (1 0 0) graphene plane [28].

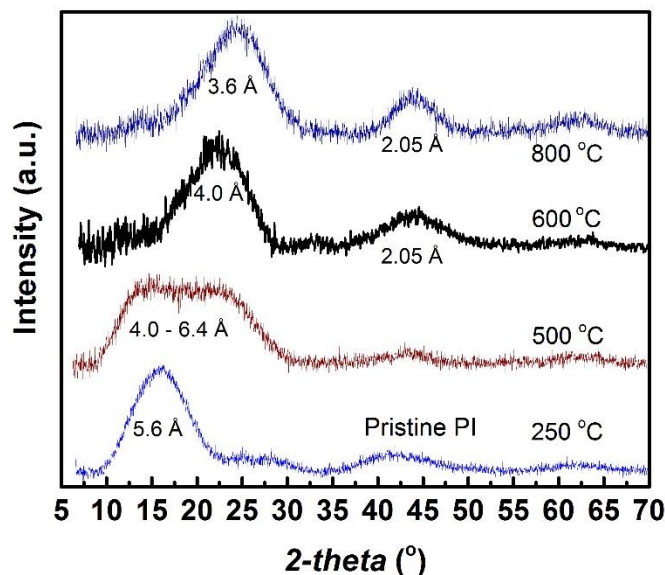


**Fig. 7.6.** XRD spectra of PIM-6FDA (pristine PI) and CMS membranes for each isothermal stage of carbonization.



Samples treated at 800 °C did not suffer significant additional losses in weight, indicating that those membranes are mainly comprised of a honeycomb-arranged carbon skeleton with no thermally liable groups. The final residual weight after treating PIM-6FDA at 800 °C was 59% which is 4% higher than that of PIM-6FDA-OH carbonized at the same temperature [23]. Most importantly, the PIM-6FDA-based carbon generated at 800 °C had a d-spacing of 3.6 Å, which was 0.15 Å smaller than that of its CMS membrane made from the hydroxyl-functionalized PIM-6FDA-OH pyrolyzed at the same temperature [23]. From this evidence, it is suggested that the CMS membranes derived from PIM-6FDA were more susceptible to thermally induced porosity modifications compared to carbons obtained from their analog PIM-6FDA-OH. Notably, the pores created in PIM-6FDA at 500 °C were larger and more widely distributed than those created in PIM-6FDA-OH during the same heating protocol. Conversely, the pore collapse at 800 °C produced a more tightly sintered (i.e. smaller-sized cavities) carbon matrix from PIM-6FDA.

### 7.3 *CO<sub>2</sub> sorption for PSD estimation*

CO<sub>2</sub> sorption was used to assess the ultramicroporous domains found in the carbons derived from PIM-6FDA via the NLDFT method. As distinctive as in other PIM materials, there was an abrupt CO<sub>2</sub> uptake for relative pressures less than 10<sup>-3</sup>, as shown in **Fig. 7.7**.

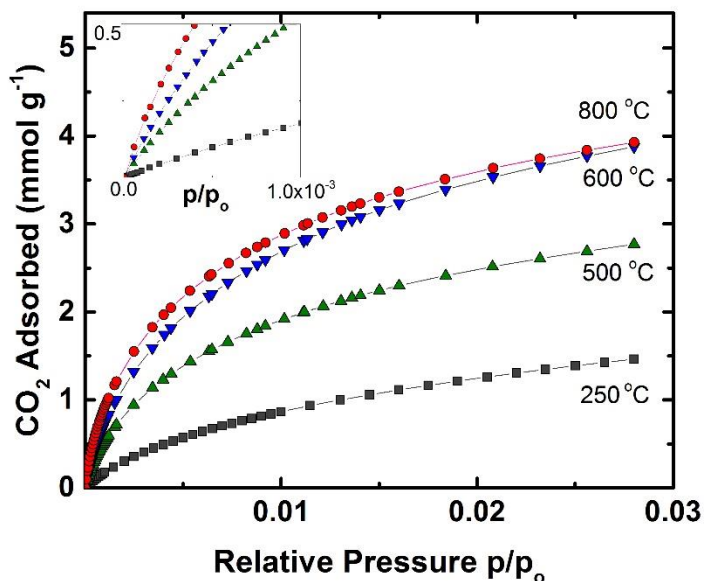


**Fig. 7.7.** Physisorption of CO<sub>2</sub> at 0 °C in PIM-6FDA and its heat-derived CMS membranes. Low-pressure sorption is shown in the upper left corner of the graph.

Furthermore, pyrolysis of PIM-6FDA above 500 °C created a significant fraction of ultramicroporous cavities that provided additional internal surface area for gas sorption. At a relative pressure of 0.028, the CO<sub>2</sub> sorption capacity increased stepwise from 1.5 mmol g<sup>-1</sup> for the pristine PIM-6FDA to 2.7 mmol g<sup>-1</sup> for the 500 °C CMS. The CO<sub>2</sub> uptake further increased to its highest value of ~4 mmol g<sup>-1</sup> for both 600 and 800 °C treated CMS membranes.

The PSD obtained from CO<sub>2</sub> sorption at 0 °C is shown in **Fig. 7.8**. A clear trimodal ultramicroporous distribution was detected in samples that were produced at 500 °C or above. The sharp increase in the fraction of ~3.6 Å pores is correlated with the rise of ultramicroporosity due to cavity sintering during the carbonization process (i.e. also observed in the XRD spectra). The weaker peaks at ~4.8 Å and

~5.7 Å also gained intensity as the carbonization proceeded further. This *qualitative* methodology tracked a definite improvement in the ultramicroporous characteristics of the PIM-6FDA films after the thermal treatment, and consequently, their molecular sieving capabilities. However, the NLDFT PSD between CMS membranes derived from PIM-6FDA and PIM-6FDA-OH showed very subtle differences. It has been suggested that this method may not be sensitive enough to distinguish porosities obtained from similar precursors [29].

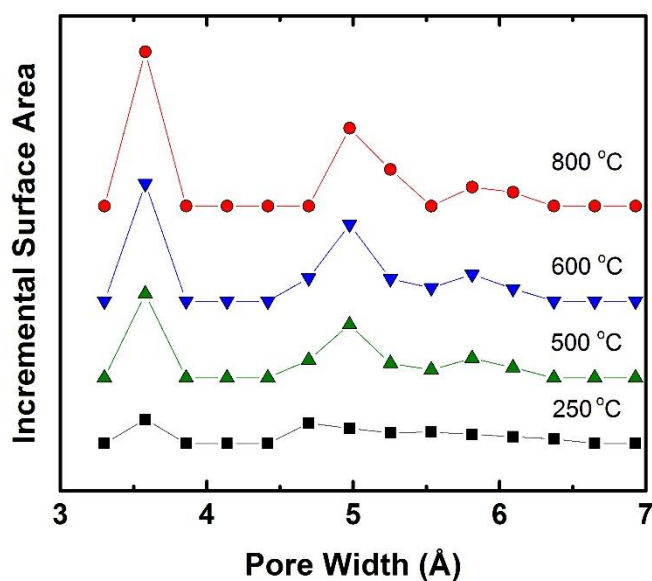


**Fig. 7.8.** PSD of 250 °C annealed PIM-6FDA and CMS samples heat-treated at 500, 600 and 800 °C.

Ethylene and ethane sorption measurements were carried out on PIM-6FDA and its CMS films using a gravimetric method at 35°C. The films were dried in a vacuum oven at 120 °C for at least 12 hrs prior to testing to remove any moisture.

The sample cell was then evacuated for 1 day prior to testing and evacuated for 24 hrs after completion of each gas isotherm. The pure-gas sorption results for ethylene and ethane are shown in **Fig. 7.9**. The “dual-mode” sorption model with both Langmuir (hole filling) and Henry's law (dissolution) contributions is apparent for PIM-6FDA in the concave sorption isotherms. The sorption data were then fitted using the least-squares method to determine the dual-mode sorption parameters for each sorption isotherm.

The CMS membrane sorption isotherms followed Langmuir behavior with higher ethylene and ethane sorption capacity than their PIM-6FDA polyimide precursor. The strong Langmuir behavior was promoted by increasingly higher carbonization temperatures due to the formation of ultramicroporous vacancies, in agreement with the *qualitative* evolution of the porosity described before. It is of utmost importance to point out that the sorption uptake of either hydrocarbon was very similar for each sample, that is, the  $C_2H_4/C_2H_6$  solubility selectivity was essentially 1. Hence, the permselectivity of the CMS membranes was *completely* controlled by their diffusivity selectivity.

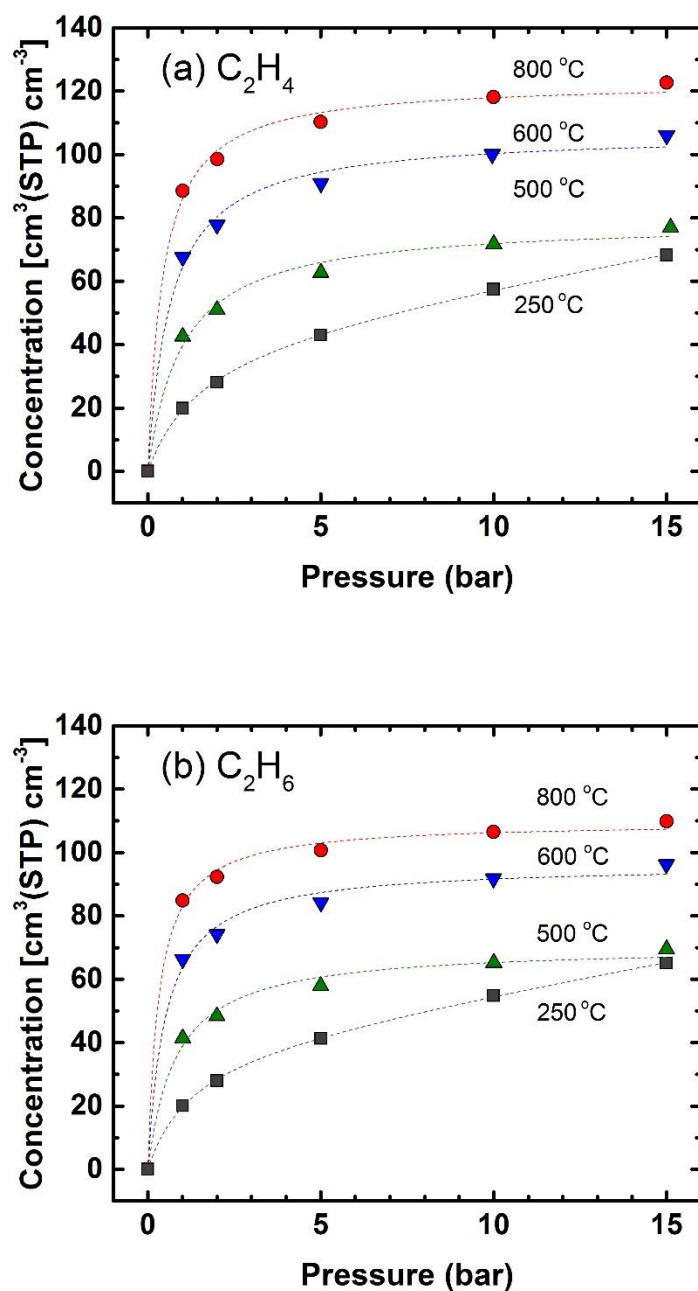


**Fig. 7.9.** Pure-gas sorption isotherms of (a) ethylene and (b) ethane at 35 °C in PIM-6FDA and its CMS derivatives. Fitted dashed curves follow the dual-mode sorption model for the polymeric PIM-PI annealed at 250 °C, whereas the Langmuir model was used to describe sorption in the CMS samples.

The parameters of the fitted sorption models are summarized in **Table 7.2**. The overall trend indicated an increase in  $C'_H$  and  $b$  with increasing treatment temperature. For example, ethylene  $C'_H$  of the 800 °C-treated film had a value of 123 cm<sup>3</sup>(STP) cm<sup>-3</sup>, three times higher than the  $C'_H$  value of the original polymeric PIM-6FDA precursor annealed at 250 °C. This result is consistent with the enhanced CO<sub>2</sub> sorption uptake of carbonized PIM-6FDA, as also evidenced by low-pressure CO<sub>2</sub> sorption experiments performed at 0 °C, as shown in **Fig. 7.7**.

**Table 7.2.** Parameters obtained from fitting experimental data to the dual-mode (pristine PIM-6FDA) and the Langmuir isotherms for CMS membranes. <sup>a</sup>

Membrane type	C <sub>2</sub> H <sub>4</sub>			C <sub>2</sub> H <sub>6</sub>		
	$K_d$	$C'_H$	$b$	$K_d$	$C'_H$	$b$
PIM-6FDA 250 °C	2.57	43.5	0.9	2.54	39.7	1.1
CMS 500 °C		79.0	1.3		70.6	1.6
CMS 600 °C		106.9	2.0		96.3	2.6
CMS 800 °C		123.0	3.1		109.6	4.2

<sup>a</sup>  $K_d$  [10<sup>-2</sup> cm<sup>3</sup>(STP) cm<sup>-3</sup> cmHg<sup>-1</sup>];  $C'_H$  [cm<sup>3</sup>(STP) cm<sup>-3</sup>];  $b$  [10<sup>-2</sup> cmHg<sup>-1</sup>]

#### 7.4 Ethylene/ethane pure-gas permeation properties

The pure-gas ethylene and ethane permeation properties of the thermally annealed PIM-6FDA film and its pyrolyzed CMS derivatives were determined at 2 bar and 35 °C (Fig. 7). The diffusion and solubility coefficients and selectivities are

shown in Table S2. The 250 °C-heat-treated PIM-6FDA film showed a pure-gas ethylene/ethane permselectivity of 3.6 and an ethylene permeability of 7 Barrer. After partial degradation of the polymer backbone at 500 °C, the ethylene permeability of the CMS membrane increased by a factor of 40 to 328 Barrer mainly due to the generation of new pores and pore opening in the range of 4.6-6.4 Å (**Fig. 7.6** and **Fig. 7.8**) but selectivity decreased from 3.6 to 2.1. The formation of microporous vacancies during the early stages of carbonization caused the significant enhancement in permeability right after the long-range polymeric structure was lost to main backbone reactions. Heat treatment at higher temperatures reduced permeability, as a result of the pore contraction confirmed by XRD and CO<sub>2</sub> sorption tests. From 600 to 800 °C, ethylene permeability decreased significantly from 79 to 3.0 Barrer. All samples treated at temperatures above 600 °C surpassed the polymeric ethylene/ethane upper bound (**Fig. 7.10**). For a PIM-6FDA-derived CMS membrane at 800 °C, a pure-gas ethylene/ethane selectivity of 25 was reached, which is the highest value reported to date for any CMS membrane type.

The CMS of the previously reported hydroxyl-functionalized PIM-6FDA-OH generated at 800 °C had an ethylene permeability of 10.6 Barrer and C<sub>2</sub>H<sub>4</sub>/C<sub>2</sub>H<sub>6</sub> selectivity of ~18 [23]. It is suggested that the microporous CMS morphology created after carbonization of PIM-6FDA at 800 °C formed tighter, more size-sieving ultramicroporous cavities than formed in the CMS membrane derived from PIM-6FDA-OH. It may be hypothesized that the polybenzoxazole intermediate generated from PIM-6FDA-OH at ~400-450 °C possessed relatively thermally

stable voids that partially hindered the sintering mechanism at the higher temperature carbonization stages.

**Table 7.3.** Pure-gas transport properties at 35 °C and 2 bar driving-force for heat-treated PIM-6FDA and its CMS samples.

Treatment temperature (°C)	Permeability (Barrer)		$\alpha_P$ (-)	Solubility <sup>a</sup> (cm <sup>3</sup> cm <sup>-3</sup> cmHg <sup>-1</sup> )		$\alpha_S$ (-)	Diffusivity <sup>b</sup> 10 <sup>-10</sup> * (cm <sup>2</sup> s <sup>-1</sup> )		$\alpha_D$ (-)
	C <sub>2</sub> H <sub>4</sub>	C <sub>2</sub> H <sub>6</sub>	(-)	C <sub>2</sub> H <sub>4</sub>	C <sub>2</sub> H <sub>6</sub>	(-)	C <sub>2</sub> H <sub>4</sub>	C <sub>2</sub> H <sub>6</sub>	(-)
250	7.9	2.19	3.6	0.19	0.19	1.00	42	11.5	3.7
400	8.5	2.18	3.9	0.19	0.19	1.00	47	11.9	3.9
500	328	156	2.1	0.34	0.32	1.05	970	490.5	2
600	77	18.8	4.1	0.52	0.50	1.04	150	38.0	3.9
800	3.0	0.12	25.0	0.66	0.62	1.06	4.57	0.194	23.5

<sup>a</sup> Average solubility calculated from the gravimetric sorption uptake at 2 bar

<sup>b</sup> Average diffusion coefficient calculated from  $D = P S^{-1}$

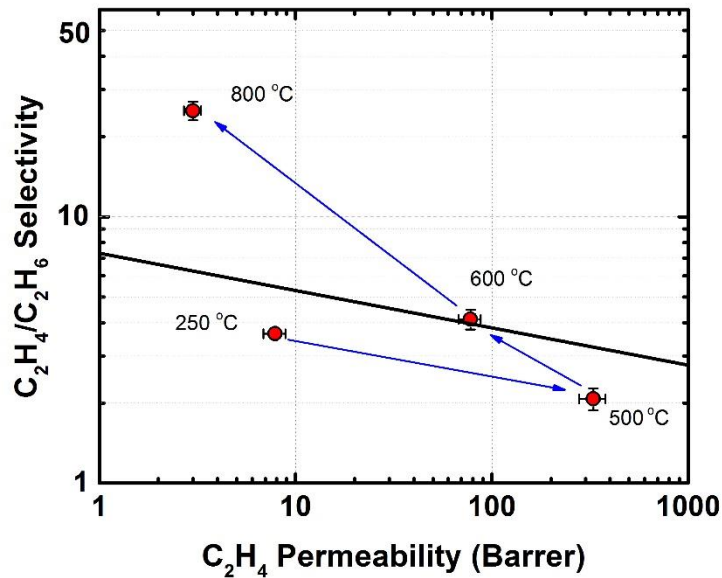




**Fig. 7.10.** Pure-gas ethylene/ethane permeation properties of CMS membranes derived from PIM-6FDA (2 bar; 35 °C). The polymer upper bound is represented with the bold black line [10].

### 7.5 *Mixed-gas permeability and selectivity of the 800 °C CMS membrane*

The PIM-6FDA sample carbonized at 800 °C was evaluated with a 50:50 v/v ethylene/ethane mixture as a function of feed pressure and the results are shown in Fig. 8. The overall response to increasing the upstream pressure indicated a small permeability enhancement for both hydrocarbons. Ethylene permeability increased slightly from 3.0 to 3.2 Barrer, whereas ethane permeability increased from 0.167 to 0.205 Barrer over the feed pressure range of 4 to 20 bar. The mixed-gas ethylene/ethane selectivity of the CMS membrane dropped by only 13% from 18 to 15.6 by increasing the feed pressure from 4 to 20 bar. It is important to note that the high-pressure mixed-gas performance for ethylene/ethane separation of the CMS membrane generated at 800 °C from PIM-6FDA is the highest reported to date for all previously reported CMS membranes.

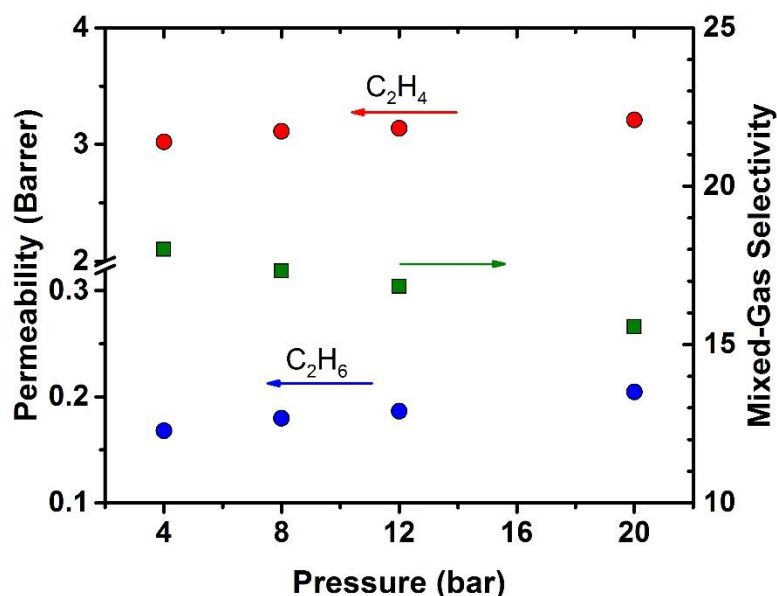


**Fig. 7.11.** Pressure dependence of the mixed-gas permeation properties of 800 °C-treated CMS membranes derived from PIM-6FDA using a 1:1 v/v ethylene/ethane binary mixture at 35 °C.

The time dependence of the mixed-gas permeation experiments is shown in **Fig. 7.12**. In order to reach pseudo steady-state permeation conditions for each feed pressure over the range of 4 to 20 bar it took a total period of about 80 days. This significant time-dependent effect of the physical state of the CMS membrane tested at each pressure point on the mixed-gas permeation properties can be attributed to a small matrix dilation of its smallest ultramicropores. This subtle dilation resulted in the observed small increase in mixed-gas permeability of the two hydrocarbons and a concurrent selectivity drop. This transient behavior observed under mixed-gas ethylene/ethane permeation conditions agreed with previous results for the

ethylene/ethane [23] and CO<sub>2</sub>/CH<sub>4</sub> separation [45] obtained for the 800 °C CMS membrane derived from PIM-6FDA-OH.

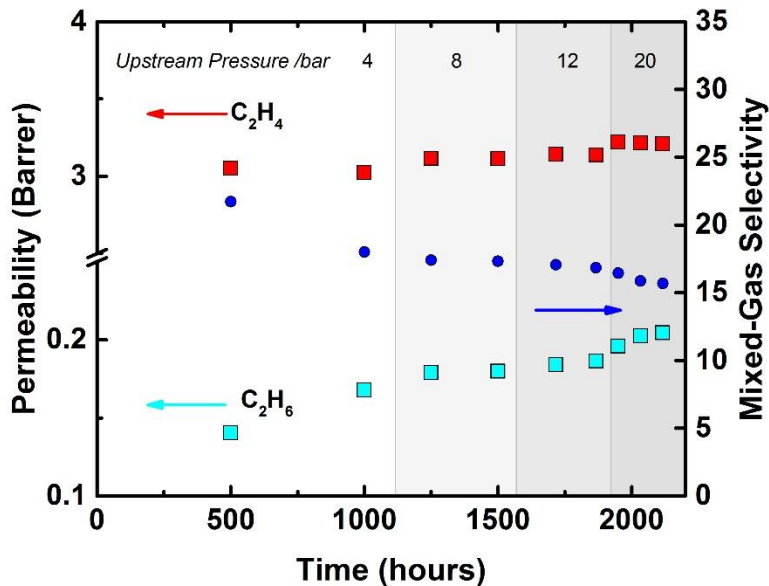


**Fig. 7.12.** Time dependence of the mixed-gas permeation properties of 800 °C-treated CMS membranes derived from PIM-6FDA using a 1:1 v/v ethylene/ethane binary mixture at 35 °C.

## 7.6 Conclusions

In this chapter, a PIM-PI bearing a spiro-center, PIM-6FDA, was employed to generate isotropic CMS membranes with excellent performance for ethylene/ethane separation. This study addressed the role of the: (i) ortho-hydroxyl functionality of the polyimide and (ii) formation of the intermediate PBO on thermally-induced changes in the porosity of the final CMS structure. Carbons derived from PIM-6FDA were compared with those obtained from its hydroxyl-

functionalized analog, PIM-6FDA-OH, with respect to pore size distribution and transport properties. The creation of ultramicroporous vacancies that severely hinder ethane diffusion through the CMS matrix was favored by the single-staged reordering of PIM-6FDA into the pseudo-graphitic CMS structure. The molecular size-exclusion effect dominated the ethylene and ethane transport through the CMS membranes derived from PIM-6FDA. Furthermore, densification of the PIM-6FDA carbonaceous matrix at 800 °C produced a superior ethylene/ethane diffusion-selective effect compared to its hydroxyl-bearing-counterpart-derived CMS. The PIM-6FDA CMS made at 800 °C sintered into a denser structure with smaller and sharper pore size distribution, as confirmed by XRD diffraction and permeation experiments. The CMS derived from PIM-6FDA at 800 °C exhibited a pure-gas selectivity of 25 (measured at 2 bar and 35 °C). Mixed-gas permeation tests using a binary 1:1 v/v ethylene/ethane feed under realistic operating pressures revealed a small performance loss due to a subtle matrix dilation of the selective CMS cavities. Notwithstanding, even the reduced mixed-gas ethylene/ethane selectivity of ~16 measured at 20 bar and 35 °C is the highest value reported to date for any CMS membrane.

## 7.7 References

- [1] T. Ren, M. Patel, K. Blok, Olefins from conventional and heavy feedstocks: energy use in steam cracking and alternative processes, *Energy*, 31 (2006) 425-451.
- [2] W.J. Koros, Evolving beyond the thermal age of separation processes: membranes can lead the way, *AIChE Journal*, 50 (2004) 2326-2334.
- [3] J.A. Caballero, I.E. Grossmann, M. Keyvani, E.S. Lenz, Design of hybrid distillation-vapor membrane separation systems, *Ind. Eng. Chem. Res.*, 48 (2009) 9151-9162.
- [4] A. Motelica, O.S.L. Bruinsma, R. Kreiter, M. den Exter, J.F. Vente, Membrane retrofit option for paraffin/olefin separation—a technoeconomic evaluation, *Ind. Eng. Chem. Res.*, 51 (2012) 6977-6986.
- [5] J. Ploegmakers, A.R.T. Jelsma, A.G.J. van der Ham, K. Nijmeijer, Economic evaluation of membrane potential for ethylene/ethane separation in a retrofitted hybrid membrane-distillation plant using unisim design, *Ind. Eng. Chem. Res.*, 52 (2013) 6524-6539.
- [6] R.W. Baker, B.T. Low, Gas separation membrane materials: a perspective, *Macromolecules*, 47 (2014) 6999-7013.
- [7] L.M. Robeson, Correlation of separation factor versus permeability for polymeric membranes, *J. Membr. Sci.*, 62 (1991) 165-185.
- [8] L.M. Robeson, The upper bound revisited, *J. Membr. Sci.*, 320 (2008) 390-400.
- [9] A.B. Fuertes, I. Menendez, Separation of hydrocarbon gas mixtures using phenolic resin-based carbon membranes, *Sep. Purif. Technol.*, 28 (2002) 29-41.
- [10] M. Rungta, C. Zhang, W.J. Koros, L. Xu, Membrane-based ethylene/ethane separation: the upper bound and beyond, *AIChE Journal*, 59 (2013) 3475-3489.
- [11] C. Staudt-Bickel, W.J. Koros, Olefin/paraffin gas separations with 6FDA-based polyimide membranes, *J. Membr. Sci.*, 170 (2000) 205-214.
- [12] P.M. Budd, K.J. Msayib, C.E. Tattershall, B.S. Ghanem, K.J. Reynolds, N.B. McKeown, D. Fritsch, Gas separation membranes from polymers of intrinsic microporosity, *J. Membr. Sci.*, 251 (2005) 263-269.
- [13] P.M. Budd, N.B. McKeown, D. Fritsch, Polymers of intrinsic microporosity (PIMs): high free volume polymers for membrane applications, *Macromol. Symp.*, 245-246 (2006) 403-405.
- [14] Y. Zhuang, J.G. Seong, Y.S. Do, H.J. Jo, Z. Cui, J. Lee, Y.M. Lee, M.D. Guiver, Intrinsically microporous soluble polyimides incorporating Tröger's base for membrane gas separation, *Macromolecules*, 47 (2014) 3254-3262.

- [15] B.S. Ghanem, R. Swaidan, E. Litwiller, I. Pinnau, Ultra-microporous triptycene-based polyimide membranes for high-performance gas separation, *Adv. Mater.*, 26 (2014) 3688-3692.
- [16] M. Carta, M. Croad, R. Malpass-Evans, J.C. Jansen, P. Bernardo, G. Clarizia, K. Friess, M. Lanč, N.B. McKeown, Triptycene induced enhancement of membrane gas selectivity for microporous Tröger's base polymers, *Adv. Mater.*, 26 (2014) 3526-3531.
- [17] N. Du, H.B. Park, G.P. Robertson, M.M. Dal-Cin, T. Visser, L. Scoles, M.D. Guiver, Polymer nanosieve membranes for CO<sub>2</sub>-capture applications, *Nat. Mater.*, 10 (2011) 372-375.
- [18] P.M. Budd, B.S. Ghanem, S. Makhseed, N.B. McKeown, K.J. Msayib, C.E. Tattershall, Polymers of intrinsic microporosity (PIMs): robust, solution-processable, organic nanoporous materials, *Chem. Commun.*, (2004) 230-231.
- [19] R. Swaidan, B. Ghanem, I. Pinnau, Fine-tuned intrinsically ultramicroporous polymers redefine the permeability/selectivity upper bounds of membrane-based air and hydrogen separations, *ACS Macro Lett.*, 4 (2015) 947-951.
- [20] P. Li, T.S. Chung, D.R. Paul, Gas sorption and permeation in PIM-1, *J. Membr. Sci.*, 432 (2013) 50-57.
- [21] M. Rungta, L. Xu, W.J. Koros, Carbon molecular sieve dense film membranes derived from Matrimid® for ethylene/ethane separation, *Carbon*, 50 (2012) 1488-1502.
- [22] X. Ma, R. Swaidan, B. Teng, H. Tan, O. Salinas, E. Litwiller, Y. Han, I. Pinnau, Carbon molecular sieve gas separation membranes based on an intrinsically microporous polyimide precursor, *Carbon*, 62 (2013) 88-96.
- [23] O. Salinas, X. Ma, E. Litwiller, I. Pinnau, High-performance carbon molecular sieve membranes for ethylene/ethane separation derived from an intrinsically microporous polyimide, *J. Membr. Sci.*, 500 (2016) 115-123.
- [24] O. Salinas, X. Ma, E. Litwiller, I. Pinnau, Ethylene/ethane permeation, diffusion and gas sorption properties of carbon molecular sieve membranes derived from the prototype ladder polymer of intrinsic microporosity (PIM-1), *J. Membr. Sci.*, 504 (2016) 133-140.
- [25] K.M. Steel, W.J. Koros, Investigation of porosity of carbon materials and related effects on gas separation properties, *Carbon*, 41 (2003) 253-266.
- [26] A.J. Bird, D.L. Trimm, Carbon molecular sieves used in gas separation membranes, *Carbon*, 21 (1983) 177-180.
- [27] S.M. Saufi, A.F. Ismail, Fabrication of carbon membranes for gas separation—a review, *Carbon*, 42 (2004) 241-259.
- [28] L. Shao, T.-S. Chung, K.P. Pramoda, The evolution of physicochemical and transport properties of 6FDA-durene toward carbon membranes; from polymer, intermediate to carbon, *Microporous Mesoporous Mater.*, 84 (2005) 59-68.

- [29] S. Fu, E.S. Sanders, S.S. Kulkarni, W.J. Koros, Carbon molecular sieve membrane structure–property relationships for four novel 6FDA based polyimide precursors, *J. Membr. Sci.*, 487 (2015) 60-73.
- [30] M. Inagaki, N. Ohta, Y. Hishiyama, Aromatic polyimides as carbon precursors, *Carbon*, 61 (2013) 1-21.
- [31] H.B. Park, C.H. Jung, Y.M. Lee, A.J. Hill, S.J. Pas, S.T. Mudie, E. Van Wagner, B.D. Freeman, D.J. Cookson, Polymers with cavities tuned for fast selective transport of small molecules and ions, *Science*, 318 (2007) 254-258.
- [32] Y. Jiang, F.T. Willmore, D. Sanders, Z.P. Smith, C.P. Ribeiro, C.M. Doherty, A. Thornton, A.J. Hill, B.D. Freeman, I.C. Sanchez, Cavity size, sorption and transport characteristics of thermally rearranged (TR) polymers, *Polymer*, 52 (2011) 2244-2254.
- [33] J. Weber, N. Du, M.D. Guiver, Influence of intermolecular interactions on the observable porosity in intrinsically microporous polymers, *Macromolecules*, 44 (2011) 1763-1767.
- [34] Q. Song, S. Cao, R.H. Pritchard, B. Ghalei, S.A. Al-Muhtaseb, E.M. Terentjev, A.K. Cheetham, E. Sivaniah, Controlled thermal oxidative crosslinking of polymers of intrinsic microporosity towards tunable molecular sieve membranes, *Nat. Commun.*, 5 (2014).
- [35] K. Vanherck, G. Koeckelberghs, I.F.J. Vankelecom, Crosslinking polyimides for membrane applications: a review, *Prog. Polym. Sci.*, 38 (2013) 874-896.
- [36] S. Li, H.J. Jo, S.H. Han, C.H. Park, S. Kim, P.M. Budd, Y.M. Lee, Mechanically robust thermally rearranged (TR) polymer membranes with spirobisindane for gas separation, *J. Membr. Sci.*, 434 (2013) 137-147.
- [37] X. Ma, O. Salinas, E. Litwiller, I. Pinnau, Pristine and thermally-rearranged gas separation membranes from novel o-hydroxyl-functionalized spirobifluorene-based polyimides, *Polymer Chemistry*, 5 (2014) 6914-6922.
- [38] H. Shamsipur, B.A. Dawood, P.M. Budd, P. Bernardo, G. Clarizia, J.C. Jansen, Thermally rearrangeable PIM-polyimides for gas separation membranes, *Macromolecules*, 47 (2014) 5595-5606.
- [39] D.F. Sanders, R. Guo, Z.P. Smith, K.A. Stevens, Q. Liu, J.E. McGrath, D.R. Paul, B.D. Freeman, Influence of polyimide precursor synthesis route and ortho-position functional group on thermally rearranged (TR) polymer properties: pure gas permeability and selectivity, *J. Membr. Sci.*, 463 (2014) 73-81.
- [40] J.N. Barsema, S.D. Klijnstra, J.H. Balster, N.F.A. van der Vegt, G.H. Koops, M. Wessling, Intermediate polymer to carbon gas separation membranes based on Matrimid PI, *J. Membr. Sci.*, 238 (2004) 93-102.
- [41] D.F. Sanders, Z.P. Smith, C.P. Ribeiro Jr, R. Guo, J.E. McGrath, D.R. Paul, B.D. Freeman, Gas permeability, diffusivity, and free volume of thermally rearranged polymers based on 3,3'-dihydroxy-4,4'-diamino-biphenyl (HAB) and 2,2'-bis-(3,4-

dicarboxyphenyl) hexafluoropropane dianhydride (6FDA), *J. Membr. Sci.*, 409-410 (2012) 232-241.

[42] B. Comesaña-Gándara, A. Hernández, J.G. de la Campa, J. de Abajo, A.E. Lozano, Y.M. Lee, Thermally rearranged polybenzoxazoles and poly(benzoxazole-co-imide)s from ortho-hydroxyamine monomers for high performance gas separation membranes, *J. Membr. Sci.*, 493 (2015) 329-339.

[43] Z.P. Smith, D.F. Sanders, C.P. Ribeiro, R. Guo, B.D. Freeman, D.R. Paul, J.E. McGrath, S. Swinnea, Gas sorption and characterization of thermally rearranged polyimides based on 3,3'-dihydroxy-4,4'-diamino-biphenyl (HAB) and 2,2'-bis-(3,4-dicarboxyphenyl) hexafluoropropane dianhydride (6FDA), *J. Membr. Sci.*, 415-416 (2012) 558-567.

[44] Z.P. Smith, G. Hernández, K.L. Gleason, A. Anand, C.M. Doherty, K. Konstas, C. Alvarez, A.J. Hill, A.E. Lozano, D.R. Paul, B.D. Freeman, Effect of polymer structure on gas transport properties of selected aromatic polyimides, polyamides and TR polymers, *J. Membr. Sci.*, 493 (2015) 766-781.

[45] R. Swaidan, X. Ma, E. Litwiller, I. Pinnau, High pressure pure- and mixed-gas separation of CO<sub>2</sub>/CH<sub>4</sub> by thermally-rearranged and carbon molecular sieve membranes derived from a polyimide of intrinsic microporosity, *J. Membr. Sci.*, 447 (2013) 387-394.



## Chapter 8

### Conclusions and Recommendations

Chapter 4 reported the ethylene/ethane separation properties of nine spiro-based PIMs, while Chapters 5 to 7 analyzed the CMS membranes derived from PIM-1, PIM-6FDA-OH, and PIM-6FDA, respectively. The pristine PIMs studied here did not surpass the known upper bound performance due to limited diffusion selectivities. The pore distribution of these PIMs did not allow for effective ethylene/ethane separation factors (i.e. pure-gas  $\alpha < 6$ , measured at 35 °C and 2 bar of upstream pressure). Nevertheless, insight was obtained on the effect of -OH functionalities, and bromine substitutions on the transport of PIM-polyimides. The tighter and more rigid structure of -OH-bearing PIM-PI sieve ethylene from ethane more efficiently than their unfunctionalized analogues do. As a consequence of this pre-synthetic modification, PMDA-HSBF and PIM-6FDA-OH presented properties akin to those of low free-volume polyimides. This work also provided valuable information on the degradation path of PIMs towards highly selective ethylene/ethane CMS membranes. In spite of their loss in performance when exposed to realistic mixed-gas permeation environments, the CMSs derived from PIMs offered valuable candidates for ethylene/ethane separation that could potentially debottleneck this difficult separation.

### 8.1 PIMs for ethylene/ethane separation

Ethylene/ethane separation is both extremely energy expensive to achieve and done in very large quantities; therefore, an improvement in its operating efficiency should translate into significant savings. Membrane technology is a potential solution since it circumvents the need to apply a thermal phase change by distillation to achieve the required ethylene product purity. However, this application has been severely limited by lack of high-performing, cost-effective materials that could act as a separation layer.

In this work, state-of-the-art PIMs were tested in an effort to screen for the right combination of matrix rigidity and pore size distribution. The PIM matrices bearing spiro centers reported here lacked the pore size and uniformity required to sieve ethylene from ethane efficiently. However, OH-functionalized PIMs were able to attain selectivities comparable to those of low-free-volume glassy polymers. Polymers with small (i.e. in the order of 3.6-4.4 Å) inter-chain spacing have a chance of reaching meaningful diffusion selectivities for ethylene/ethane separation. One clear method of improving selectivity during the film preparation method is by drying the film at high temperatures. PIM-PIs under extensive sub- $T_g$  annealing may have the matrix resilience required to enhance the diffusion selectivity of these closely related hydrocarbons [1]. Nevertheless, this work confirms the strongest contribution offered by PIM-materials to ethylene/ethane membrane separations as precursors for pyrolytic carbon molecular sieves.

## 8.2 *PBO for ethylene/ethane separation*

An intermediate product between CMSs and their *o*-functionalized PIM precursors, such as PIM-6FDA-OH, are polybenzoxazoles. The PBO derived from PIM-6FDA-OH, previously praised for its elongation at break [2], was not useful for ethylene/ethane separation. The PBO showed reduced selectivity because the TR process removed some of the constricting barriers responsible for increasing the diffusion selectivity, which is vital for ethylene/ethane separation.

## 8.3 *PIM-based CMS for ethylene/ethane separation*

PIMs are very rigid organic materials and they remain so even after crossing their degradation threshold. In this regard, they tend to retain some vestigial properties from their polymeric structure. From this work it was observed that carbons derived from PIMs at 800 °C were generally more permeable than those obtained from lower free-volume polymers, suggesting that some of their original interconnected intrinsic porosity was maintained. They also tend to produce cavities in the 3.6-4.4 Å range that are vital for ethylene/ethane discrimination. Previous studies using Matrimid® as a polymeric precursor described that pores may sinter to form no longer attractive PSDs. The ethylene/ethane selectivities of Matrimid®-derived carbons reached a plateau after 675 °C; pyrolysis at higher temperature (i.e. 800 °C) resulted in a severe loss in ethylene permeability without improvement in selectivity [3]. In general, the ethylene/ethane selectivity of polymers pyrolyzed above 600 °C increased and reached a commercially attractive area. Interestingly, carbons obtained at 600 to 675 °C, in the intermediate stages

of the degradation of the polymer backbone, have similar transport properties. This observation holds despite the precursor chemistry and free volume of the precursor, as shown in **Fig. 5.8**. The sintering mechanism that follows beyond that temperature differentiates between each precursor. The membranes generated from both PIM-6FDA-OH and PIM-6FDA at 800 °C represent the most selective carbon molecular sieves for ethylene/ethane reported to date by virtue of their narrow and rigid porosities [4].

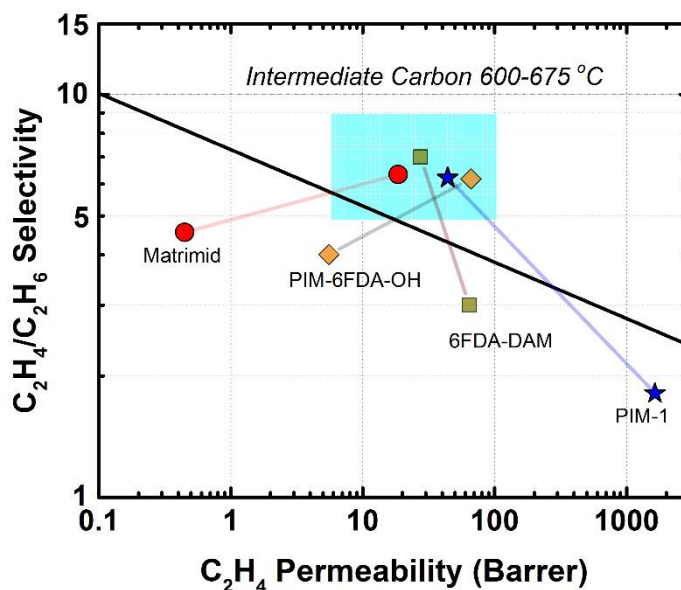


**Fig. 8.1.** Intermediate carbon region. Data underneath the polymer upper bound represents pristine Matrimid® 6FDA-DAM, PIM-6FDA-OH and PIM-1. Data above the tradeoff represent carbons generated between 600-675 °C [3-5].

#### 8.4 Thermally induced porosity evolution during pyrolysis

Breaking the polymeric backbone by thermal means changes its morphology and hydrocarbon affinity. PIM-6FDA-OH began as a hydrophilic polymer that undergoes a degradation reaction at 400 °C into hydrophobic PBO. Conversely, non-polar PIM-6FDA degrades at 480 °C into a carbonized matrix that shows some polar groups, as confirmed from their FTIR spectra at 600 °C (described in chapter 7). Overall, polar groups are likely to react as the temperature increases, although the degradation mechanisms of these polar groups created *in situ* remain to be fully understood. Furthermore, the polymers' intrinsic free volume strongly influences the likelihood of the carbon planes sintering in the advanced pyrolysis stages. PIM-1 collapsed in a similar fashion to Matrimid® and clarified the importance of crosslinking reactions in this sintering mechanism at higher temperatures [5]. This sintering mechanism was key to the fine tuning of the carbonaceous cavities of PIM-6FDA at 800 °C.

### 8.5 *Dilation of ultramicroporous CMS cavities*

The mixed-gas experiments of the 800 °C-treated CMS derived from both PIM-6FDA-OH and PIM-6FDA showed a transient decrease in selectivity as the upstream pressure increased to realistic industrial process values. It is suggested that subtle dilation of the carbon matrix occurred at high feed pressure as indicated by an enhancement on the ethane diffusion coefficient. Weak spots may exist in the carbon matrix that contains smaller proportions of damaged graphene. Previously, CMSs were reported to age analogously to glassy polymers, which is indicative of some “mobility” of the carbon matrix [6]. Conversely, CMS may also dilate due to highly sorbing feed gas components.

Even the smallest dilation of the regions containing ultramicroporous selective cavities, within the range of a tenth of an Ångstrom, can change the sieving properties of the CMS dramatically (**Fig. 8.2**).

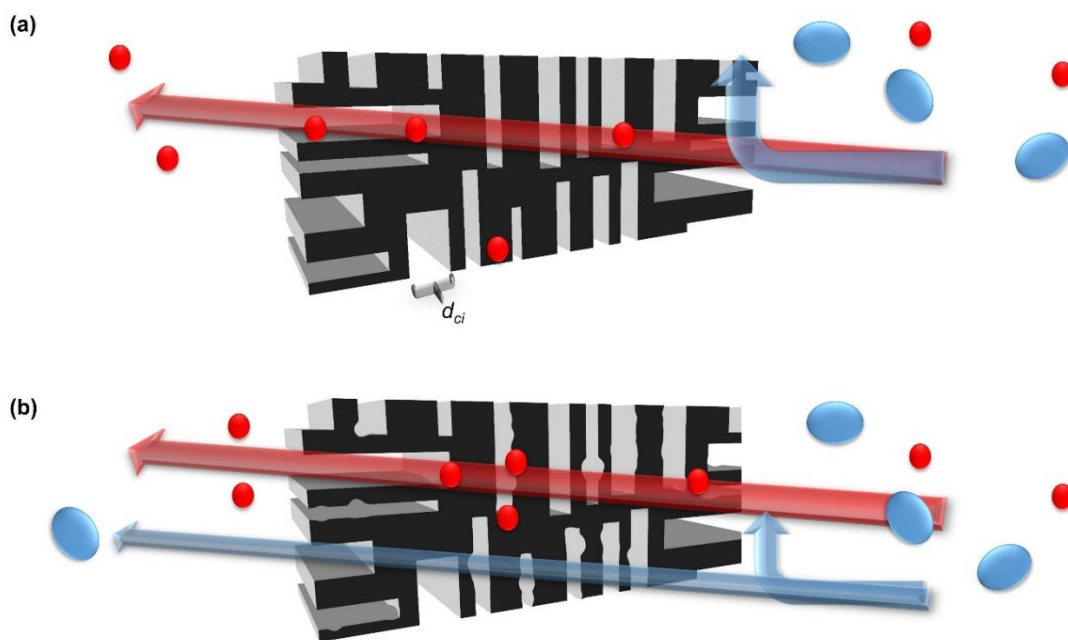


**Fig. 8.2.** Schematic representation of the ultramicroporous selective CMS pores ( $d_{ci}$ ) as they remain: (a) unaltered by condensable molecules and (b) dilate slightly allow permeation of bulkier molecules.

## 8.6 Recommendations

### 8.6.1 Advanced PIMs for ethylene/ethane separation

The most advanced PIMs known today also happen to bear the most rigid of contortion centers [7]. The right combination of rigidity and narrow porosity may still be

tailored to olefin/paraffin separations [8]. Such PIMs would need relatively small surface areas ( $< 100 \text{ m}^2\text{g}^{-1}$ ) coupled with high inter-chain interactions to provide a stable system that has a chance in discriminating ethylene from ethane.

### 8.6.2 *Advanced PIM precursors as carbon platforms and thin-film carbons*

PIMs are ideal carbon precursors due to their high carbon yield, the absence of a  $T_g$  prior to decomposition, and their known flexibility of synthesis. Previous work demonstrated that the mechanical properties of their heat-treated analogues exceeded those of their low free-volume counterparts [2]. Fundamentally, the pores of PIM-derived CMS membranes seem not to sinter as completely as those of lower free-volume polymers. Thus, they are more stable in response to heat-induced changes in their porosity. Given the extraordinary properties of these materials, it is strongly suggested to fabricate thin CMS films that would further clarify non-ideal effects such as swelling and aging [4, 6]. Furthermore, there is strong evidence that carbon hollow fibers derived from high  $T_g$  precursors may withstand microstructure collapse [9]. Therefore, PIM-based CMS hollow fiber membranes may not suffer from a substantial thickening of their separation layer due to their exceptional heat resistance.

### 8.6.3 *Control of the $O_2$ atmosphere*

As detailed by Kiyono et al. [10], the  $O_2$  presence during the pyrolysis protocol may cause significant variations in the transport performance of the resultant CMSs.  $O_2$

doping is a great tool with which to tailor porosity if used to generate tighter carbons at lower temperatures. Studies with PIM-derived CMS by varying the O<sub>2</sub> concentration would be interesting to conduct, as they would make possible the production of high-performing films under more economically feasible conditions.



## 8.7 References

- [1] R.J. Swaidan, X. Ma, E. Litwiller, I. Pinnau, Enhanced propylene/propane separation by thermal annealing of an intrinsically microporous hydroxyl-functionalized polyimide membrane, *J. Membr. Sci.*, 495 (2015) 235-241.
- [2] S. Li, H.J. Jo, S.H. Han, C.H. Park, S. Kim, P.M. Budd, Y.M. Lee, Mechanically robust thermally rearranged (TR) polymer membranes with spirobisindane for gas separation, *J. Membr. Sci.*, 434 (2013) 137-147.
- [3] M. Rungta, L. Xu, W.J. Koros, Carbon molecular sieve dense film membranes derived from Matrimid® for ethylene/ethane separation, *Carbon*, 50 (2012) 1488-1502.
- [4] O. Salinas, X. Ma, E. Litwiller, I. Pinnau, High-performance carbon molecular sieve membranes for ethylene/ethane separation derived from an intrinsically microporous polyimide, *J. Membr. Sci.*, 500 (2016) 115-123.
- [5] O. Salinas, X. Ma, E. Litwiller, I. Pinnau, Ethylene/ethane permeation, diffusion and gas sorption properties of carbon molecular sieve membranes derived from the prototype ladder polymer of intrinsic microporosity (PIM-1), *J. Membr. Sci.*, 504 (2016) 133-140.
- [6] L. Xu, M. Rungta, J. Hessler, W. Qiu, M. Brayden, M. Martinez, G. Barbay, W.J. Koros, Physical aging in carbon molecular sieve membranes, *Carbon*, 80 (2014) 155-166.
- [7] R. Swaidan, B. Ghanem, I. Pinnau, Fine-tuned intrinsically ultramicroporous polymers redefine the permeability/selectivity upper bounds of membrane-based air and hydrogen separations, *ACS Macro Lett.*, 4 (2015) 947-951.
- [8] R.J. Swaidan, B. Ghanem, R. Swaidan, E. Litwiller, I. Pinnau, Pure- and mixed-gas propylene/propane permeation properties of spiro- and triptycene-based microporous polyimides, *J. Membr. Sci.*, 492 (2015) 116-122.
- [9] L. Xu, M. Rungta, M.K. Brayden, M.V. Martinez, B.A. Stears, G.A. Barbay, W.J. Koros, Olefins-selective asymmetric carbon molecular sieve hollow fiber membranes for hybrid membrane-distillation processes for olefin/paraffin separations, *J. Membr. Sci.*, 423-424 (2012) 314-323.
- [10] M. Kiyono, P.J. Williams, W.J. Koros, Effect of pyrolysis atmosphere on separation performance of carbon molecular sieve membranes, *J. Membr. Sci.*, 359 (2010) 2-10.

## APPENDIX

**Table A.1.** Pure-gas permeability of heat-treated PIM-6FDA-OH at 35 °C and 2 bar pressure.

Treatment	Permeability (Barrer)					Selectivity (-)	
Temperature (°C)	H <sub>2</sub>	N <sub>2</sub>	O <sub>2</sub>	CH <sub>4</sub>	CO <sub>2</sub>	O <sub>2</sub> /N <sub>2</sub>	CO <sub>2</sub> / CH <sub>4</sub>
400 (TR-PBO)	649	43	153	49	760	3.5	15.5
500	3085	210	680	147	3732	3.2	25.3
600	3259	52	338	27.3	1447	6.5	53
800	2182	16.3	124.7	4.3	565	7.6	131

**Table A.2.** Pure-gas permeability of heat-treated PIM-6FDA at 35 °C and 2 bar pressure.

Treatment	Permeability (Barrer)					Selectivity (-)	
Temperature (°C)	H <sub>2</sub>	N <sub>2</sub>	O <sub>2</sub>	CH <sub>4</sub>	CO <sub>2</sub>	O <sub>2</sub> /N <sub>2</sub>	CO <sub>2</sub> / CH <sub>4</sub>
500	1430	115	440	127.5	2153	3.8	16.9
600	2037	42.1	294.6	27.3	1323	7.0	48.5
800	1126	4.1	39.6	0.9	143	9.6	160

**Table A.3.** Pure-gas permeability of heat-treated PIM-1 at 35 °C and 2 bar pressure.

Treatment	Permeability (Barrer)					Selectivity (-)	
Temperature (°C)	H <sub>2</sub>	N <sub>2</sub>	O <sub>2</sub>	CH <sub>4</sub>	CO <sub>2</sub>	O <sub>2</sub> /N <sub>2</sub>	CO <sub>2</sub> / CH <sub>4</sub>
400	2587	363	1031	580	6021	2.8	10.4
600	1239	31	132	19	796	4.2	42
800	380	1.3	12	0.24	65.5	9.4	270

## **VITA**

Octavio Salinas holds a B.Sc. in Chemical Engineering from Monterrey Institute of Technology and Higher Education (ITESM) and a M.Sc. from King Abdullah University of Science and Technology (KAUST). He has done experimental work at the University of Texas at Austin and at Georgia Institute of Technology. His work focuses on functionalized polymers for gas separation, olefin-paraffin purification, and carbon molecular sieve membranes. He earned his Ph.D. degree in Chemical Engineering in May 2016.